ANNUAL REPORT

30 June 1968

POST- DOCTORAL PROGRAM IN SEISMOLOGY

prepared for

GEOPHYSICS DIVISION
AIR FORCE OFFICE OF SCIENTIFIC RESEARCH
ARLINGTON, VIRGINIA 22209

by

DEPARTMENT OF GEOLOGY AND GEOPHYSICS
MASSACHUSETTS INSTITUTE OF TECHNOLOGY
CAMBRIDGE, MASSACHUSETTS 02139

sponsored by

ADVANCED RESEARCH PROJECTS AGENCY
NUCLEAR TEST DETECTION OFFICE
PROJECT VELA-UNIFORM
ARPA ORDER 292-67
AMENDMENT NR42

Department of Geology and Geophysics
Massachusetts Institute of Technology
Cambridge, Massachusetts 02139

POST-DOCTORAL PROGRAM IN SEISMOLOGY

Annual Report
To
Air Force Office of Scientific Research

1 July 1967 - 30 June 1968

ARPA Order No. 292-67

Project Code No. 8652

Name of Contractor - M.I.T.

Date of Contract - July 1, 1966

Amount of Contract - $377,755

Contract No. AF 49(638) - 1763

Contract Termination Date - June 30, 1970

Project Scientists - Frank Press 617/864-6900, ext. 3382
M. Nafi Toksöz 617/864-6900, ext. 6382
(also: Keiiti Aki, Paul E. Green Jr.,
and Edward J. Kelly, Jr.)

Short Title of Work - Post-Doctoral Program in Seismology

Abstract

The research efforts of the research associates supported by this program are described. These studies are divided into two groups: I. Continental size arrays and their application, and II. Theoretical seismograms and earth structure.

A continental size array can be realized by considering individual seismic stations as array elements. A section of North America, where LRSM stations exist in sufficient density, is considered as a very large aperture array to supplement LASA. Travel times and $dT/d\Delta$ values for core phases (PKP, PKIKP) are measured with this array and the results are interpreted. A technique for direct measurement of $dT/d\Delta$ is also described.

The theoretical seismograms for P and S waves are computed for a model of point source in layered medium and matched with observed records. With this technique, the structures are determined for oceanic crust using marine refraction profiles, and for the upper mantle utilizing seismograms from NTS nuclear explosions.

CONTENTS

BLANK PAGE

I. INTRODUCTION

In this report, the research activities carried out during the second year of this program are described. The program involves research associates and some staff members from the Department of Geology and Geophysics and the Lincoln Laboratory. The main purpose of this project is to utilize the new tools and techniques in seismological research. Seismic arrays and computation of theoretical seismograms constitute two such areas which are described in this report.

The first section of this report is devoted to studies with an array of continental dimensions. The apertures of conventional arrays such as LASA are too small for seismic phases with very high phase velocities. Extension of these arrays to a thousand or more kilometers is impractical. The technique that is utilized here is to treat a group of seismic stations as an array and to use the time of arrival at each station to compute the velocity ($d\Delta/dT$) of selected phases with a least squares procedure. This is demonstrated by utilizing the LRSM station network as such an array for the study of core phases.

In the second section of the report, the importance of synthetic seismograms in understanding observed records and determining earth structure is illustrated. At some epicentral distances where a multitude of seismic rays emerge from a given event (i.e. where travel time curves are duplicated or triplicated) seismograms are extremely complicated and difficult to analyze in terms of travel times alone. The Cagniard-de Hoop technique is utilized to synthesize seismograms which are compared with the observed records. The computed seismograms are very sensitive to velocity gradients in the crust and mantle and to the source time function. Thus the method provides the means for studying both the structure and the source parameter studies. Examples of these are shown in Section III of the report, where the method is generalized to spherical layer geometry.

II. CONTINENTAL ARRAY AND THEIR APPLICATIONS

II.1 On the Structure of the Earth's Core

(E.S. Husebye and M.N. Toksöz)

The existence of a central core in the earth was first suggested by Wiechert in 1897 and that of an inner core by Lehmann in 1936. Since then, there have been a number of studies and different core models proposed. These models vary from each other and they all fit different aspects of the data derived from core phases. The variations arise primarily because of the insensitivity of travel time curves to minor structural features deep in the core, and also from difficulties of identifying branches.

To demonstrate these problems, it may be helpful to examine some of the existing core models proposed by Jeffreys (1939), Gutenberg (1958a), Bolt (1964), Adams and Randall (1964), and Ergin (1967). These velocity models are shown in Fig. 1. Important parameters like travel time T, $dT/d\Delta$, and $d^2T/d\Delta^2$ for the above models were calculated using classical ray theory (Bullen, 1961). The results of these calculations are presented in Figures 2-3, where the core phases are identified by the branches to which they belong. From the figures we can deduce several important features. First, the travel time T is very insensitive to structural variations in comparison with its first and second derivatives ($dT/d\Delta$ and $d^2T/d\Delta^2$). The values of $dT/d\Delta$ for core phases are small, and errors in T could result in large errors in $dT/d\Delta$. As a result, it is almost impossible to calculate reliable $d^2T/d\Delta^2$ values from observed travel time data. However, the wave amplitude A is a function of $d^2T/d\Delta^2$ (Thirlaway and Carpenter, 1966):

$$A = \frac{B}{R(R-H)} \cdot \left[\frac{\rho_1 V_1}{\rho_0 V_0}\right]^{1/2} \cdot \left[\frac{1}{\sin\Delta \cdot \cos i_0 \cdot \cos i_1} \cdot \frac{dT}{d\Delta} \cdot \frac{d^2T}{d\Delta^2}\right]^{1/2} \cdot \frac{dQ}{dt} \qquad (1)$$

Above B is a constant, $\rho_0, \rho_1, V_0, V_1, i_0, i_1$ denote respectively,

the density, velocity and angle of incidence at the station and focus, $d\Phi/dT$ is the time derivative of the wave potential, R is earth radius and H focal depth. The relative effects of attenuation on different phases are neglected. In the above equation all quantities are either constants or slowly varying functions with the exception of $d^2T/d\Delta^2$. The expression $dT/d\Delta \cdot d^2T/d\Delta^2$ will be referred to as the geometrical spreading factor.

Figure 3 shows very clearly that amplitude observations are of crucial importance in core analysis. Large P wave amplitudes in the distance interval Δ~142°-147° have frequently been reported (Shahidi, 1968) and different explanations have been given for this feature. Basically, the above phenomenon is attributed to a large geometrical spreading factor, which may be combined with diffraction effects near the caustic B (Figure 3). The latter hypothesis (Jeffreys, 1939) favors the interpretation that the precursors, i.e. waves arriving prior to the P(DF) phases, are real core phases and not diffraction effects. Unfortunately, it is very difficult to verify diffraction phenomena associated with a caustic in this case, as the local velocity variation is not well known and might strongly influence the diffraction pattern. Another difficulty here is the problem of proper phase identification in the 140°-150° distance interval.

In recent years, much attention has been given to the precursor branches mentioned above. Although these waves are relatively easily detectable on modern instruments, the number of phases, at most 3 so far, and their arrival times are somewhat controversial. An important question here is how many core phase branches can be observed. This question has to be raised as $dT/d\Delta$ for core phases vary continuously between say, 0.0-4.60 sec/deg and the well established DF and AB

branches between $\Delta = 143°$ and 180° account for roughly two-thirds of this variation. Also, the precursor phases are always very weak. This is not compatible with the values of their geometrical spreading factors. As a result one wonders whether there may be another, quite different explanation of these waves than those advocated up to now.

Another property of existing core models is the small $d^2T/d\Delta^2$ values and large $dT/d\Delta$ values allocated for most part of the AB branch. The first term gives a small geometrical spreading factor while the latter requires a large angle of incidence at the mantle-core boundary. That is, at large distances the amplitude of the P(AB) would be weak compared to the P(DF) phase.

In this study, in addition to travel times we measured $dT/d\Delta$ and the relative amplitudes of the core phases for determining a structure which is constrained by all these quantities.

DATA AND METHODS OF ANALYSIS

To determine travel times of core phases a large number of seismograms from North American WWSS and LRSM stations were analyzed (Table I) for fifteen earthquakes listed in Table II. The procedure used was to identify the wave associated with a certain branch and to read the arrival time at each station. To determine $dT/d\Delta$ for core phases an array with the proper dimensions is needed for the measurement of such high phase velocities. Existing arrays such as LASA are too small for measuring phase velocities larger than 25 km/sec.

We consider the North American station network as a large array and express the travel time variation of this array as

$$T = f(\varphi, \lambda) \tag{2}$$

where φ and λ are station latitude and longitude. Expansion of $f(\varphi,\lambda)$ in a Taylor series gives

$$f(\varphi+d\varphi, \lambda+d\lambda) = f(\varphi_0, \lambda_0) + \left[\frac{\partial}{\partial\varphi} d\varphi + \frac{\partial}{\partial\lambda} d\lambda\right] \cdot f(\varphi_0, \lambda_0) \tag{3}$$

Neglecting terms of higher order than two, we can write for T, at the i-th station

$$T_i = a_0 + a_1\varphi_i + a_2\lambda_i + a_3\varphi_i^2 + a_4\varphi_i\lambda_i + a_5\lambda_i^2 \tag{4}$$

Now T is expressed as a second order polynomial in φ and λ . From a set of observations by the method of least squares the coefficients can be determined.

The ray parameter p (i.e. the gradient of the scalar T) is obtained by differentiating eq.(4).

$$\frac{dT}{dA} = |\bar{P}| = \left|(\bar{N}\cdot\nabla)T\right| = \left|\frac{\partial T}{\partial\varphi}\bar{e}_\varphi + \frac{1}{\cos\varphi}\frac{\partial T}{\partial\lambda}\bar{e}_\lambda\right| \tag{5}$$

where a bar denotes vectors. The azimuth of the normal to the wave-front is

$$Azi = \text{Arctan}\left|\bar{p}\,\bar{e}_\varphi \,/\, \bar{p}\,\bar{e}_\lambda\right| \tag{6}$$

By taking the derivative of the (5) in the direction of ray, we obtain $d^2T/d\Delta^2$

$$\frac{d^2T}{d\Delta^2} = \left| \left[\left(\cos Azi\ \bar{e}_\varphi + \sin Azi\ \bar{e}_\lambda \right) \nabla \right] \bar{p} \right| \qquad (7)$$

It should be noted that this procedure is independent of focal parameters. In fact, approximate epicenter location is easily obtained from the calculated azimuth values and a table of p- values as function of distance. As stated before, accurate travel times are of critical importance when dealing with core phases. Therefore, wherever possible, the records were correlated with each other to minimize reading errors (Jansson and Husebye, 1968), also available station corrections, namely those of (Chinnery and Toksöz, 1967) and (Cleary and Hales, 1966) were incorporated in the analysis. The former gave rise to the smallest standard error in T and were adopted in this study. To reduce errors of this type, the arrays formed, consisted of stations in the NE or SW part of North America. During the dT/dΔ calculation, array size and distance range were varied when sufficient data were available. This procedure proved useful in locating errors. Since the accuracy of dT/dΔ decreases with distance from the array center, only the central dT/dΔ value was retained for further analysis. The only exception was the BC-branch where few records were available. Accordingly, despite the large number of records used, the dT/dΔ data obtained were few.

In the case of core phases, the main problem is still a proper phase identification. The amplitude of these phases play an important role in the identification. Wherever possible amplitudes were measured and computed. To avoid the problems of normalizing magnitudes and varying crustal effects at different stations, amplitude ratios such as Amp(AB)/Amp(DF), between branches were used for each event.

EXPERIMENTAL RESULTS

The T, $dT/d\Delta$ and amplitude values obtained for the main branches of the core phases are presented in Figures 5-8. For some distance interval our $dT/d\Delta$ values deviate significantly from those previously reported. A more detailed presentation of the data for each branch is given below.

The DF-Branch

The main problem here is to locate the branch endpoint D. The core phases have been observed down to about 105°. Gutenberg (1958a) and Ergin (1967) put D around $\Delta \approx 125°$, while Jeffreys (1939) places it at $\Delta = 110°$. We terminate the DF-branch at $\Delta = 123°$, as the amplitude curve has a pronounced maximum here (Figure 9). If the inner core boundary is characterized by a sharp velocity increase, then the amplitudes of P(DF) waves near the endpoint D should be small due to nearly grazing incidence and small $d^2T/d\Delta^2$ values. In our opinion, the waves observed between 105° - 123° do not belong to the DF-branch but are reflections from an inner core boundary. Some records of P-waves in this distance range are displayed in Figure 10.

The DC-Branch

This branch, sometimes denoted as the receding branch of DF, ranges from $\Delta = 123°$ to C at about 160° where $dT/d\Delta \sim 2.45$ sec/deg. From what has been said above, it seems appropriate to prolong this branch down to 105°, naming the endpoint D^1. The observational evidence of the existence of the DC-branch is meager, and has been based mainly on the requirement of a monotonic increase of $dT/d\Delta$ between 0.0 and 4.60 for core phases. Subiza and Båth (1964) attributed observations of large wave amplitudes

at $\Delta = 130° - 138°$ to this branch. Some of our records strongly support the above observations as demonstrated in Figure 10. Identification errors are possible since the travel time difference T(DF) - T(DC) would be about 2-4 seconds. It should be noted that only one of the events analyzed gave a dT/dΔ value which is expected for the DC branch. On the other hand, the assumed DF-waves sometimes give dT/dΔ values expected for the DC-branch. Thus, the given dT/dΔ values for the DC-branch are based on the endpoint values of the DF and BC branches and amplitude data. Amplitudes along the DF-branch should decrease steadily toward the endpoint D due to decreasing geometrical spreading factor and energy transmission through an inner core boundary. For large amplitudes on parts of DC, the range of variation of dT/dΔ must be sufficiently large. Our value is about 0.5 sec/deg while corresponding values for Adams and Randall and Bolt's models are 0.20 and 0.10 sec/deg respectively. Also their distance range is about 15° larger than ours.

The Precursor Branches

An interesting but confusing feature of core phases is the existence of some precursors before the DF-branch. These are named GH and IJ branches (Figure 2) by Adams and Randall (1964). These forerunners were first attributed to diffraction effects near a caustic at 143° (Bullen and Burke-Gaffney, 1958). Later studies, (Bolt, 1964; Adams and Randall, 1964) introduced a layered zone outside the inner core as a more satisfactory explanation of these waves. The precursor branches will not be included in our core model for several reasons. First, precursors are observed from about $\Delta = 144°$ and down to about 105° and they do not resemble ordinary P-waves (see Figures 10

and 11). They are in general long and oscillatory wave trains similar to guided waves. It is noteworthy that waves identified as forerunners on some long-period records ($\Delta \approx 105° - 112°$) give evidence of negative dispersion. Second, the calculated $dT/d\Delta$ values partly overlap with those of our BC-branch. The precursor branches are characterized by very weak onsets. This may explain the differences in arrival times between Adams and Randall's IJ-branch and Bolt's FG branch which is about 7 sec at $\Delta \approx 135°$. Our own records sometimes give arrival times relative to T(DF) in agreement with Adams and Randall's data, other times with those of Bolt, and in a few records, arrivals precede those of Adams and Randall by a few seconds. The possibility of three precursor branches as proposed by Ergin (1967) cannot be excluded. The above points are important, as the precursors arrive between the two main phases (AB and DF) at distances beyond 140°. At these distances it is not possible to vary the phase arrival times much. This explains the large differences in reported $dT/d\Delta$ values for the precursor branches. From the available evidence it is not clear that the forerunners are core phases of ordinary type as interpreted by Bolt (1964), Adams and Randall (1964) and Ergin (1967). If we interpret the above precursors at least partly as some sort of guided waves (to be discussed later), then our $dT/d\Delta$ values will correspond to the slowness of energy bursts in these waves. Also, such an explanation will remove the inconsistency in the reported arrival times and number of phases identified. Precursors are very weak between $\Delta \approx 114°$ and $\Delta \approx 124°$, and this may indicate that more than one excitation mechanism exists.

The BC-Branch

The BC-branch displayed in our Figure 6 incorporates

features from different models, but it does not agree wholly with any single model proposed previously. The branch we have shown is similar to that of Adams and Randall (1964) in the sense that it excludes the possibility of strong diffraction effects near B. Also, like Jeffreys and Gutenberg's models, $dT/d\Delta$ values range from about 2.45 - 3.45 sec/deg. The hypothesis of strong diffraction effects was omitted for several reasons. First, observed $dT/d\Delta$ values do not favor such features, the amplitude observations of P(AB) waves require that $dT(AB)/d\Delta$ is almost constant near B. The $d^2T(BC)/d\Delta^2$ parameter is large enough to explain the observed amplitudes along the BC-branch. Theoretical amplitude curve given in Figure 8 is the geometrical spreading factor of the BC-branch relative to the DF-branch. If B were associated with diffraction, then we should expect irregularities in signal shape and amplitude variation. However, no evidence of such behavior of P(BC) could be detected. This check was performed partly by visual examination and partly by applying a signal-matching method. The latter method also was used unsuccessfully in search of the fourth P phase of Adams and Randall's and Bolt's core models, i.e. P(IJ) or P(GH). In fact, even the identification of the AB-branch was questionable for $\Delta \approx 141°$-152°. An exact location of the branch endpoints B and C is impossible due to decreasing amplitudes toward these points. The $dT/d\Delta$ estimation was difficult as the data available was concentrated at $\Delta \approx 144.5° - 147°$ and $\Delta \approx 150° - 152°$. Between $\Delta = 141°$ and 144.5° the time lags between T(DF), T(DC), T(BC) and T(AB) are small, preventing reliable phase identification.

The AB-Branch

The amplitude observations in Figure 8 require a slow

dT(AB)/dΔ increase all the way from B toward A, contrary to that in other core models. Our amplitude data and those of Shurbet (1967) and as well the few dT(AB)/dΔ data available confirm this hypothesis. In the distance interval 155°-180°, all T(AB) and T(DF) were obtained from records of a single event.

Travel time analysis for stations near the antipodal point are difficult as epicentral distance may be nearly constant while station separations and azimuths vary considerably. In other words, even very small lateral velocity gradients in the mantle and outer core could cause large errors in the dT/dΔ values. Observed and calculated travel time data of P(DF), P(BC) and P(AB) are shown in Figure 5. A clear secondary onset occuring at both the AB and DF branches is attributed to crustal reflection or reverberation effects. The location of the endpoint A and also the corresponding dT/dΔ value are uncertain. From our data we cannot determine whether AB-branch extends beyond 180°, while Ergin (1967) reports weak P(AB) onsets out to $\Delta \sim 200°$.

A NEW CORE MODEL

The dT/dΔ data we presented in the previous section differ from those of other core models at some distance intervals. Although there are regions where observations are scarce, the new results warrant interpretation in terms of a velocity structure inside the core. The procedure we use is a simplification of that outlined by Bullen (1961) which includes stripping off of the mantle. Although the above method is straight forward, we sometimes have to resort to the reverse procedure, that is fitting the preliminary model to the observed T, dT/dΔ and amplitudes. The reason for this is the insensitivity of the above method to small travel time gradients near branch endpoints.

Before we proceed with a detailed discussion of the new core model, we should discuss briefly the accuracy of the data. The standard deviation of the $dT/d\Delta$ estimates are in general, small, around ± 0.08 sec/deg. The records from the LRSM stations are of an excellent quality, permitting reading of arrival times to the nearest 0.1 sec. However, manipulations with array size and station corrections indicate existence of biased errors which may amount to ± 0.10 sec/deg. This figure is likely to be larger for the BC and AB branches. We searched for large errors in the above $dT/d\Delta$ values by checking observed amplitude ratios with those computed on the basis of our model. The effect of errors in $dT/d\Delta$ on the P-velocity depth distribution is most easily anticipated at branch endpoints. For example, a $dT/d\Delta$ interval of 0.02 sec/deg is equivalent to a depth interval of about 11 km. The corresponding velocity increment is small, about 0.006 km/sec for parts of the AB-branch. Just near boundaries where velocity discontinuities exist, distortion of these boundaries will account for larger velocity errors. This is demonstrated in Figure 1, which shows that the given core models with exceptions of Ergin's and a small part of Jeffreys" are very similar despite large differences in the original data from which they were derived. Although the absolute values of travel times are influenced by focal parameters and the velocity distribution in the mantle, the time differences between the BF, BC and AB branches should be insensitive to parameters other than the epicentral distance.

We consider the amplitudes of core phases as a strong constraint in the interpretation of travel time and the $dT/d\Delta$ data. The joint interpretation of travel time, $dT/d\Delta$ and the amplitudes remove much of the ambiguity otherwise involved. A detailed discussion of this important point is given by Asbel, et al. (1966). As amplitude observations of short period P-waves exhibit considerable scattering we only

seek a broad agreement between the observed and the calculated amplitudes. To minimize source magnitude and crustal response effects we use the ratios of the amplitudes of different phases such as A(AB)/A(DF).

A factor of crucial importance in deducing a core model is the value of $dT/d\Delta$ at the core-mantle boundary. For example, commonly accepted P-wave velocity values for the lowest 200 km of the mantle is around 13.60 km/sec, which gives a maximum $dT(AB)/d\Delta$ value of about 4.45 sec/deg. However, this is incompatible with our observations. One way to avoid this difficulty is to increase the $dT(AB)/d\Delta$ factor by lowering the P-velocity in the lowest part of the mantle. Our final values are shown in Figure 14. Such a velocity distribution and $dT/d\Delta$ values of 4.55-4.60 sec/deg are in general agreement with the recent array measurements and the resultant structure of the deepest part of the mantle (Johnson, 1967; Sachs, 1967; Fairborn, et al, 1967). At the endpoint A of this branch, the depth of penetration is about 2530 km from the earth's center. This means that the velocity distribution from this depth to the core-mantle boundary is obtained on the basis of travel times. In other words, with only PKP and PKIKP data it is quite permissible to vary the velocity distribution in the outer core as long as total travel time is satisfied. We had to assume a slightly steeper velocity gradient in the outer core than that of Jeffreys' model. This was necessary to ensure reasonable travel times for P(AB). The $dT(AB)/d\Delta$ and amplitude data require an almost constant velocity gradient between R = 2500-2150 km.

As for the BC-branch, the effect of small errors in the velocity distribution in the AB-depth interval will diminish toward C. Assuming that A(BC)/A(DF) is mainly governed by the geometrical spreading factor, our model gives a reasonable fit of expected amplitude ratios to those actually observed (and to

those of Shurbet, 1967). The calculated P-wave velocity distribution for the BC interval may be interpreted as a transition from homogeneous material at B to inhomogeneous material at C. The branch point B is characterized by a turning point in the curvature on the velocity curve. We would like to point out that small variations of the velocity structure here would permit an extension of the AB and BC-branches toward shorter distances.

As pointed out previously, hardly any reliable observations of the P(DC) phases are available. This means that the structure near the inner core boundary may be more complex than hereto assumed. A rapid, continuous velocity increase in this region, as favored by Gutenberg, produces structures which would not permit core wave observations at distances shorter than $\Delta \simeq 125°$. The branch endpoint D is the point where the reflected P wave from the inner core boundary obtains its critical value and is located somewhat arbitrarily, at $\Delta = 123°$. This distance was chosen because at $\Delta = 120° - 124°$ the wave amplitudes are very large and some signal decorrelations occur. The latter effect may partly be due to the dominance of high frequency energy in the signals. Actually, we should expect some pecularities in the P-wave near the critical angle of incidence. Another factor favoring location of D at $\Delta = 123°$ is that this would allow a larger energy concentration in the region $\Delta = 110° - 123°$ as required by amplitude observations.

The DC-branch is constituted of waves reflected from the inner core boundary, and more formally should be denoted as PKiKP-waves. We find it convenient to locate D' at $\Delta = 105°$ as it is very difficult to observe this wave for shorter distances due to decreasing reflection coefficients and interference from other waves.

In the previous section we discussed the reasons for our preference to interpret the precursor branches as guided waves

rather than core waves of ordinary type. As guided waves travel time puts a strong constraint on possible sources of these waves. First, they cannot be associated only with an inner core boundary or the transition zone as their travel times do not fit such paths. The outer core is not a likely region. The ray deflection at the mantle-core boundary, would make the angle of incidence in this region too small to trap sufficient wave energy. Focal mechanism peculiarities have to be excluded since the precursor observations are limited to certain distance intervals. One possible explanation is propagation in the mantle-core transition zone. So far, only the propagation of high velocity, low frequency diffracted waves has been investigated in this zone (Phinney and Alexander, 1966). However, slow, high frequency diffracted waves as reported here may be possible, and this problem is being studied at this time. The above explanation may not be sufficient to account for all the features of the precursors. Similar excitation might exist at the inner core boundary causing the observed increase in precursor amplitude at distances beyond 128°. Some contribution also may come from ordinary P-waves as a result of possible prolongation of the P(AB) and P(BC) branches due to velocity peculiarities at $R \approx 2000$ km.

Our new model for the core and the lower most part of the mantle, is presented in Figure 14. We have introduced a velocity decrease in the mantle and a gradient increase in the outer part of the core. These changes are based entirely on our analysis of PKP waves traveling in the lower parts of the core. However, the essential feature of the new core model is an inhomogeneous zone extending out to $R = 2530$ km. The main evidence for the inhomogeneity is the new values of $dT(AB)/d\Delta$. Although seemingly modest, they are responsible for this extension. Furthermore, this effect is not removable

by small changes in the velocity distribution in the outer part of the fluid core. At $R \sim 2000$ km, corresponding to the branch point B, the velocity gradients increase rapidly over a small depth interval. We cannot exclude the possibility of a small velocity discontinuity in this region. For the remaining part of the core ($R < 1900$ km), the velocity gradient is small, positive or negative, which is in good agreement with other models. The much discussed precursor branches would have a modest influence on the velocity structure. Our calculations give that the inner core radius is around 1250 km, and this boundary may be preceded by some sort of a transition zone. The exact location of the branch point D does not strongly effect the above structure.

Assumptions introduced when deriving the structure of the outer core, naturally would affect the calculations of the inner core. In other words, the core model above might need revision, but the essential feature, the very small velocity gradients throughout the larger part of the core should remain unchanged. If it is found desirable to change the absolute travel times, this can be done by small velocity variations in the inner and outer core or in the mantle.

CONCLUSIONS

The core model presented in this paper favors a division of the earth's core into four parts.

1. The inner core or the DF zone between R = 0-1250 km. The inner core has a nearly constant velocity throughout except at the outer side where a possible small velocity increase may be followed by a large velocity decrease.

2. The inner central region or the BC zone between R 1375-2000 km. This region has a negative velocity gradient at the inner end and a 125 km wide transition zone (DC branch) to bridge the gap to the inner core.

3. The outer central region or the AB zone between ξ = 2000-2530 km. In most parts of this zone the velocity gradient is small and could be positive or negative.

4. The outer core or SKS zone between ξ = 2530-3480 km. The velocity gradient is assumed to be fairly constant and somewhat steeper than in Jeffreys' model to satisfy the total travel time data.

As a final note we should again mention that the core model shown in Figure 14 is subject to uncertainties arising from the problems of phase identifications, number of branches, and branch endpoints. The effects of the scatter in our data on the final model were investigated (Toksöz, et al, 1968). It is found that the scattering of data does not affect the major features of the above core model.

ACKNOWLEDGEMENTS

The LRSM data used in this study were obtained from Seismic Data Laboratory of Teledyne Industries. We are grateful for the help and cooperation of the SDL personnel. We benefited greatly from the discussions with Drs. D. Helmberger and R.A. Wiggins. This research was supported by the Advanced Projects Research Agency and monitored by the Air Force Office of Scientific Research under contract AF 49(638)-1759.

References

Adams, R.D. and M.J. Randall, The fine structure of the earth's core, Bull. Seism. Soc. Am., 54, 1299-1313, 1964.

Asbel, I.J., V.I. Keilis-Borok and T.B. Yanovskaja, A technique of a joint interpretation of travel-time and amplitude-distance curves in upper mantle studies, Geophys. J., 11, 25-55, 1966.

Bolt, B.A., The velocity of seismic waves near the earth's center, Bull. Seism. Soc. Am., 54, 191-208, 1964.

Bullen, K.E., Seismic ray theory, Geophys. J., 4, 93-105, 1961.

Bullen, K.E. and T.N. Burke-Gaffney, Diffracted seismic waves near the PKP caustic, Geophys. J., 1, 9-17, 1958.

Chinnery, M.A. and M.N. Toksöz, P-wave velocities in the mantle: I, below 700 km., Bull. Seism. Soc. Am., 57, 199-226, 1967.

Cleary, J. and A.L. Hales, An analysis of travel times of P waves to North American stations in the distance range 32° to 100°, Bull. Seism. Soc. Am., 56, 467-489, 1966.

Ergin, K., Seismic evidence for a new layered structure of the earth's core, J. Geophys. Res., 72, 3669-3687, 1967.

Fairborn, J.W., M.N. Toksöz and A.F. Gangi, Measurements of wavefront parameters and seismic velocity profiles in the lower mantle, Transactions, Am. Geophys. Union, 48, 195, 1967.

Gutenberg, B., Wave velocities in the earth's core, Bull. Seism. Soc. Am., 48, 301-324, 1958.

Jansson, B. and E.S. Husebye, Application of array data processing techniques to a network of ordinary seismograph stations, Pure and Appl. Geophys., in press.

Jeffreys, H., The times of the core waves, Mon. Not. R. Astr. Soc. Geophys. Suppl., 4, 548-561, 594-615, 1939.

Johnson, L., Array measurements of P velocities in the lower mantle, paper presented at Seism. Soc. Am. meeting, Santa Barbara, Calif. 1967.

Lehmann, I., P', Publ. Bur. Cent. Seism. Intern., Ser. A, 14, 3-31, 1936.

Phinney, R.A. and S.S. Alexander, P wave diffraction theory and the structure of the core-mantle boundary, J. Geophys. Res., 71 (24), 5959-5975, 1966.

Sachs, I.S., Diffracted P-waves studies of the earth's core, 2, lower mantle velocity, core size, lower mantle structure, J. Geophys. Res., 72 (10), 2589-2594, 1967.

Shahidi, M., Variation of amplitude of PKP across the caustic, Phys. Earth Planet. Interiors I, 97-102, 1968, North-Holland Publ. Co.

Shurbet, D.H., The earthquake P phase which penetrate the earth's core, Bull. Seism. Soc. Am., 57, 875-890, 1967.

Subiza, G.P. and M. Båth, Core phases and the inner core boundary, Geophys. J., 8, 496-513, 1964.

Thirlaway, H.I.S. and E.W. Carpenter, Seismic signal anomalies, travel times, amplitudes, and pulse shapes, VESIAC Rep. 4410-99-X, Willow Run Lab., Univ. Mich., 119-140, 1966.

Toksöz, M.N., E.S. Husebye and R.A. Wiggins, Structure and properties of the earth's core, To be published.

Wiechert, E., Über die Massenverteilung im Innern der Erde, Nachr. Akad. Wiss. Goettingen, Math.-Phys. KL., 221-243, 1897.

TABLE 1

Stations used for travel time and $dT/d\Delta$ measurements

STA.	Coordinates		STA.	Coordinates	
	Latitude	Longitude		Latitude	Longitude
AAM	42 17 59 N	83 39 22 W	FNWV	38 32 58 N	79 30 47 W
ALQ	34 56 30 N	106 27 30 W	FOTX	30 54 06 N	102 41 52 W
APOK	34 49 59 N	98 26 09 W	FRMA	46 06 00 N	106 26 25 W
ATL	33 26 00 N	84 20 15 W	FTBC	54 54 49 N	122 52 56 W
BKS	37 52 36 N	122 14 06 W	GEO	38 54 00 N	77 04 00 W
BLD	37 12 40 N	80 25 14 W	GEAZ	33 46 32 N	101 31 41 W
BLWV	37 47 56 N	81 18 36 W	GIMA	47 11 34 N	104 13 10 W
BOZ	45 36 00 N	111 38 00 W	GOL	39 42 01 N	105 22 16 W
BRPA	39 55 27 N	78 50 41 W	GPMN	47 39 52 N	93 29 22 W
COK	44 35 09 N	123 18 12 W	GSC	35 18 06 N	116 48 17 W
CRNB	40 39 52 N	96 51 15 W	GVTX	32 53 09 N	96 59 54 W
DAL	32 50 46 N	96 47 02 W	HDPA	40 59 44 N	77 35 44 W
DHNY	42 14 39 N	74 53 18 W	HHND	48 56 53 N	98 41 33 W
DRCO	37 27 53 N	107 47 00 W	HLID	43 38 50 N	114 15 02 W
DUG	40 11 42 N	112 48 48 W	HNME	46 09 43 N	67 59 09 W
EBMT	41 37 40 N	95 37 20 W	HVMA	48 25 20 N	109 49 20 W
ENMO	36 52 58 N	90 35 44 W	JCT	30 28 46 N	99 48 08 W
EKNV	39 12 32 N	115 42 37 W	JELA	31 47 05 N	92 00 55 W
EVAL	32 47 10 N	87 52 00 W	JPAT	52 53 50 N	118 05 25 W
FLBC	50 51 38 N	122 50 11 W	JRAZ	34 49 32 N	111 59 25 W
FLO	38 48 06 N	90 22 12 W	KCMO	39 21 21 N	94 40 17 W

KHAZ	34 29 00 N	111 02 03 W		SV2QB	54 48 54 N	66 45 31 W	
KNUT	37 01 22 N	112 49 39 W		SWMA	48 58 08 N	111 57 46 W	
LCNM	32 24 08 N	106 35 58 W		TKWA	48 47 38 N	119 35 16 W	
LGAZ	34 24 28 N	111 32 45 W		TUC	32 18 35 N	110 46 56 W	
LON	46 45 00 N	121 48 36 W		VOIO	42 13 30 N	92 07 37 W	
LSNH	44 14 18 N	71 55 21 W		WES	42 23 05 N	71 19 20 W	
LUB	33 35 00 N	101 52 00 W		WFMN	43 48 05 N	92 22 23 W	
MDS	43 22 20 N	89 45 36 W		WNSD	43 15 08 N	100 11 46 W	
MNN	44 54 52 N	93 11 24 W		WOAZ	35 52 53 N	110 37 15 W	
MNNV	38 26 10 N	118 08 53 W					
NLAZ	35 54 05 N	109 34 10 W					
OGD	41 04 00 N	74 37 00 W					
OXF	34 30 43 N	89 24 33 W					
PIWY	42 27 10 N	109 32 55 W					
RCD	44 04 30 N	103 12 30 W					
RGSD	45 12 59 N	63 32 05 W					
RKON	50 50 20 N	93 40 20 W					
RYND	48 05 50 N	101 29 40 W					
SCP	40 48 36 N	77 52 10 W					
SGAZ	35 38 27 N	113 15 39 W					
SHA	30 41 41 N	88 08 23 W					
SIBC	54 47 18 N	127 04 17 W					
SNAZ	33 51 49 N	111 41 34 W					

TABLE 2

List of earthquakes used in the core phase studies

Date	h	m	s	Location		Depth	Mag.
APR 7, 1964	13	18	18.9	0.1N	123.7E	150 km	6.30
MAY 26, 1964*	10	59	12.3	56.2S	27.8W	120	6.5
SEP 12, 1964	22	07	03.2	49.1S	164.2E	33	6.90
NOV 1, 1964	12	26	06.2	3.1N	128.1E	65	6.3
JAN 16, 1965	11	32	37.4	56.6S	27.4W	101	6.2
JAN 17, 1965	20	57	41.3	6.8S	109.1E	242	6.5
JAN 24, 1965*	00	11	12.1	2.4S	126.0E	6	6.6
MAR 21, 1965	11	08	16.2	1.5S	126.5E	33	6.2
MAY 16, 1965	11	35	46.0	5.3N	125.7E	36	6.2
MAY 19, 1965	06	03	58.9	6.5S	105.4E	74	6.3
MAY 24, 1965*	19	44	10.9	56.1S	27.6W	120	6.7
AUG 2, 1965	13	19	55.9	56.2S	157.9E	33	6.6
SEP 12, 1965	22	02	34.3	6.3S	70.5E	34	6.2
NOV 21, 1965	10	31	54.0	6.3S	130.3E	33	6.6
FEB 17, 1966	11	48	00.8	32.2S	78.9E	33	6.4

* No $dT/d\Delta$ calculated.

Figure Captions

1. P wave velocity models for the earth's core.

2. $dT/d\Delta$ variations for the different velocity models.

3. $d^2T/d\Delta^2$ plot for Adams and Randall's core model.

4. Contour map of travel time residuals from the Long Shot explosion.

5. Observed $dT/d\Delta$ values. Solid lines indicate the average of observations and used in the velocity determination.

6. Observed and calculated travel times. Points connected by thin lines were interpreted as crustal reverberations. Thick lines correspond to travel times calculated from our core model.

7. Samples of P(D'DF) phases.

8. Amplitude observations in the distance interval 135°-180°.

9. Normalized amplitude observations in the distance interval 105°-135°.

10. Seismograms showing P(DC) phases. Precursors are indicated by the notation PRE.

11. Sample seismograms of precursor phases. Note the long and almost continuous nature of these waves.

12. Samples of P(BC) waves.

13. Seismograms showing P(AB) and P(DF) phases.

14. The new core model. Velocity changes in the lowermost part of the mantle are also shown.

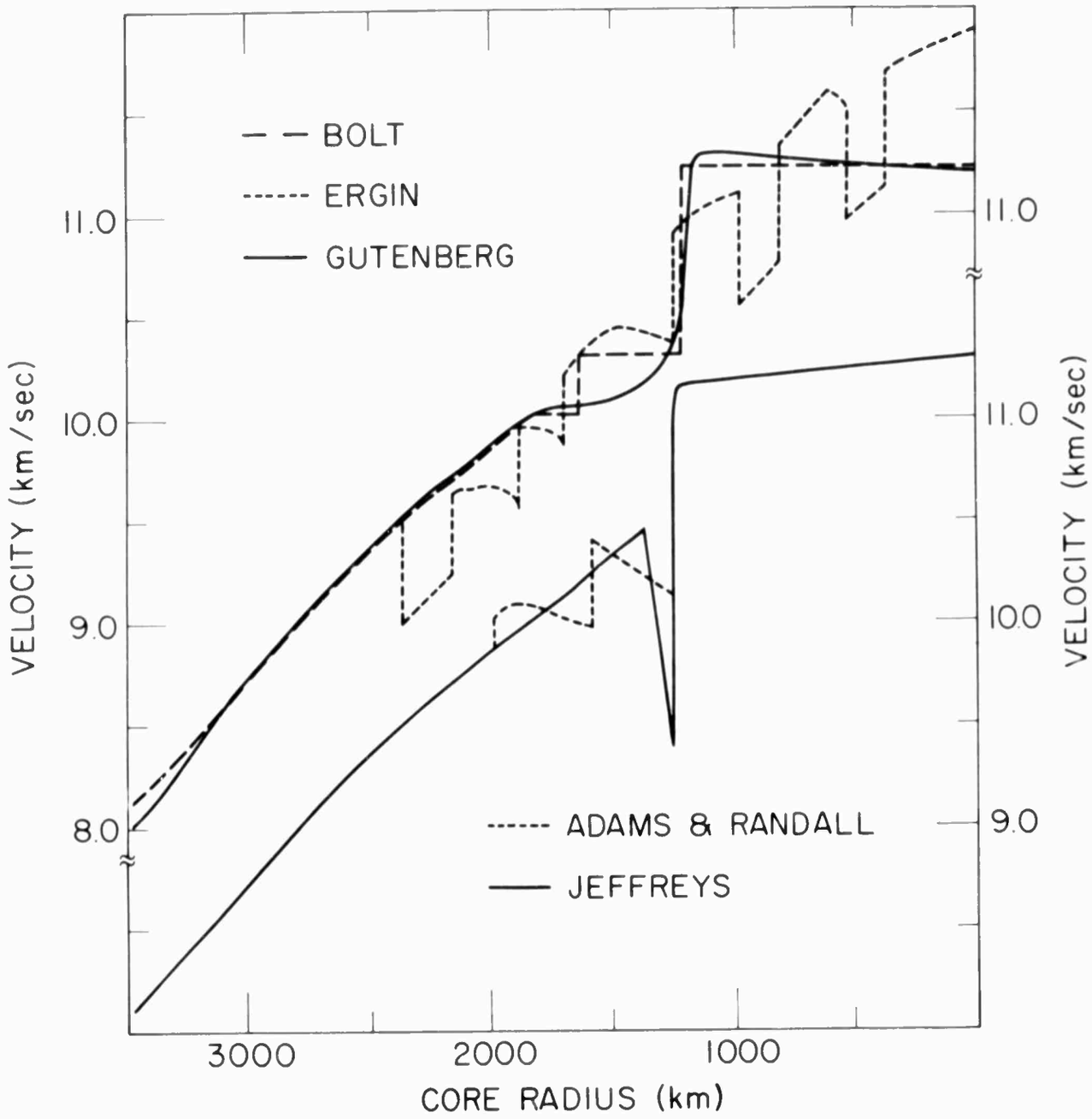
BOLT
ERGIN
GUTENBERG
ADAMS & RANDALL
JEFFREYS
VELOCITY (km/sec)
11.0
10.0
9.0
8.0
3000
2000
1000
CORE RADIUS (km)

Fig. 1

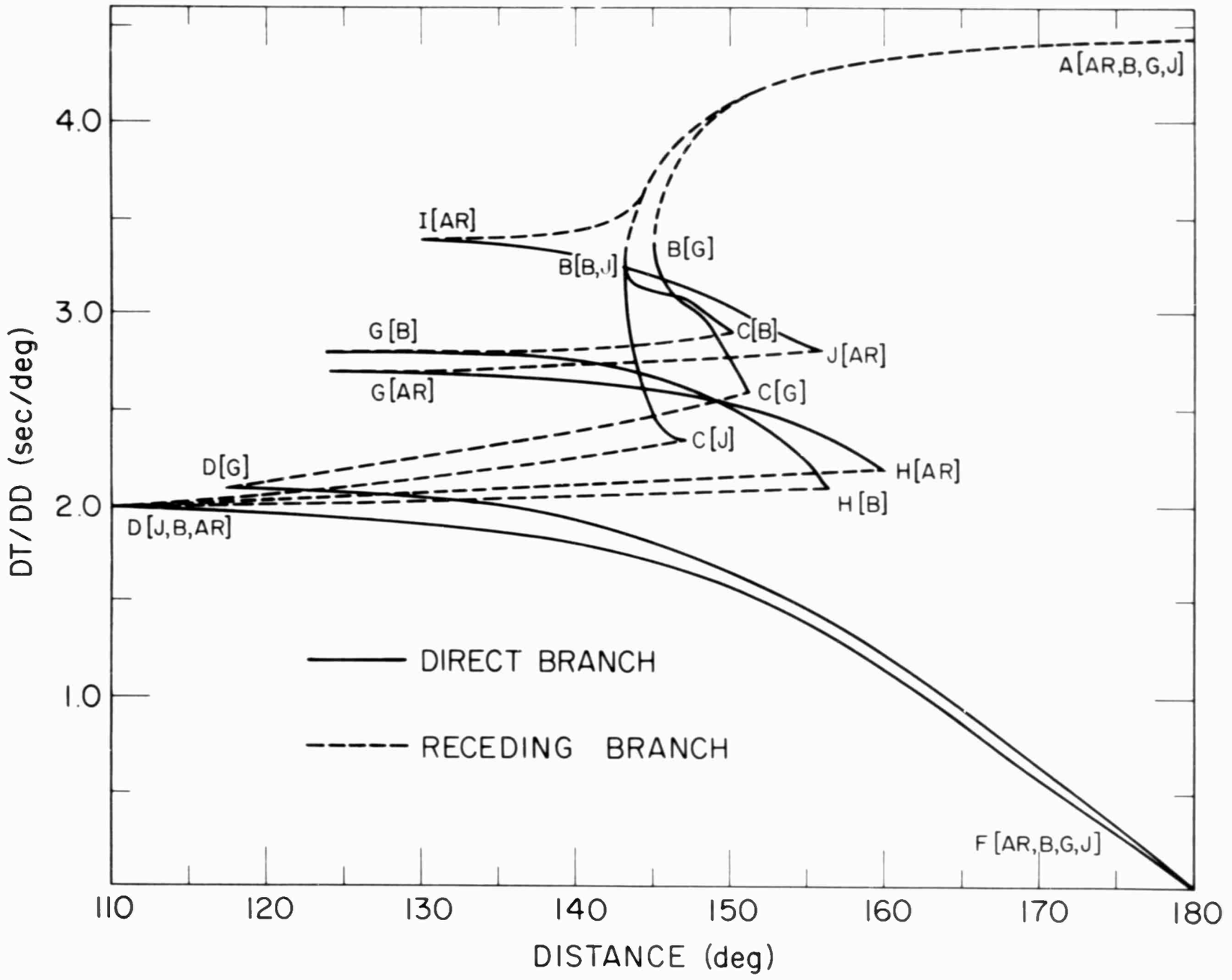
A[AR,B,G,J]
I[AR]
B[B,J]
B[G]
G[B]
C[B]
J[AR]
G[AR]
C[G]
C[J]
D[G]
H[AR]
H[B]
D[J,B,AR]
DIRECT BRANCH
RECEDING BRANCH
F[AR,B,G,J]
4.0
3.0
2.0
1.0
DT/DD (sec/deg)
110
120
130
140
150
160
170
180
DISTANCE (deg)

Fig. 2

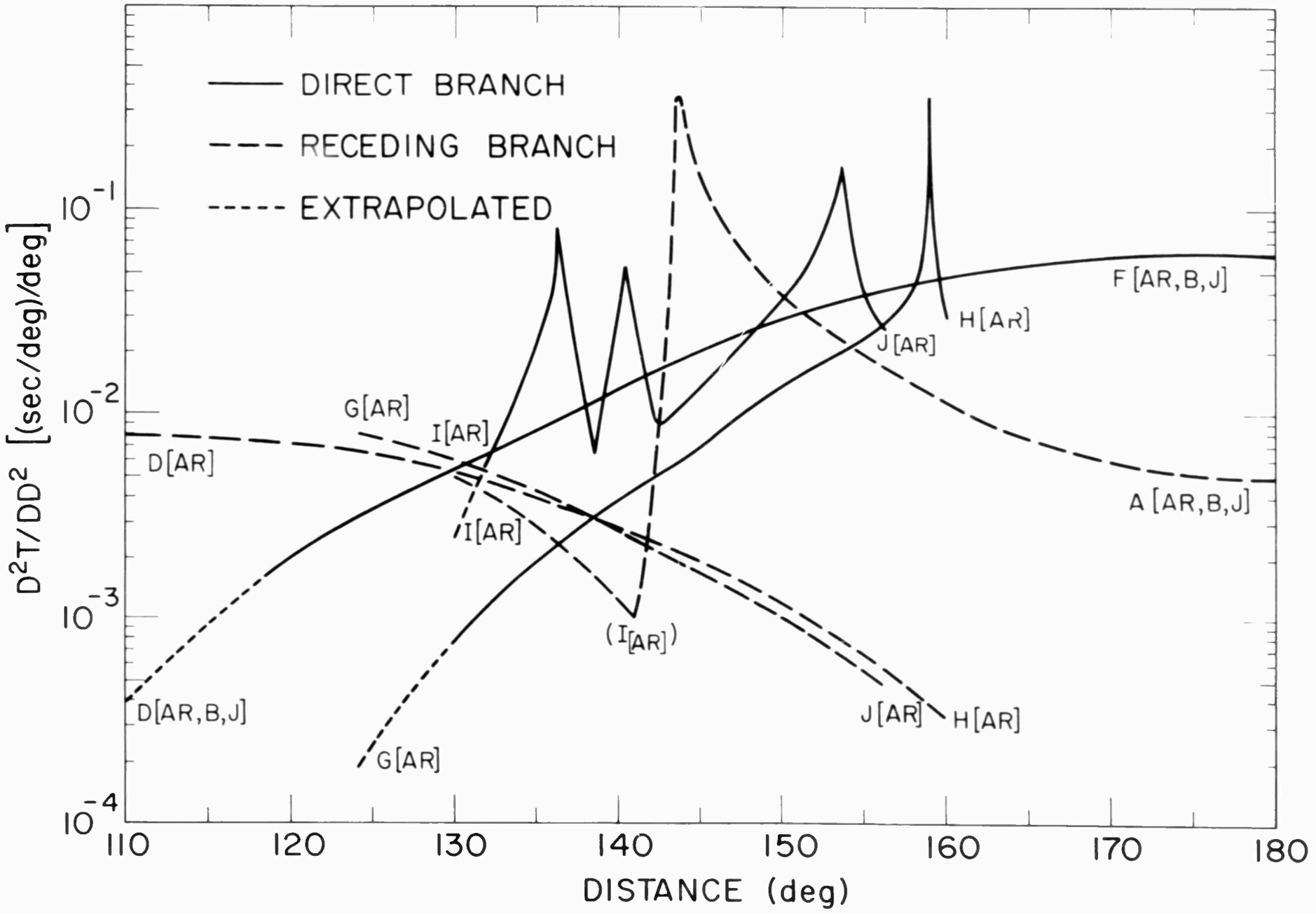
DIRECT BRANCH
RECEDING BRANCH
EXTRAPOLATED
D^2T/DD^2 [(sec/deg)/deg]
10^{-1}
10^{-2}
10^{-3}
10^{-4}
110
120
130
140
150
160
170
180
DISTANCE (deg)
F [AR,B,J]
H[AR]
J[AR]
G[AR]
I[AR]
D[AR]
A [AR,B,J]
I[AR]
(I[AR])
D[AR,B,J]
J[AR]
H[AR]
G[AR]

Fig. 3

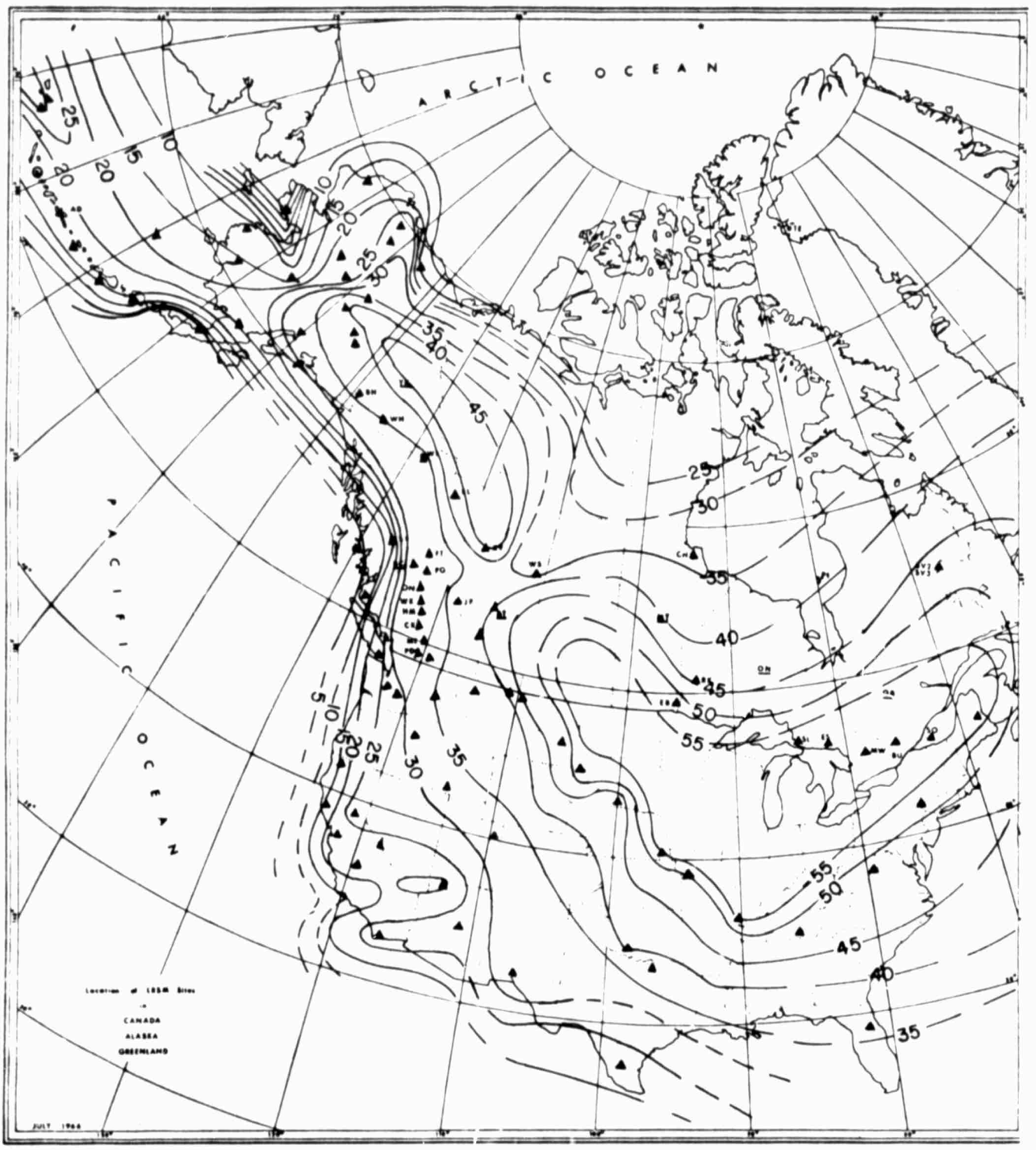

Fig. 4

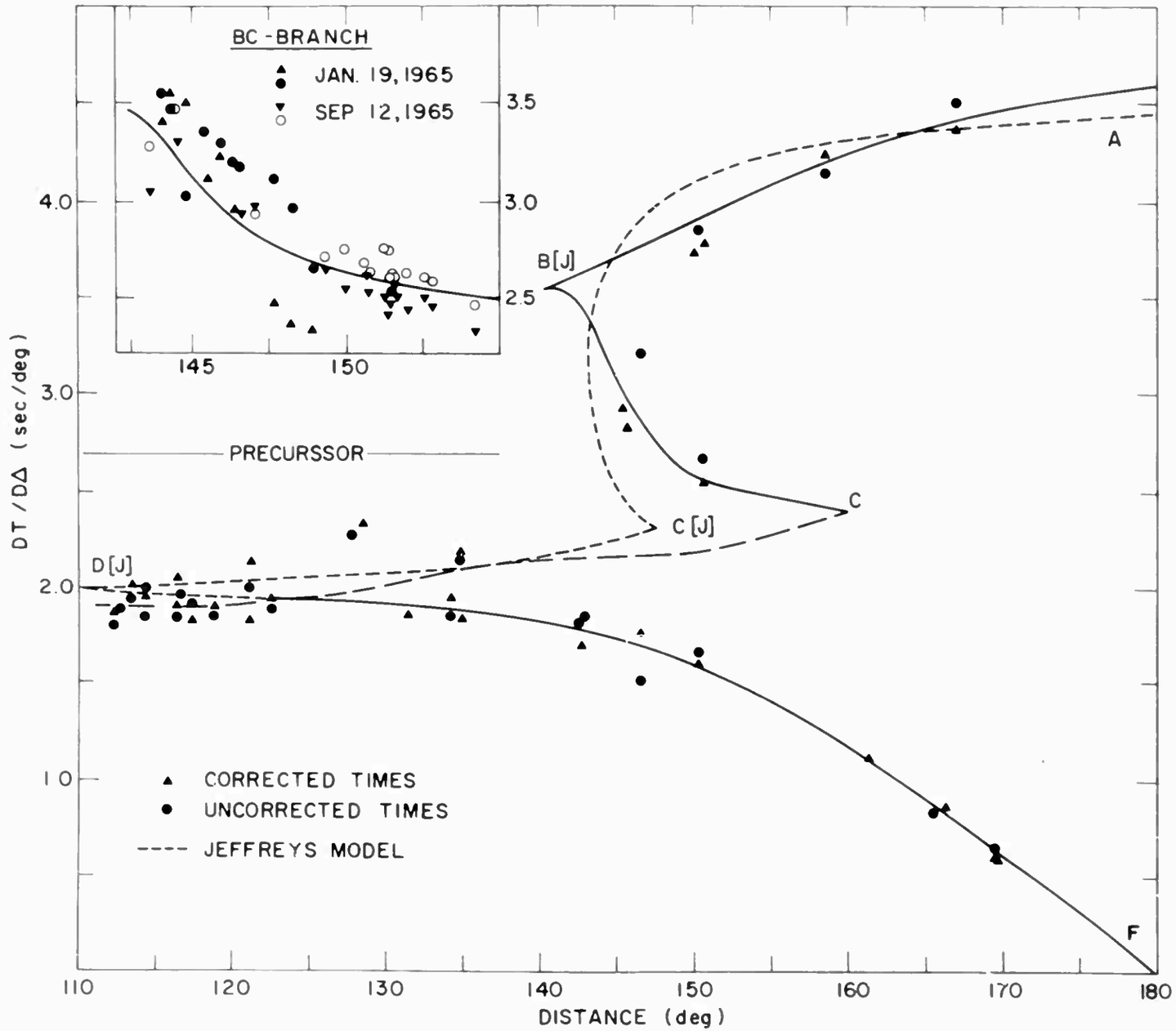
BC - BRANCH
JAN. 19, 1965
SEP 12, 1965
3.5
3.0
2.5
145
150
4.0
3.0
2.0
1.0
DT / DΔ (sec / deg)
PRECURSSOR
A
B[J]
C
C [J]
D[J]
F
CORRECTED TIMES
UNCORRECTED TIMES
JEFFREYS MODEL
110
120
130
140
150
160
170
180
DISTANCE (deg)

Fig. 5

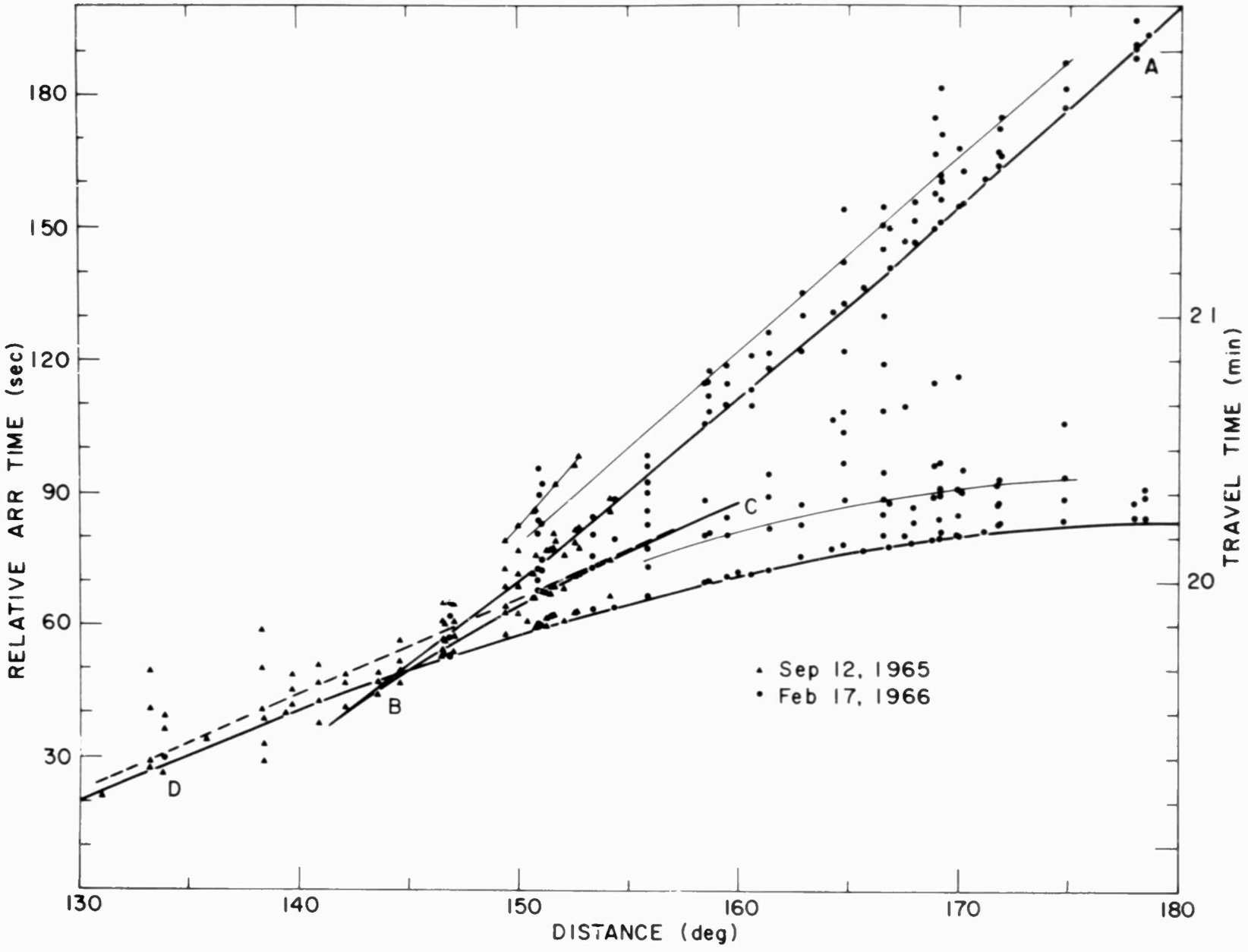
RELATIVE ARR TIME (sec)
180
150
120
90
60
30
TRAVEL TIME (min)
21
20
130
140
150
160
170
180
DISTANCE (deg)
A
B
C
D
Sep 12, 1965
Feb 17, 1966

Fig. 6

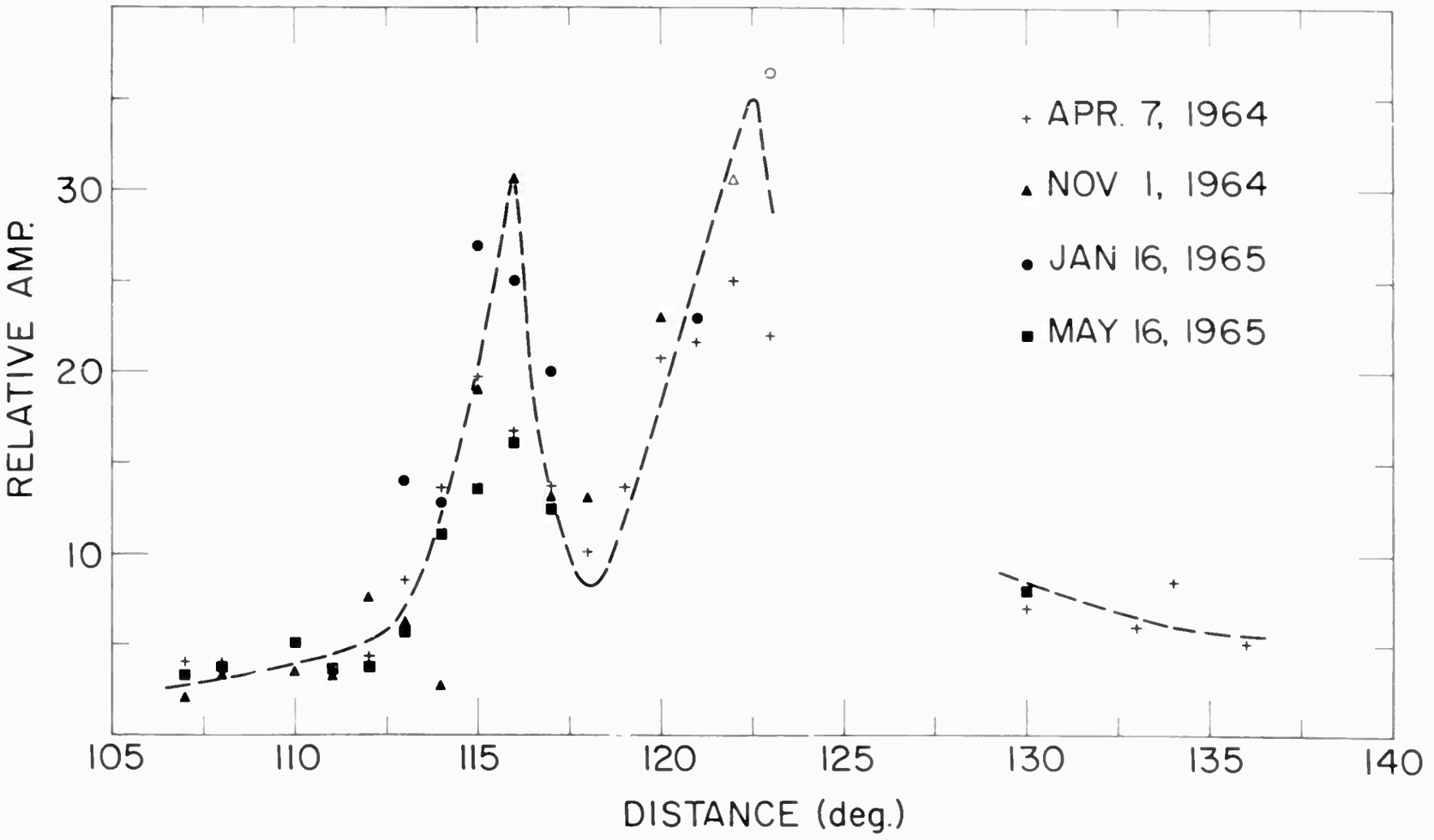
RELATIVE AMP.
30
20
10
105
110
115
120
125
130
135
140
DISTANCE (deg.)
APR. 7, 1964
NOV 1, 1964
JAN 16, 1965
MAY 16, 1965

Fig. 7

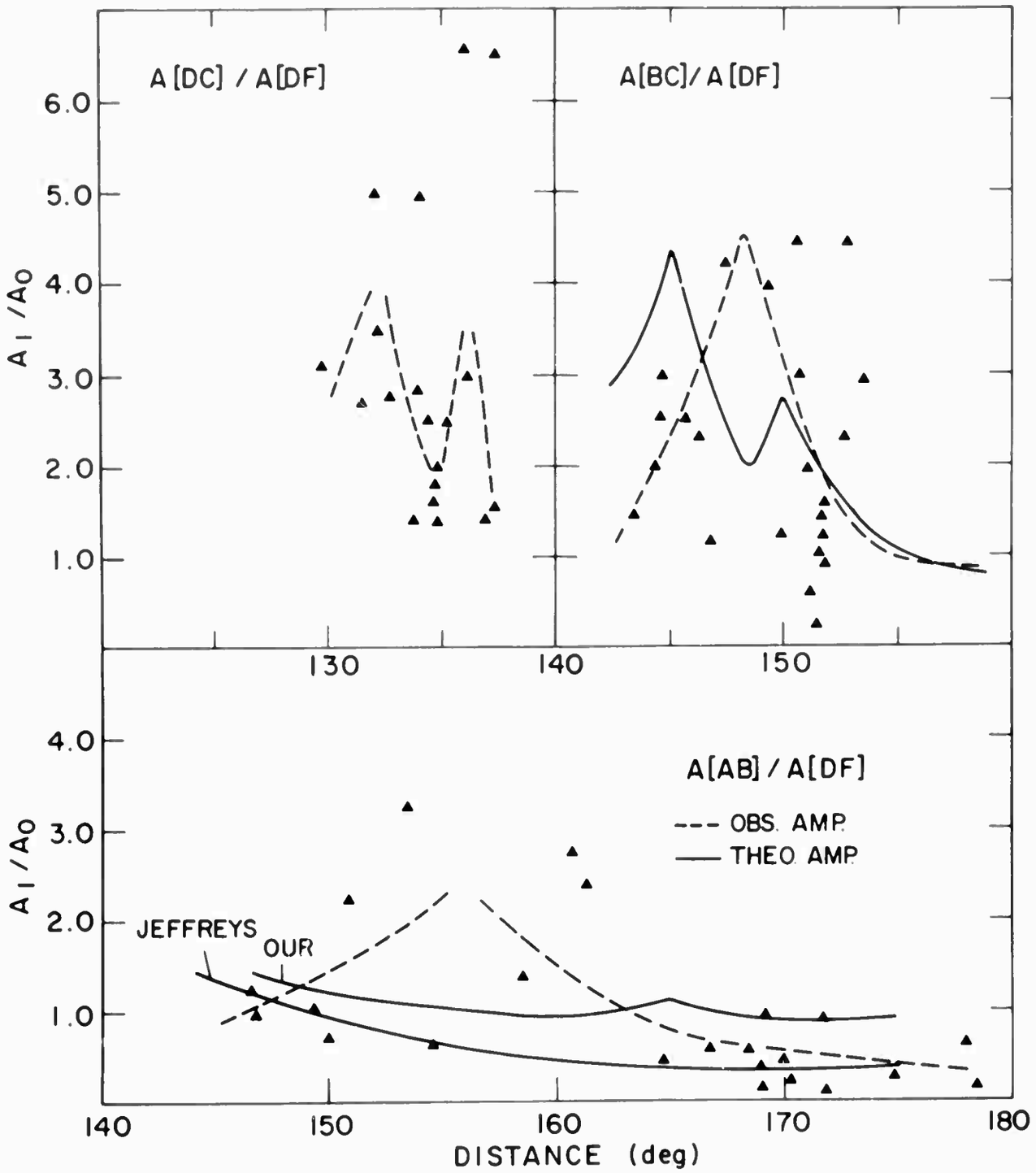
A [DC] / A[DF]
A[BC]/ A [DF]
A[AB] / A[DF]
OBS. AMP.
THEO. AMP.
JEFFREYS
OUR
A1 /A0
DISTANCE (deg)
1.0
2.0
3.0
4.0
5.0
6.0
130
140
150
160
170
180

Fig. 8

Fig. 9

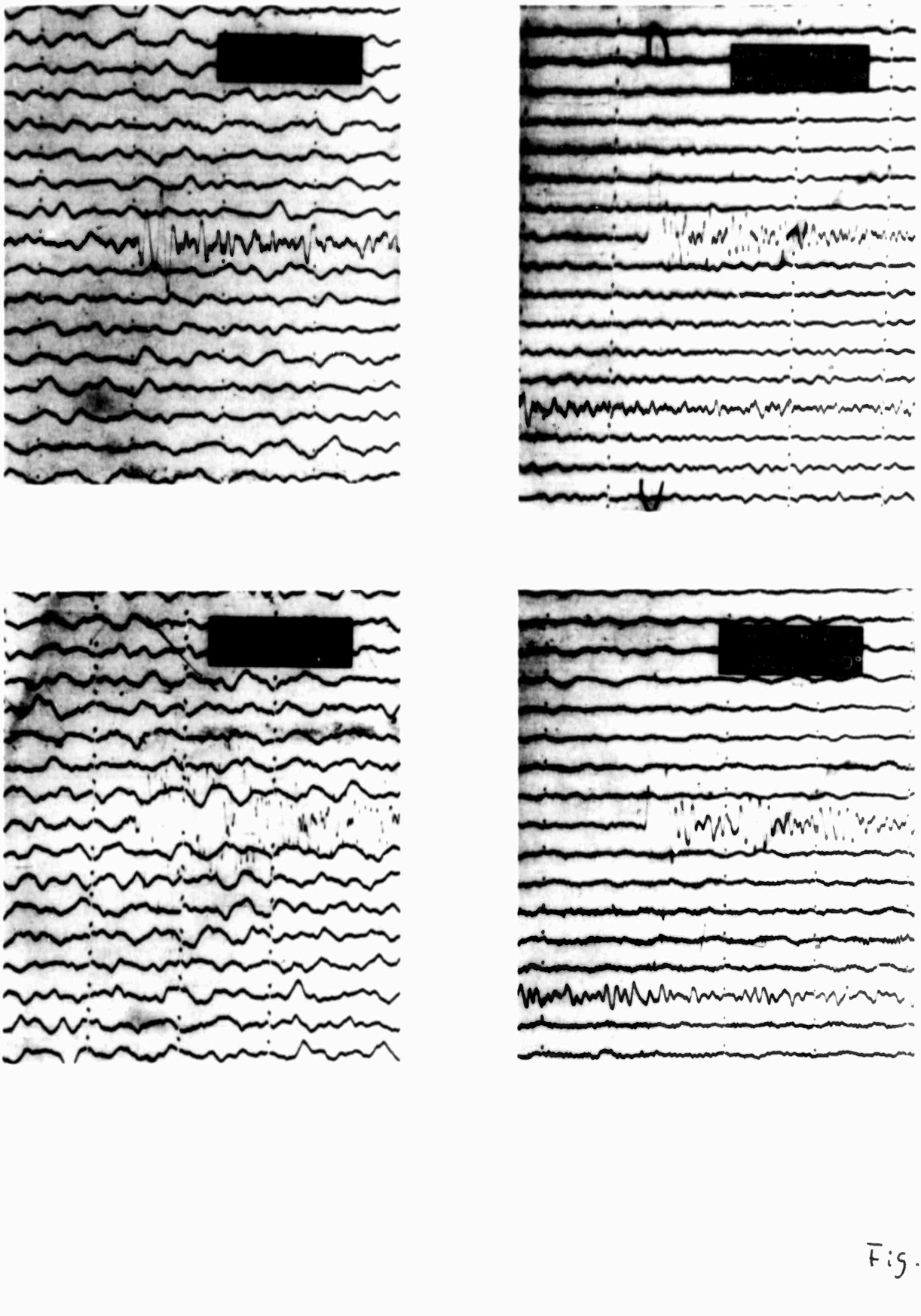

Fig. 10

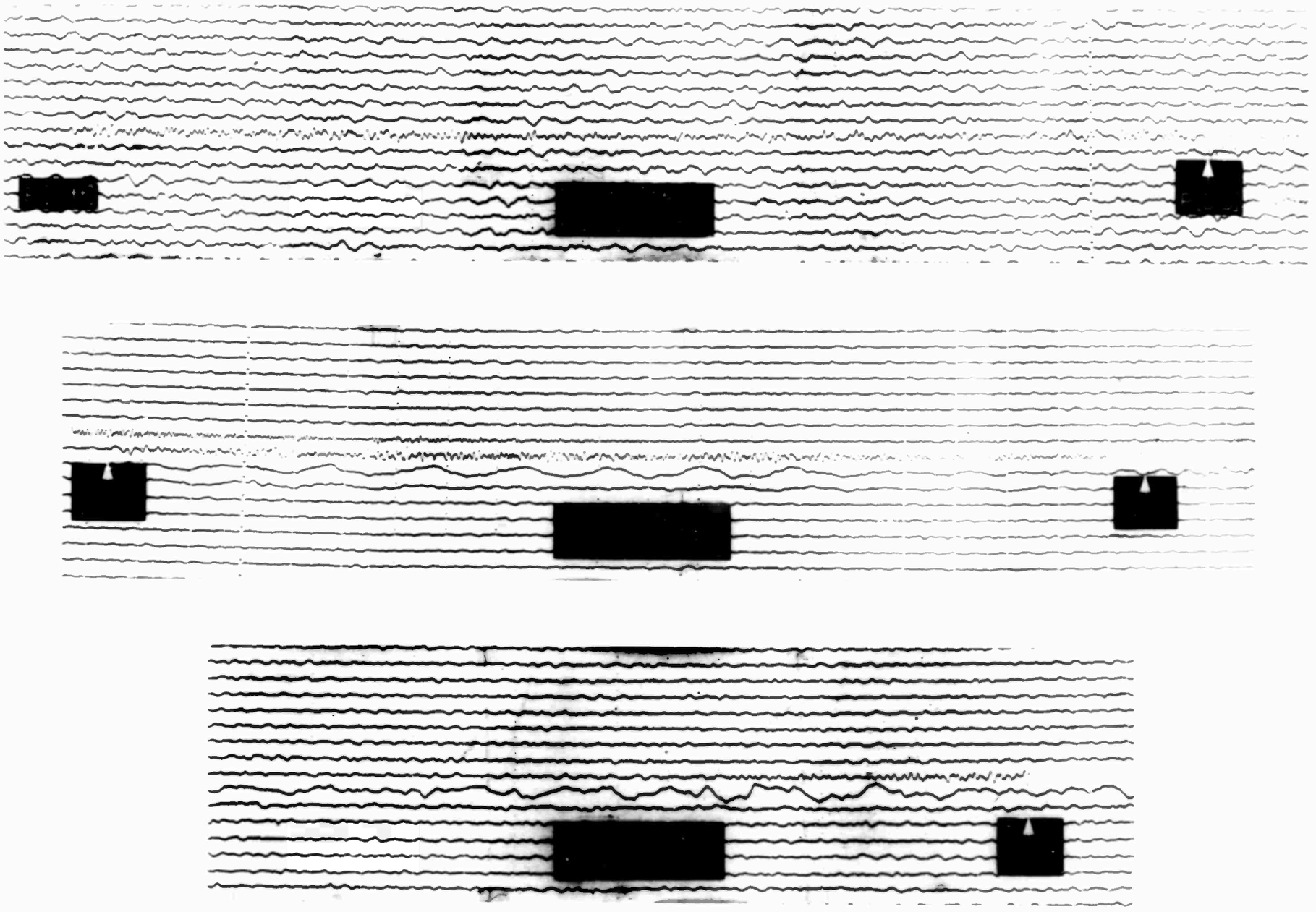

Fig. 11

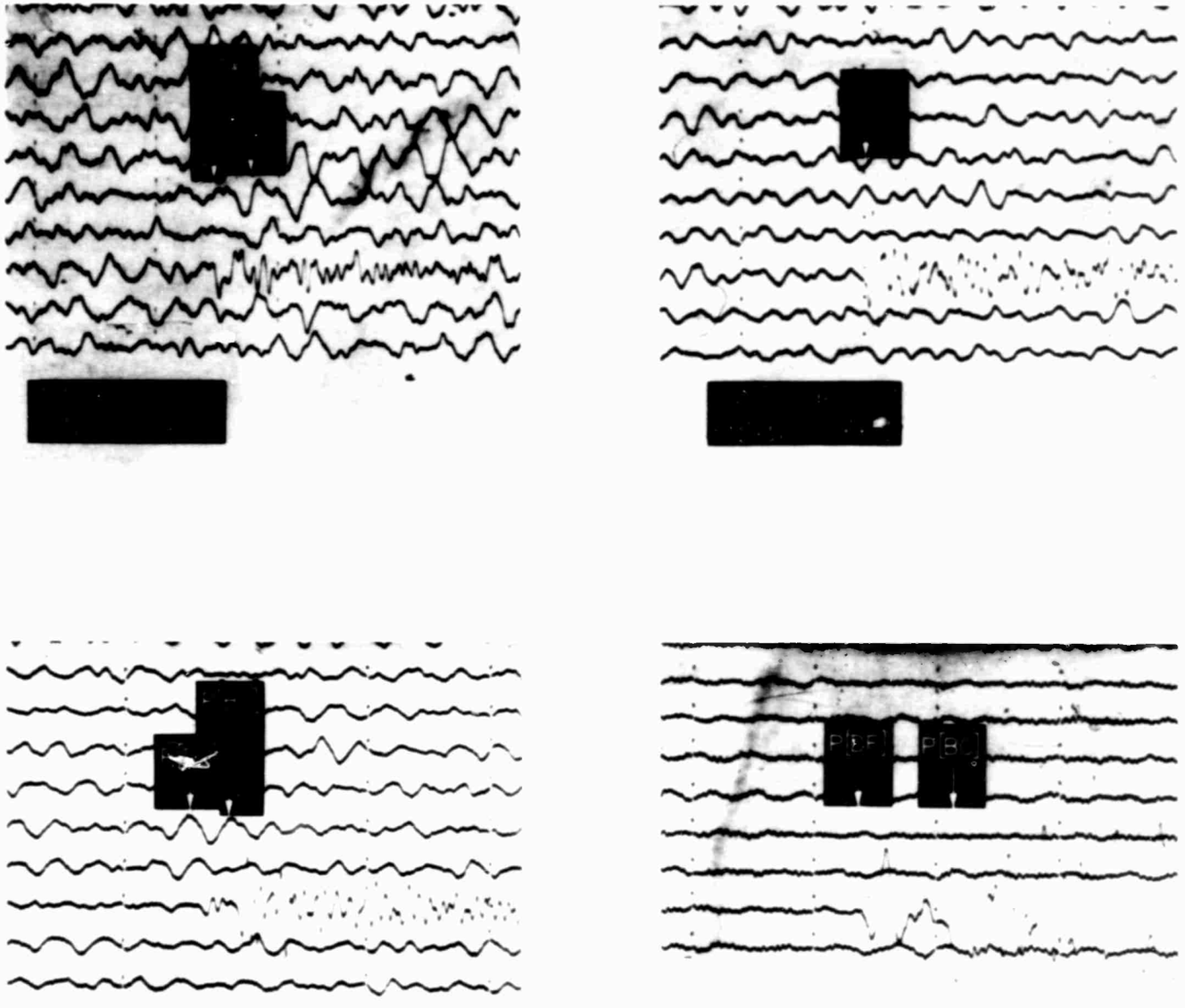

Fig. 12

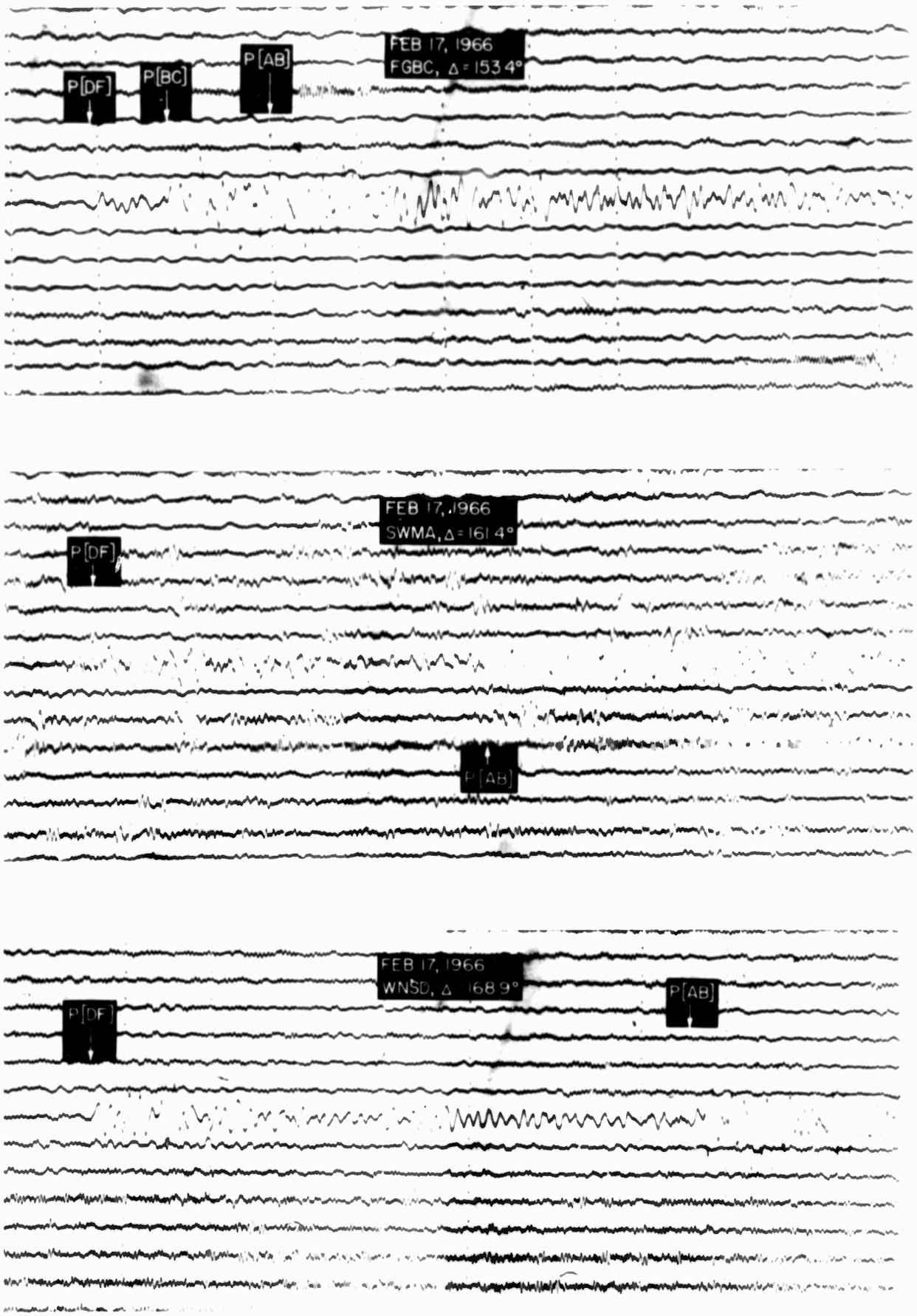
FEB 17, 1966
FGBC, Δ = 153.4°
P[DF]
P[BC]
P[AB]
FEB 17, 1966
SWMA, Δ = 161.4°
P[DF]
P[AB]
FEB 17, 1966
WNSD, Δ = 168.9°
P[DF]
P[AB]

Fig. 13

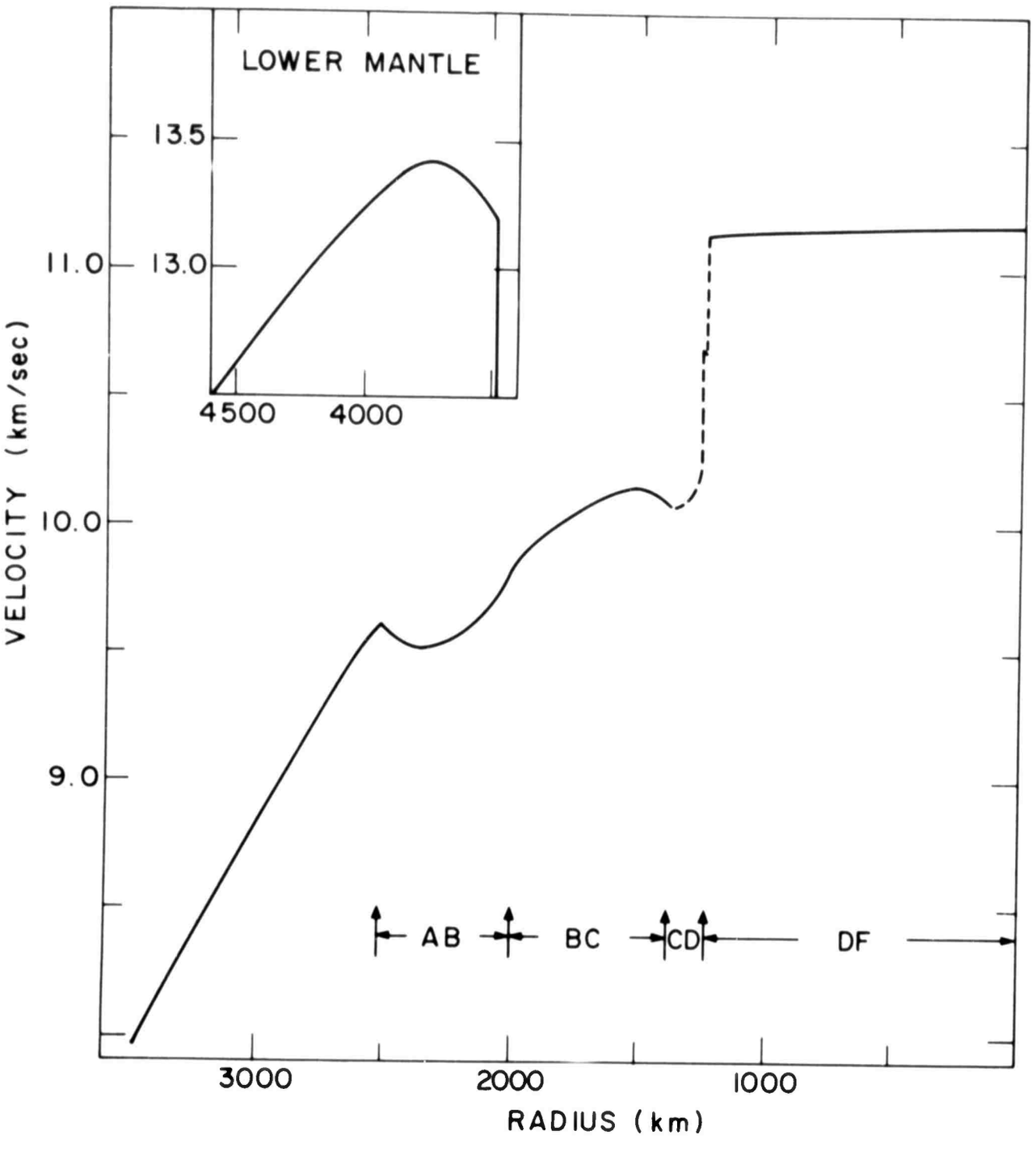
LOWER MANTLE
13.5
13.0
4500
4000
11.0
10.0
9.0
VELOCITY (km/sec)
AB
BC
CD
DF
3000
2000
1000
RADIUS (km)

Fig. 14

II.2 Direct Measurement of $dT/d\Delta$

(E.S. Husebye)

A very common problem in seismological research is the measurement of the apparent velocity or the wave parameter $p = dT/d\Delta$ over a seismograph network. Several methods here have been developed (Press, 1954; Aki, 1963; Kelly, 1964; Johnson, 1967; Knopoff et al., 1967) which are fully adequate for their special purpose. However, the above methods are limited in some ways, i.e. they are not applicable to an arbitrarily spaced, super large seismic array (Jansson and Husebye, 1967) where the only known parameters are relative arrival times and station coordinates. Recently, Chinnery and Toksöz, 1967, devised a simple least square method for measuring $dT/d\Delta$ directly from LASA data, assuming a plane wave front. Husebye and Toksöz, 1968, extended this method to cover the general case by introducing spherical coordinates and representing the wave front as a second order surface, i.e. that a Taylor expansion of T gives a second order polynomia in ϕ (latitude) and λ (longitude) whose coefficients are estimated by regression analysis. We then compute azimuth, $dT/d\Delta$ and $d^2T/d\Delta^2$. The problem to be dealt with here is to improve the latter method by transformations of the independent variables ϕ and λ. In short, our goal is to express the response surface of T in a simple form, and thus increase the applicability of the above method. It should be noted that the $dT/d\Delta$ and $d^2T/d\Delta^2$ parameters are much more sensitive to reading and identification errors than the arrival time T.

SYMBOLS

$\bar{\alpha}_i$, 1 x p_i vector containing the unknown transformation coefficients

$\alpha_{ij}^{(o)}$, j^{th} elements of $\bar{\alpha}_i$ for the first iteration of the i^{th} transformation

$\bar{a}_i$, estimated values of $\bar{\alpha}_i$

$\bar{\beta}$, a vector representing regression coefficients

$\bar{b}$, estimated values of $\bar{\beta}$

C , $(k + i) \times (k + i)$ matrix, c_{ij} is an element of C

Δ , epicentral distance

$\bar{e}_\phi, \bar{e}_\lambda$, unit vectors pointing north and east

$E( )$, expected values

η , expected value of T

γ , azimuth angle

n , no. of observations

ϕ, λ , latitude and longitude

Φ, Λ, latitude and longitude

σ^2 , variance

s^2 , estimate of σ^2

T , dependent variable or relative arrival time

$\bar{x}_i$, 1 x k vector containing independent variables

Y , $[n \times (k + i)]$ matrix constituted of n z-vectors

$\bar{y}_i$, a vector consisting of transformed elements of $\bar{x}_i$

$\bar{z}_i$, a vector consisting of transformed elements of ϕ and λ

THEORY

In the present investigation we suppose that the errors in the T's are at least approximately normal and independently distributed with constant variance. We shall concentrate on finding transformations in the ϕ and λ to reduce the T-function to as simple form as possible. Our aim is to work with a polynomial of low degree in the transformed variables rather than a polynomial of higher degree in the original variable. The procedure outlined here is based on a method described by Box and Tidwell (1962).

We first start with a short outline of Box and Tidwell's method which is as follows. Suppose observations T_i; $i = 1,\ldots,n$ are available at n sets of conditions $\bar{X}_i$, $i=1,\cdots,n$ where $\bar{X}_u$ is a $k \times 1$ vector giving the levels of the x's for the uth observation. Suppose further that:

$$E(T_u) = \eta_u \quad \text{and} \quad E(T_u - \eta_u)(T_v - \eta_v) = \begin{cases} \sigma^2, & u = v \\ 0, & u \neq v \end{cases} \qquad (1)$$

where σ^2 is unknown. Assuming that the response can be closely represented over the region of interest by some simple function:

$$\eta = f(\bar{\xi}, \bar{\beta}) \qquad (2)$$

where the elements $\xi_1, \cdots, \xi_k$ of the vector $\bar{\xi}$ are the x's transformed in some suitable way so that:

$$\bar{\xi}_i = \xi_i(x_i, \bar{\alpha}_i) \tag{3}$$

where $\bar{\alpha}_i$ is a p-dimensional vector with elements $\alpha_{i1}, \cdots \alpha_{ij}, \cdots, \alpha_{ip_i}$ the unknown constants of the ith transformation. The functional relationship also involves L unknown constants whose values $\beta_1, \cdots, \beta_L$ are the elements of the $\bar{\beta}$-vector and depend upon the particular transformations of ξ's employed, i.e. they depend on the choice of the α's. Suppose $\bar{\alpha}_i^{(0)} = [\alpha_{i1}^{(0)}, \cdots, \alpha_{ip_i}^{(0)}]$ are the first guesses for the constants of the ith transformation. A natural first guess would be to use untransformed data, that is $\alpha_{ij} = 1.0$. We then write $\bar{\xi}_u^{(0)}$ for the vector whose ith element is $\xi_i = \xi_i(x_{iu}, \bar{\alpha}_i^{(0)})$. Expanding about these guessed values and ignoring terms of second and higher orders in $(\alpha_{ij} - \alpha_{ij}^{(0)})$, we have approximately

$$\eta_u = f(\bar{\xi}_u^{(0)}, \bar{\beta}) + \sum_{i=1}^{k} \sum_{j=1}^{p_i} (\alpha_{ij} - \alpha_{ij}^{(0)}) \left\{ \frac{\partial f(\bar{\xi}, \bar{\beta})}{\partial \alpha_{ij}} \right\}_{\substack{\bar{\xi} = \bar{\xi}_u^{(0)} \\ \bar{\alpha}_i = \bar{\alpha}_i^{(0)}}} \tag{4}$$

We also have:

$$\left\{ \frac{\partial f(\bar{\xi}, \bar{\beta})}{\partial \alpha_{ij}} \right\}_{\substack{\bar{\xi} = \bar{\xi}_u^{(0)} \\ \bar{\alpha}_i = \bar{\alpha}_i^{(0)}}} = \left\{ \frac{\partial f(\bar{\xi}, \bar{\beta})}{\partial \xi_{iu}} \right\}_{\bar{\xi} = \bar{\xi}_u^{(0)}} \left\{ \frac{\partial \xi_{iu}}{\partial \alpha_{ij}} \right\}_{\bar{\alpha}_i = \bar{\alpha}_i^{(0)}} \tag{5}$$

The quantities $\left\{ \partial \xi_{iu} / \partial \alpha_{ij} \right\}_{\bar{\alpha}_i = \bar{\alpha}_i^{(0)}}$ are obtainable from equation (3), while the quantities $\left\{ \partial f(\bar{\xi}, \bar{\beta}) / \partial \xi_i \right\}_{\bar{\xi} = \bar{\xi}_u^{(0)}}$ must be estimated in some way. This can be done conveniently

by making a preliminary fitting of the observations to $\eta_u = f(\bar{\xi}, \bar{\beta})$ by the least square method or any other suitable procedure. By differentiating the fitted expression $T_u = f(\bar{\xi}_u^{(0)}, \bar{b})$ where $\bar{b}$ is the least square estimate of $\bar{\beta}$, we may obtain approximate values for the quantities $\{\partial f(\bar{\xi}, \bar{\beta})/\partial \xi_i\}_{\bar{\xi}=\bar{\xi}_u^{(0)}}$.

The $n \sum_{i=1}^{k} p_i$ approximate values of

$$\left\{\frac{\partial f(\bar{\xi}, \bar{\beta})}{\partial \alpha_{ij}}\right\}_{\substack{\bar{\xi}=\bar{\xi}_u^{(0)} \\ \bar{\alpha}_i=\bar{\alpha}_i^{(0)}}} \tag{6}$$

which can now be calculated, provide a set of "independent variables' from which we can obtain the adjustments to the transformation constants by refitting the observations to the whole expression on the right side of equation (4). These adjusted constants can now take the place of the "first quesses" in the above calculation, and the whole cycle is repeated.

Seismological Application

The arrival time T of a seismic wave usually increases monotonically with epicentral distance, and thus might be represented as a second order polynomia in station coordinates φ and λ. As the earth is approximately spherical, we can safely ignore the earth radius in the above function. However, it would be preferable to work with an essential linear function in φ and λ, as the number of station records available for analysis usually is limited, say 5-15. Note that the above approach makes us quite free to consider any number of seismological stations as an array which we might use for measuring $dT/d\Delta$. As array geometry, azimuth, epicentral distance and the wave under consideration will vary,

the function which best fits the observed response surface T will vary too. The Box and Tidwell method outlined above should therefore by appropriate for direct measurement of $dT/d\Delta$, as the response surface here is not tied to a single class of functions. For example

$$\xi_i = \begin{cases} x_i^{\alpha_i} & \alpha_i \neq 0 \\ \ln x_i & \alpha_i = 0 \end{cases} \qquad (7)$$

includes many forms commonly found useful, like square root and reciprocal transformations. The above procedure can easily be adapted to transformations of the dependent variable too. For example, assume we make guesses different from 1.0 for the values of α_{ij} in the first iteration. We can always regard these new variables, including any transformation of the dependent variable, as being the basic variables. When a second iteration is performed, only the $X_i^{\alpha_i}$ will be taken as new basic variables.

Leaving the general notation above, and returning to our problem, namely to find the response surface of the relative arrival time over an arbitrary array, we then have:

$$\bar{T} = \beta_0 z_0 + \beta_1 z_1 + \beta_2 z_2 + \cdots + \beta_k z_k \qquad (8)$$

where z_0 is a dummy variable always equal 1.0, $z_1 = \phi^{\alpha_1}$, $z_2 = \lambda^{\alpha_2}$ etc., k is number of parameters in the T expansion. Our first guess is that $\alpha_1 = \alpha_2 = 1.0$, and rewriting of eq. (4) gives

$$T_u = \bar{T} + (\alpha_1 - 1.0)\,\partial\bar{T}/\partial\alpha_1 + (\alpha_2 - 1.0)\,\partial\bar{T}/\partial\alpha_2 \qquad (9)$$

From eq. (5) we have:

$$\overline{T_u} = \overline{T} + (\alpha_1 - 1.0)\cdot \partial T/\partial \phi \cdot \phi \ln \phi + (\alpha_2 - 1.0)\partial T/\partial \lambda \cdot \lambda \ln \lambda \qquad (10)$$

We start by applying the method of least square to eq. (8). Differentiating this equation with respect to ϕ and λ, we may calculate $\partial \hat{\overline{T}}/\partial \phi$ and $\partial \hat{\overline{T}}/\partial \lambda$. The sign roof means statistical averaging. Construction of new, independent variables gives:

$$z_{k+1} = \partial \hat{\overline{T}}/\partial \phi \cdot \phi \ln \phi \;, \; z_{k+2} = \partial \hat{\overline{T}}/\partial \lambda \cdot \lambda \ln \lambda \qquad (11)$$

When refitting, we use the equation:

$$\overline{T_u} = \beta_0 z_0 + \beta_1 z_1 + \cdots + (\alpha_1 - 1.0) z_{k+1} + (\alpha_2 - 1.0) z_{k+2} \qquad (12)$$

Thus we get estimates $(a_1 - 1.0)$ and $(a_2 - 1.0)$ of $(\alpha_1 - 1.0)$ and $(\alpha_2 - 1.0)$. The ϕ^{a_1} and λ^{a_2} may be treated as ϕ and λ in further iterations.

ADEQUACY OF TRANSFORMATION

It is desirable to have some measure of precision of the a_i quantities, both for deciding number of iterations and whether it is worthwhile to transform the original variables. The variance of a_i, $Var(a_i)$ might be calculated in the ordinary way for estimated least square coefficients. Imagining matrix notation applied to eq. (12), then

$$Var(a_i) = \sigma^2 \cdot c_{k+i,\,k+i} \qquad (13)$$

where $c_{k+i,k+i}$ is the $(k+i)$ diagonal element in the matrix $(Y'Y)^{-1}$. σ^2 is the variance of T, and its estimated value is the residual mean square value s^2 of $\hat{T}$.

However, when the number of observations is small, allowances are necessary for the β-estimates included in the Z_{k+i} variables. When working with transformed linear functions, this difficulty may be avoided by using Fieller's theorem (1940). However, the straight forward method here is to test the transformations by calculating standard parameters like sum of squares around regression and due to regression, lack of fit, etc.

CALCULATION OF AZIMUTH, $dT/d\Delta$ AND $d^2T/d\Delta^2$

When the above steps are finished, the travel time variation over the array is expressible as:

$$\hat{T} = b_0 z_0 + b_1 z_1 + \cdots + b_k z_k \qquad (14)$$

where $z_0 = 1.0$, $z_1 = \phi^{a_1}$, $z_2 = \lambda^{a_2}$, $z_3 = \phi^{2a_1}$, $\cdots$. The variance of T_i is, setting $C = (Y'Y)^{-1}$

$$Var(\bar{T}_i) = \sigma^2 (\bar{z}_i' C \bar{z}_i) \qquad (15)$$

where $\bar{z}_i = (1\ z_{1i} \cdots z_{ki})$.

Differentiating the scalar T_i, remembering that we are using spherical coordinates, we get if T_i is a second order polynomia:

$$\partial \hat{T}_i / \partial \phi\, \bar{e}_\phi = U_i \bar{e}_\phi = (b_1 + 2b_3 \phi_i^{a_1} + b_4 \lambda_i^{a_2}) a_1 \phi_i^{a_1 - 1} \cdot \bar{e}_\phi \qquad (16)$$

$$\partial \hat{T}_i / \partial \lambda\, \bar{e}_\lambda = V_i \bar{e}_\lambda = (b_2 + 2b_5 \lambda^{a_2} + b_4 \phi_i^{a_1}) a_2 \lambda_i^{a_2 - 1} / \cos\phi_i \cdot \bar{e}_\lambda$$

First order expansion of (16) gives (U -term only):

$$U_i + dU_i = \left[b_1 + db_1 + 2(b_3 + db_3)\phi_i^{a_1} + (b_4 + db_4)\lambda_i^{a_2}\right] a_1 \phi_i^{a_1 - 1.} \qquad (17)$$

Since we have assumed that the error ΔT_i accompanying the ith observation, is an independent Gaussian variable, having zero mean and variance σ^2, db_i and dU_i will also be Gaussian variables with zero means. Performing statistical averaging over eq. (17), we have for the variance of U_i:

$$Var(U_i) = \left[\left(db_1 + 2db_3\phi_i^{a_1} + db_4\lambda_i^{a_2}\right) a_1 \phi_i^{a_1 - 1.0}\right]^2 \qquad (18)$$

Since we are averaging over the db_i terms, we may write:

$$\begin{aligned} Var(U_i) = \Big[& Var(b_1) + 4\phi_i^{2a_1} \cdot Var(b_3) + \lambda_i^{2a_2} \cdot Var(b_4) \\ & + 4\phi_i^{a_1} Cov(b_1 b_3) + 2\lambda_i^{a_2} Cov(b_1 b_4) \\ & + 4\phi_i^{a_1}\lambda_i^{a_2} Cov(b_3 b_4)\Big] \cdot \left[a_1 \phi_i^{a_1 - 1.0}\right]^2 \end{aligned} \qquad (19)$$

where $Cov(b_1 b_3)$ means covariance $b_1 b_3$ and corresponds to σ^2 multiplied with the c_{13} element of the C-matrix given above. In similar ways we may calculate the terms $Var(V_i)$ and $Cov(U_i V_i)$.

The azimuth of the wavefront is:

$$\tan \gamma_i = \frac{V_i}{U_i} \qquad (20)$$

First order expansion of both sides of eq. (20) gives:

$$\tan\gamma_i + \frac{d\gamma_i}{\cos^2\gamma_i} = \frac{V_i}{U_i} + \frac{U_i\,dV_i - V_i\,dU_i}{U_i^2} \qquad (21)$$

Using eq. (20) we get:

$$d\gamma_i = \cos^2\gamma_i \left[\frac{dV_i}{U_i} - \frac{V_i\,dU_i}{U_i^2}\right] = \sin\gamma_i\cos\gamma_i\left[\frac{dV_i}{V_i} - \frac{dU_i}{U_i}\right] \qquad (22)$$

Thus the error in γ_i is Gaussian with zero mean. The variance of γ_i is:

$$\mathrm{Var}(\gamma_i) = \sin^2\gamma_i\cos^2\gamma_i\left[\frac{\mathrm{Var}(V_i)}{V_i^2} - \frac{2\,\mathrm{Cov}(U_iV_i)}{U_iV_i} + \frac{\mathrm{Var}(U_i)}{U_i^2}\right] \qquad (23)$$

The wave parameter $p = d\hat{T}/d\Delta$ is:

$$p_i^2 = U_i^2 + V_i^2 \qquad (24)$$

Differentiating eq. (24), we get:

$$p_i\,dp_i = U_i\,dU_i + V_i\,dV_i \qquad (25)$$

Also dp_i is Gaussian, and the variance of p_i is:

$$\mathrm{Var}(p_i) = p_i^{-2}\left[U_i^2\,\mathrm{Var}(U_i) + 2U_iV_i\,\mathrm{Cov}(U_iV_i) + V_i^2\,\mathrm{Var}(V_i)\right] \qquad (26)$$

The $dp/d\Delta$ or $d^2T/d\Delta^2$ term is very important in interpretation of amplitude data, and it might be worthwhile to calculate when our observations are very precise. Normally, this quantity is obtained from $dT/d\Delta$ observations, but for the sake of completeness, the calculation procedure will be outlined. By taking the directional derivative of the p-vector, we get

for $d^2T/d\Delta^2$ - vector:

$$\overline{d^2T_i/d\Delta^2} = \left[A_i \cdot \nabla\right] \bar{P}_i = \left[\cos\gamma_i \bar{e}_\phi + \sin\gamma_i \bar{e}_\lambda\right] \cdot \left[\frac{\partial}{\partial\phi}\bar{e}_\phi + \frac{\partial}{\cos\phi_i \partial\lambda}\bar{e}_\lambda\right] \cdot \left[U_i \bar{e}_\phi + V_i \bar{e}_\lambda\right] \tag{27}$$

Introducing new vectors L and M:

$$\bar{L}_i = \left[\cos\gamma_i \frac{\partial U_i}{\partial\phi} + \frac{\sin\gamma_i}{\cos\phi_i}\frac{\partial U_i}{\partial\lambda_i}\right]\bar{e}_\phi$$
$$\bar{M}_i = \left[\cos\gamma_i \frac{\partial V_i}{\partial\phi} + \frac{\sin\gamma_i}{\cos\phi_i}\frac{\partial V_i}{\partial\lambda}\right]\bar{e}_\lambda \tag{28}$$

Proceeding in the same manner as we did for calculating the ϕ- vector, we have:

$$Azi_i\left(d^2\hat{T}/d\Delta^2\right) = \text{Arctan}\left(M_i/L_i\right) \tag{29}$$

$$Var\left(Azi_i\right) = \sin^2 Azi_i \cos^2 Azi_i \left[\frac{Var(M_i)}{M_i^2} - \frac{2\,Cov(L_iM_i)}{M_iL_i} + \frac{Var(L_i)}{L_i^2}\right]$$

and

$$d^2\hat{T}_i/d\Delta^2 = \left[L_i^2 + M_i^2\right]^{1/2}$$

$$Var\left(d^2\hat{T}_i/d\Delta^2\right) = \left[d^2\hat{T}_i/d\Delta^2\right]^{-2} \cdot \left[L_i^2 Var(L_i) + 2L_iM_i Cov(L_iM_i) + M_i^2 Var(M_i)\right] \tag{30}$$

A large problem in present day seismogram analysis is the existence of local travel time anomalies. This effect should be properly accounted for to avoid biased errors in the $dT/d\Delta$ estimates.

If the epicenter parameters are not given, these could be easily calculated from the estimated azimuth and $dT/d\Delta$ values if a $dT/d\Delta$ table is available. This has been demonstrated by Kelly (1964) and the procedure here is as follows.

We construct a spherical triangle whose corners and corner angles are STA($\varphi_i, \lambda_i, \gamma_i$), EPI ($\Phi, \Lambda, -$) and NPOLE($90.-, -, \lambda_i - \Lambda$). The angular lengths of the sides are ($90.-\varphi_i, 90.-\Phi, \Delta$). From these quantities and the following equations, we can easily calculate Φ and Λ.

$$\sin\Phi = \sin\varphi_i \cos\Delta_i + \cos\varphi_i \sin\Delta_i \cdot \cos\gamma_i$$
$$\cos(\lambda_i - \Lambda) = [\cos\varphi_i \cos\Delta_i + \sin\varphi_i \sin\Delta_i \cos\gamma_i] / \cos\Phi \qquad (31)$$

Due to existence of biased azimuth errors, it might sometimes be preferable to combine the above method with another one described by Husebye (1966). The latter method needs some modification for analytical usage.

Demonstration of the Method

The above method has been applied to the two arrays shown in Fig. 1. The P travel time data have been taken from Jeffreys-Bullen tables and in some cases random errors have been added. Two types of response surfaces are investigated.

$$\bar{T} = b_0 + b_1 \varphi^{a_1} + b_2 \lambda^{a_2} + b_3 \varphi^{a_1} \lambda^{a_2} \qquad (32)$$

$$\bar{T} = b_0 + b_1 \varphi^{a_1} + b_2 \lambda^{a_2} + b_3 \varphi^{a_1} \lambda^{a_2} + b_4 \varphi^{2a_1} + b_5 \lambda^{2a_2} \qquad (33)$$

Input data like station coordinates, travel times and also true $dT/d\Delta$ and azimuth values, are given in Table 1. The results are displayed in Tables 2 and 3, and need a few comments. For the second order response surface given by

eq. (33), no improvement is gained by the iteration process. The new α -coefficents are very close to 1.0 having standard errors around 0.6. This result reflects the very nature of our problem, i.e. to measure the slope of a surface which deviates slightly from a shell. For the first order response surface, the new α -coefficents give sometimes a small improvement in the $dT/d\Delta$ values. In these cases it was sufficient with only one iteration. Implemented in least square analysis is that the most accurate estimate of the sought parameters corresponds to points at the center of the array, so only these values should be retained for further investigations. Important, the "center' values in Tables 2 and 3 exhibit little dependence both on the type of response surface and inclusion of random errors. For example, analysis of core phases could sometimes be performed, using only two free variables in the response surface.

Discussion

The method outlined above, favors a somewhat different approach to the analysis of travel time data. Instead of using many events recorded at widely scattered stations, it is preferable to use fewer events recorded in a relatively dense station network. If digitized data are available, the proper procedure might be as follows. The first step is to band pass and remode filter the records if this is deemed necessary. To avoid the non-linear properties of the general remode filter (Flinn, 1965), an acceptable version of this would be to rotate the seismograph system such that one of the component points in the direction of the particle motion of the phase under investigation. By weighting, the ellipti-

city of the particle motions is restricted to certain limits, and parts of the reverberation effects would be suppressed. The first order time lags are calculated from proper knowledge of focal parameters, while second order time lags are obtained by using a cross-correlation-iteration scheme (Fairborn and Gangi, 1967, see also Jansson and Husebye, 1968). Additional refienment of the arrival time values are possible when information on local velocity anomalies or station corrections are available. Essentially, the above procedure corresponds to the much used method of velocity filtering of data from small arrays.

Acknowledgments

The research reported here was supported by the Advanced Research Projects Agency and monitored by the Air Force Office of Scientific Research under Contract No. AF 49 (638) - 1763.

References

Aki, K., Crustal structure in Japan from the phase velocity of Rayleigh waves, Bull. Earthquake Res. Inst., Tokyo Univ., 39, 255-283, 1961.

Box, G.E.P. and P.W. Tidwell, Transformation of the independent variables, Technometrics, 4, 531-550, 1962.

Chinnery, M.A. and M.N. Toksöz, P-wave velocities in the mantle: I, below 700 km., B.S.S.A., 57 (2), 199-226, 1967.

Fieller, E.C. The biological standardization of insulin, Jour. Roy. Stat. Soc., Supp. 7, 1-53, 1940.

Flinn, E.A., Signal analysis using rectilinearity and direction of particle motion, Proc. IEEE, 53, 1824-1826, 1965.

Gangi, A.F. and J.W. Fairborn, Accurate determination of seismic array steering delays by an adaptive computer program, in press.

Husebye, E.S., A rapid graphical method for epicenter location, Gerlands Beiträge zur Geophysik, 75, 383-392, 1966.

Husebye, E.S. and M.N. Toksöz, On the structure of the earth's core, in press.

Jansson, B. and E.S. Husebye, On the possibilities of applying array data processing techniques to ordinary seismograph stations, Pure and Appl. Geophysics, in press.

Johnson, L.R., Array measurements of P velocities in the upper mantle, J.G.R., 72 (24), 6309-6325, 1967.

Kelly, E.J., Limited network processing of seismic signals, Rep. ESD-TDR-64-369, Lincoln Lab,,Mass. Inst. Tech., Lexington, Mass. U.S.A., 1964.

Knopoff, L., M.J. Berry and F.A. Schwab, Tripartite phase velocity observations in laterally heterogeneous regions, J.G.R., 72 (10), 2595-2601, 1967.

Press, F., Determination of crustal structure from phase velocity of Rayleigh waves, 1, Southern California, Bull. Geol. Soc. Am., 67, 1647-1688, 1956.

Figure Captions

Fig.1. Array configurations. The triangles indicate the centers of the arrays.

Table Captions

Table 1. Input data used in the application and testing of this method.

Table 2a. Calculated azimuth angles, $dT/d\Delta$ values and time residuals, assumint an eq. (32) response surface model.

Table 2b. Calculated azimuth angles, $dT/d\Delta$ values and time residuals, assuming an eq. (32) response surface model.

Table 3. Calculated azimuth angles, $dT/d\Delta$ values and time residuals, assuming an eq. (33) response surface model.

Sta. no.	Coordinates North (deg)	East (deg)	Distance (deg)	Azimuth (deg)	Travel time (sec)	dT/dΔ (sec/deg)	Model for random errors in travel time (sec)
1	34.	25.	55.04	136.29	575.70	7.28	0.0
2	32.	22.	55.44	132.44	578.60	7.24	0.0
3	32.	27.	52.44	137.28	556.50	7.47	-0.4
4	32.	29.	51.31	139.34	548.0	7.57	0.6
5	30.	25.	52.20	134.23	554.70	7.50	0.6
6	30.	20.	55.42	129.60	578.40	7.24	-0.5
7	28.	22.	52.79	130.28	559.20	7.45	1.2
8	27.	28.	48.21	135.45	524.30	7.77	0.3
9	26.	24.	50.14	130.91	539.00	7.65	-0.3
10	26.	21.	52.21	128.21	554.80	7.49	0.7
11	24.	26.	47.46	131.50	518.30	7.83	-1.8
12	24.	20.	51.73	126.12	551.20	7.53	-1.0
13	24.	30.	44.81	135.55	497.40	8.02	0.9
14	22.	24.	47.59	128.23	519.30	7.82	1.5
15	21.	29.	43.39	132.29	485.90	8.11	-0.7
Center	27.47	29.	50.70	132.47		7.62	
1	28.	30.	47.73	138.16	520.50	7.87	-0.3
2	26.	30.	46.25	136.90	508.60	7.92	1.5
3	26.	34.	43.91	141.38	490.00	8.08	-1.8
4	25	28.	46.80	134.16	513.10	7.88	0.7
5	24.	32.	43.56	137.74	487.20	8.10	0.0
6	22.	30.	46.25	136.20	508.60	8.11	1.2
7	22.	33.	41.46	137.41	470.00	8.26	0.0
8	22.	27.	45.45	131.04	502.40	7.98	-1.0
9	20.	28.	43.43	130.49	486.20	8.10	-0.5
10	20.	32.	40.67	134.69	463.50	8.25	0.6
Center	23.5	30.40	44.20	135.62		8.06	

Table 1.

NO ERRORS IN TRAVEL TIME

Sta. no.	Azimuth	First Iteration $\alpha_1 = 1.0$, $\alpha_2 = 1.0$ Std. err.	dT/dΔ (sec/deg)	Std. err.	Residual (sec)	Std. err. of travel time	Second Iteration $\alpha_1 = 1.04 \pm 0.624$, $\alpha_2 = 0.82 \pm 0.735$ dT/dΔ (sec/deg)	Std. err.	Residual (sec)	Std. err. of travel time
1	135.78	0.310	4.21	0.048	0.05	0.023	7.23	0.027	0.03	0.007
2	132.77	0.216	7.08	0.052	0.07	0.030	7.14	0.030	0.08	0.010
3	136.12	0.328	7.49	0.030	-0.01	0.021	7.48	0.017	0.00	0.006
4	137.36	0.383	7.67	0.023	0.30	0.042	7.63	0.012	0.16	0.013
5	133.92	0.216	7.44	0.001	-0.29	0.008	7.46	0.017	-0.15	0.003
6	130.42	0.236	7.04	0.050	0.19	0.032	7.15	0.029	0.08	0.010
7	130.99	0.224	7.33	0.033	-0.11	0.010	7.39	0.019	-0.04	0.003
8	134.52	0.196	7.87	0.024	-0.20	0.012	7.03	0.013	0.12	0.004
9	131.51	0.213	7.61	0.024	-0.46	0.007	7.63	0.014	-0.29	0.002
10	129.43	0.300	7.38	0.029	0.03	0.017	7.46	0.017	-0.05	0.005
11	132.00	0.202	7.90	0.029	-0.35	0.011	7.87	0.016	-0.20	0.003
12	127.87	0.392	7.43	0.027	0.39	0.039	7.54	0.016	0.18	0.012
13	134.47	0.172	8.22	0.041	0.19	0.029	8.12	0.023	0.08	0.009
14	129.87	0.295	7.87	0.032	0.01	0.022	7.87	0.018	0.10	0.007
15	132.64	0.188	8.33	0.052	0.25	0.043	8.22	0.028	0.14	0.013
Center	132.67	0.188	7.58	0.024			7.59	0.014		
		$\alpha_1 = 1.0$, $\alpha_2 = 1.0$								
1	138.59	0.568	7.59	0.080	0.22	0.026				
2	132.11	0.418	7.77	0.064	-0.30	0.013				
3	140.13	0.554	8.25	0.034	0.10	0.046				
4	134.75	0.418	7.63	0.075	0.07	0.022		No improvement		
5	137.28	0.336	8.18	0.045	-0.18	0.009				
6	134.89	0.370	8.13	0.053	-0.24	0.008				
7	136.71	0.253	8.48	0.060	0.03	0.021				
8	131.88	0.597	7.87	0.063	0.10	0.023				
9	131.48	0.613	8.11	0.060	0.03	0.033				
10	134.69	0.305	8.55	0.012	0.16	0.031				
Center	135.70	0.332	8.04	0.050						

Table 2a.

RANDOM ERRORS IN TRAVEL TIME

Sta. no.	Azi-muth	First iteration $\alpha_1 = 1.0$, $\alpha_2 = 1.0$ Std. err.	dT/dΔ (sec/deg)	Std. err.	Resi-dual (sec)	Std. err. of tra-vel time	Second iteration $\alpha_1 = 0.99 \pm 2.756$; $\alpha_2 = 0.87 \pm 3.469$ dT/dΔ (sec/deg)	Std. err.	Resi-dual (sec)	Std. err. of tra-vel time
1	136.37	1.351	7.15	0.179	-0.12	0.307	7.13	0.176	-0.01	0.299
2	133.10	0.807	7.02	0.194	0.10	0.416	7.06	0.194	0.13	0.405
3	136.67	1.221	7.47	0.111	-0.68	0.282	7.42	0.107	-0.65	0.275
4	137.97	1.412	7.65	0.082	0.51	0.571	7.57	0.077	0.38	0.551
5	134.26	2.798	7.42	0.113	0.19	0.113	7.41	0.112	0.29	0.110
6	130.52	0.877	6.99	0.185	-0.22	0.440	7.09	0.186	-0.37	0.434
7	131.09	0.828	7.30	0.124	1.08	0.142	7.36	0.124	1.10	0.138
8	134.83	0.722	7.88	0.088	-0.04	0.159	7.83	0.086	-0.06	0.155
9	131.61	0.784	7.60	0.089	0.82	0.102	7.63	0.090	-0.69	0.099
10	129.39	1.100	7.36	0.109	0.66	0.225	7.45	0.110	0.60	0.220
11	132.09	0.774	7.91	0.108	-2.19	0.147	7.90	0.106	-2.05	0.144
12	127.71	1.448	7.42	0.100	-0.67	0.531	7.56	0.102	-0.86	0.523
13	134.71	0.634	8.26	0.153	1.07	0.389	8.17	0.148	0.87	0.376
14	129.80	1.083	7.89	0.118	1.48	0.304	7.92	0.118	1.67	0.295
15	132.73	0.688	8.38	0.191	-0.34	0.884	8.31	0.185	-0.35	0.568
Center	132.88	0.693	7.57	0.090			7.57	0.090		
		$\alpha_1 = 1.0$, $\alpha_2 = 1.0$					$\alpha_1 = 0.84 \pm 2.4864$; $\alpha_2 = 1.09 \pm 2.941$			
1	134.29	1.506	8.20	0.242	-0.42	0.227	8.07	0.227	-0.23	0.209
2	134.61	1.172	8.15	0.188	0.92	0.110	8.08	0.176	0.87	0.103
3	134.95	0.642	8.20	0.097	-0.12	0.402	8.18	0.091	-0.10	0.373
4	134.57	1.121	8.11	0.222	-0.13	0.192	8.03	0.207	-0.20	0.179
5	135.06	1.003	8.14	0.131	0.03	0.078	8.15	0.122	-0.17	0.073
6	135.12	1.003	8.08	0.157	0.82	0.068	8.12	0.147	0.70	0.063
7	135.38	1.092	8.11	0.175	-0.43	0.186	8.20	0.168	-0.47	0.173
8	134.85	0.789	8.04	0.195	-0.74	0.202	8.04	0.184	-0.79	0.186
9	135.14	1.675	8.03	0.179	0.22	0.285	8.11	0.170	0.34	0.267
10	135.49	1.815	8.08	0.213	-0.10	0.269	8.22	0.205	0.05	0.253
Center	134.98	0.957	8.11	0.148			8.11	0.138		

Table 2b.

	NO ERRORS IN TRAVEL TIME						RANDOM ERRORS IN TRAVEL TIME					
	First and final iteration						First and final iteration					
	$\alpha_1 = 1.0$, $\alpha_2 = 1.0$						$\alpha_1 = 1.0$, $\alpha_2 = 1.0$					
Sta. no.	Azimuth (deg)	Std. err.	dT/dΔ (sec/deg)	Std. err.	Residual (sec)	Std. err. of travel time	Azimuth (sec)	Std. err.	dT/dΔ (sec/deg)	Std. err.	Residual (sec)	Std. err. of travel time
1	136.80	0.152	7.30	0.020	-0.06	0.003	136.79	2.488	7.16	0.318	-0.04	0.768
2	132.55	0.135	7.25	0.023	0.06	0.002	132.55	2.224	7.13	0.366	+0.13	0.515
3	137.48	0.135	7.49	0.014	0.01	0.001	137.56	2.188	7.41	0.219	-0.64	0.345
4	139.36	0.177	7.60	0.015	0.01	0.003	139.45	2.880	7.54	0.242	0.26	0.861
5	134.32	0.077	7.48	0.011	0.03	0.001	134.47	1.280	7.42	0.184	0.40	0.318
6	129.32	0.160	7.27	0.027	-0.03	0.003	129.39	2.618	7.17	0.431	-0.46	0.712
7	130.20	0.111	7.45	0.017	0.08	0.001	130.42	1.805	7.40	0.277	1.16	0.268
8	135.36	0.095	7.77	0.010	0.03	0.002	035.67	1.541	7.79	0.162	0.0[illegible]	0.440
9	131.02	0.084	7.64	6.010	-0.09	0.001	131.38	1.365	7.64	0.160	-0.5[illegible]	0.355
10	128.09	0.144	7.52	0.019	0.04	0.001	128.43	2.348	7.49	0.314	+0.59	0.308
11	131.77	0.094	7.83	0.010	-0.05	0.003	132.25	1.510	7.88	0.161	-1.95	0.340
12	126.03	0.185	7.60	0.023	0.00	0.003	126.48	3.016	7.59	0.367	-0.96	0.896
13	135.40	0.139	8.02	0.019	0.00	0.003	135.86	2.234	8.11	0.299	0.81	0.733
14	128.80	0.144	7.85	0.014	0.08	0.004	129.41	2.306	7.9[illegible]	0.214	1.67	0.686
15	132.80	0.147	8.12	0.013	-0.01	0.002	133.44	2.362	8.25	0.336	-0.43	0.929
Center	132.63	0.063	7.62	0.011			132.91	1.043	7.58	0.139		
	$\alpha_1 = 1.0$, $\alpha_2 = 1.0$						$\alpha_1 = 1.0$, $\alpha_2 = 1.0$					
1	138.81	0.531	7.84	0.082	0.05	0.010	135.04	2.639	7.63	0.410	-0.34	0.245
2	137.18	0.456	7.92	0.067	-0.14	0.004	135.25	2.243	7.78	0.336	0.49	0.102
3	141.66	0.462	8.12	0.058	0.00	0.011	131.74	1.934	8.80	0.315	0.24	0.265
4	134.07	0.555	7.89	0.098	0.03	0.007	137.42	3.092	7.37	0.468	0.22	0.172
5	137.82	0.336	8.09	0.047	0.07	0.005	133.62	1.516	8.44	0.245	0.56	0.123
6	134.03	0.438	8.10	0.063	0.04	0.006	135.59	2.200	8.10	0.308	0.12	0.137
7	137.35	0.296	8.22	0.068	-0.03	0.006	133.05	1.248	8.84	0.346	0.12	0.143
8	130.62	0.653	8.00	0.110	-0.01	0.008	138.62	3.886	7.38	0.499	-0.26	0.187
9	130.26	0.642	8.13	0.095	0.01	0.009	137.60	3.531	7.79	0.439	0.06	0.222
10	134.71	0.367	8.26	0.078	-0.01	0.009	134.04	1.704	8.75	0.384	0.15	0.213
Center	135.65	0.395	8.04	0.056			135.10	1.932	8.08	0.276		

Table 3.

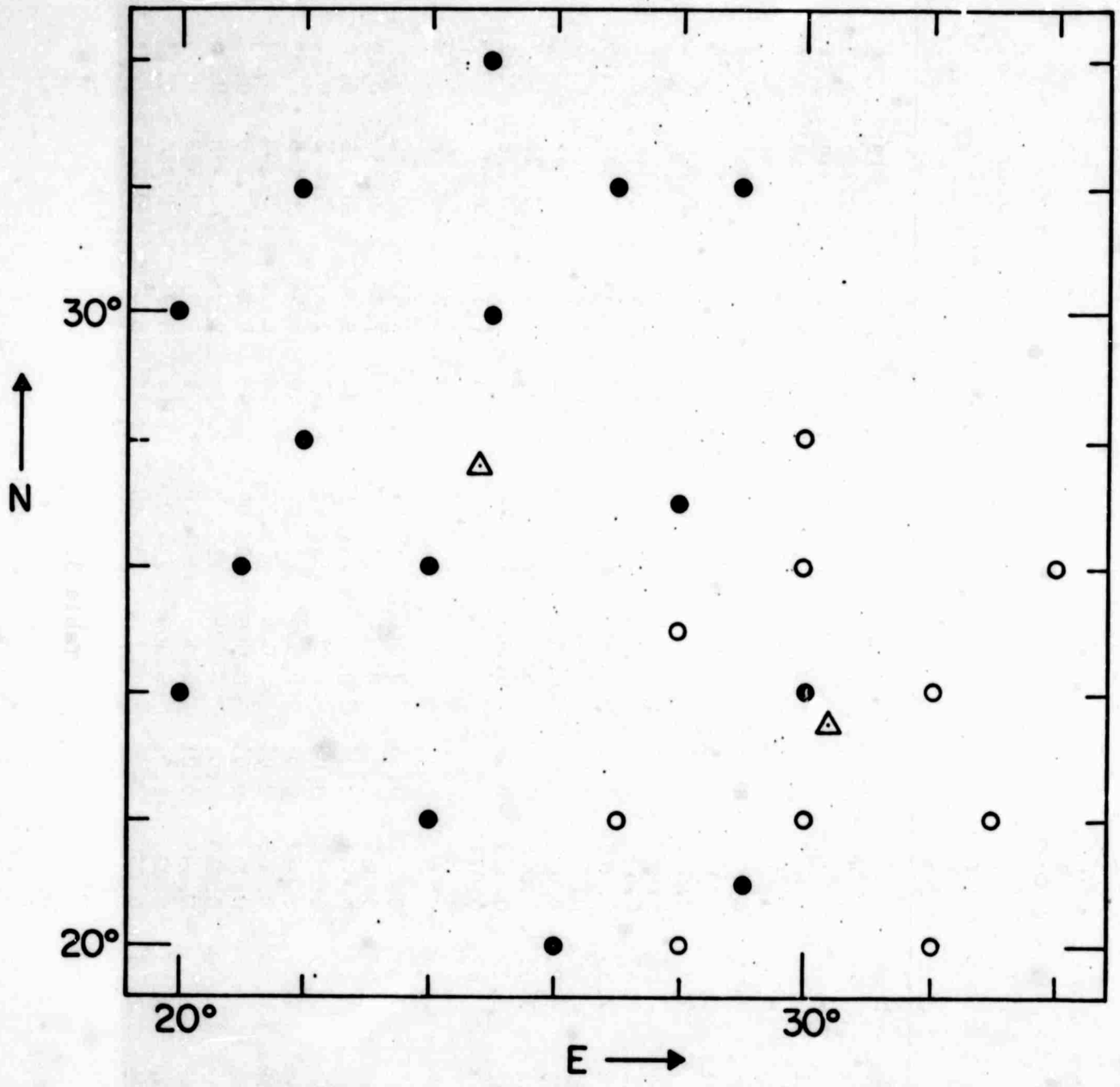

Fig. 1.

III. THEORETICAL SEISMOGRAMS AND EARTH STRUCTURE

III.1 Upper Mantle Seismic Models

(D.V. Helmberger)

In this study we will generate synthetic seismograms for upper mantle models of spherical, homogeneous layers. The seismic signals were generated by an underground shot at the NTS. We will synthesize the motion at the variour LRSM stations.

The procedure followed will be to develop the theory for a plane layered earth assuming a point source. Next, the theory of spherical layers will be treated and shown to reduce to a simple modification of plane layered theory when the curvature is small. Finally this theory is applied to models proposed from observations of the Bilby event. A short comparison between these observations and synthetic waveforms is given.

A. Point source in a plane-layered earth

Suppose we consider the problem setup specified in the following diagram.

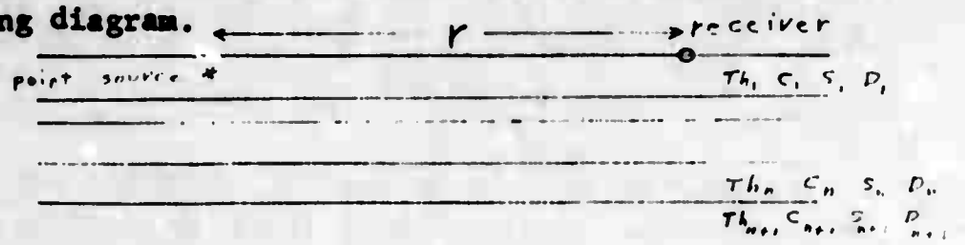

Let W be the vertical displacement with r the horizontal coordinate. The Laplace transform with respect to time is denoted by an overbar with s the transform variable. Suppose the point source emitts a step function of unit strength. Then the integral expression for the transformed response from the bottom of the n^{th} layer is

$$\bar{W}(r,s) = \frac{s}{\pi} \operatorname{Im} \int_0^\infty K_0(spr)\, \Phi(p)\, \mathcal{R}(p)\, \mathcal{T}(p)\, e^{-s\,q(p)}\, p\, dp \qquad (A1)$$

where

$$q(p) = \sum_j^n Th_j\, \eta_j \;, \qquad Th_1 = \tfrac{1}{2}(h+H)$$

$$\mathcal{T}(p) = T_{12} \cdot T_{23} \cdots T_{n-1,n} \cdot T_{n,n-1} \cdots T_{21}$$

$\mathcal{R}(p)$ = Reflection Coefficient at n,n+1

$$\Phi(p) = (\eta_2' - p^2) \,/\, \left(s_1^2 \left(4 s_1^4 \eta_1 \eta_1' + (1 - 2p^2 s_1^2)^2 \right) \right)$$

$$\eta_j = \left(\frac{1}{c_j^2} - p^2 \right)^{1/2} \;, \quad \eta_j' = \left(\frac{1}{s_j^2} - p^2 \right)^{1/2}$$

The above formula yields the transformed displacement for the generalized ray that has traversed the strata exclusively in the P-mode and contains no internal reflections. The generalized ray that is reflected at the surface above the source will be included in the source function and will be discussed later. T(p) and R(p) are the transmission and reflection coefficients and are given by Helmberger (1968).

The formalism applied in this section is obtained directly from that paper. Equation (A1) should be compared with (1). The extra s and D(p) are introduced by the fact that the receiver is situated at the surface and because we are interested in displacement, see Knopoff, Gilbert, and Pilant (1960) for details.

Applying the inverse Laplace transform we obtain

$$w(r,t) = \frac{2}{\pi}\frac{d}{dt}\,\mathrm{Im}\int^{t} p\left(\frac{dp}{d\tau}\right)\frac{R(p)\,D(p)\,H(t-\tau)\,d\tau}{(t-\tau)^{\frac{1}{2}}\left(t-\tau+2pr\right)^{\frac{1}{2}}}$$

where

$$\tau(p) = pr + 2\sum \tau h_j \eta_j$$

$$dp/d\tau = \left(r - 2p\sum \tau h_j/\eta_j\right)^{-1}.$$

The j's are to be summed from 1 to n. Suppose we now apply the high frequency approximation which is valid for sources of short duration

$$t - \tau + 2pr \approx 2pr$$

Then (A2) reduces to

$$w(r,t) = \frac{2}{\pi}\frac{d}{dt}\left[\frac{1}{\sqrt{t}} * \psi(t)\right]$$

where

$$\psi(t) = \mathrm{Im}\left(R(p)\,\bar{v}(p)\,D(p)\sqrt{p}\left(\frac{dp}{d\tau}\right)\frac{1}{\sqrt{2r}}\right)$$

To compute the vertical displacement we must sum over all the generalized rays which arrive in some specified time or

$$W_T(r,t) = \sum W_n(r,t)$$

where

$$W_n(r,t) = \frac{2}{\pi}\frac{d}{dt}\left(\frac{1}{\sqrt{t}} * \psi_n(t)\right)$$

and

$$\psi_n(t) = \mathrm{Im}\left[f_n(p)\,D(p)\sqrt{p}\left(\frac{dp}{d\tau}\right)_n\frac{1}{\sqrt{2r}}\right]$$

where the generalized rays are numbered 1 to n see Helmberger (1968) for details. Now one can perform the summation first yielding

$$W_T(r,t) = \frac{2}{\pi}\frac{\partial}{\partial t}\left[\frac{1}{\sqrt{t}} * \sum \psi_n(t)\right] \qquad (A4)$$

The high-frequency approximate solution has been compared with the exact solution and found very satisfactory for body wave analysis when the source duration is short compared with the travel time between the source and receiver. This approximation allows one to replace n convolutions by one. Before generating synthetic seismograms we must consider the effect of curvature which we now take up.

B. Point source in a spherically layered earth

We first consider the problem solved by Gilbert (1960) on scattering of impulsive SH-waves from a rigid sphere. The problem setup is given below.

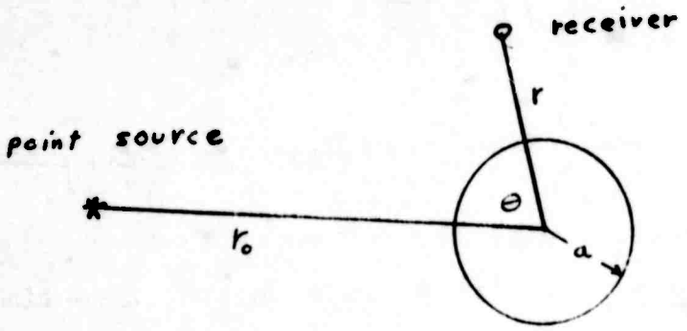

The displacement u has only a ϕ component in spherical coordinates (r, θ, ϕ). Suppose we assume a delta function time dependent source, then

$$\nabla^2 u - \frac{1}{\beta^2}\frac{\partial^2 u}{\partial t^2} = \frac{-\delta(r-r_0)\,\delta(\theta-\theta')}{r^2 \sin\theta} \qquad (B1)$$

where β is the velocity. If we apply the Laplace transform on the time variable and the Legendre transform on the angle variable θ we obtain

$$\frac{1}{r^2}\frac{\partial}{\partial r}\left[r^2\frac{\partial U}{\partial r}\right] - \left(\left(\frac{s}{\beta}\right)^2 + \frac{1}{r^2}\nu(\nu+1)\right)U = -\frac{1}{r^2}\delta(r-r_0) \quad (B2)$$

where

$$U(\nu) = \int_0^{\pi} \bar{u}(\cos\theta)\, P_\nu(\cos\theta)\sin\theta\, d\theta$$

and

$$\bar{u}(\cos\theta) = \frac{1}{2i}\int_L \frac{\lambda\, d\lambda}{\cos\pi\lambda}\, U(\lambda-\tfrac{1}{2})\, P_{\lambda-\frac{1}{2}}(-\cos\theta) \quad (B3)$$

where the L contour runs above the real λ axis from $-\infty$ to ∞. A particular solution of (B2) is

$$U_0 = \left(\frac{k}{2\pi^2}\right) i_\nu(kr)\, k_\nu(kr_0) \qquad r < r_0,\ k = s/\beta$$

where i_ν and k_ν are the spherical bessel functions. Since the sphere is rigid $U=0$ at $r=a$ and the total solution becomes

$$U = U_0 - \left(\frac{k}{2\pi^2}\right) \frac{i_\nu(ka)\, k_\nu(kr_0)}{k_\nu(ka)}\, k_\nu(kr)$$

We will be primarily interested in the second term which represents the reflected motion. The solution in the above form is due to Gilbert (1960). He applies the saddle point approximation to obtain the first-motion solution. However, we can obtain the high frequency approximation by the application of Cagniard's method.

Let

$$P_{\lambda-\frac{1}{2}}(\cos\theta) = i\, e^{i\pi\lambda} P_{\lambda-\frac{1}{2}}(\cos\theta) - 2i\cos\pi\lambda\, Q'_{\lambda-\frac{1}{2}}(\cos\theta)$$

and $\bar{u} = \bar{u}_1 + \bar{u}_2$, where

$$\bar{u}_1 = \frac{1}{2}\int_L e^{i\pi\lambda} P_{\lambda-\frac{1}{2}}(\cos\theta)\frac{1}{\cos\pi\lambda}\, U(\lambda-\tfrac{1}{2})\, d\lambda$$

and $$\bar{u}_2 = -\int_L \lambda d\lambda \, Q'_{\lambda-\frac{1}{2}}(\cos\theta)\, U(\lambda-\tfrac{1}{2}) \qquad (B4)$$

We will consider $\bar{u}_2$ which yields the reflected motion.

$$Q'_{\lambda-\frac{1}{2}} = \frac{e^{-i(\lambda\theta-\pi/4)}}{(2\pi\lambda\sin\theta)^{\frac{1}{2}}} \qquad \lambda\to\infty$$

and let

$$\lambda = i\mu \quad \& \quad Q' = \frac{1}{i}\, e^{-\mu\theta}/(2\pi\mu\sin\theta)^{\frac{1}{2}}$$

Equation (B4) becomes

$$\bar{u}_2(\cos\theta) = \frac{1}{i}\int_L \frac{\mu\, d\mu\, e^{-\mu\theta}}{(2\pi\mu\sin\theta)^{1/2}}\, U(-i\mu-\tfrac{1}{2})$$

where

$$U(-i\mu-\tfrac{1}{2}) \approx \frac{-1}{4\pi r}\,(k^2r^2-\mu^2)^{-\frac{1}{2}}\exp\left(-2\psi(\mu,s)\right)$$

where

$$r = r_0 \quad \& \quad \psi \equiv \int_a^r (k^2-\mu^2/r^2)^{1/2}\, dr$$

The asymptotic forms of the bessel functions were used in evaluating U. We also used the following identity

$$(k^2r^2-\mu^2)^{\frac{1}{2}} + \mu\sin^{-1}\left(\frac{\mu}{kr}\right) = \int\left(k^2-\frac{\mu^2}{r^2}\right)^{\frac{1}{2}} dr$$

Substituting we obtain

$$\bar{u} = \frac{-1}{2\pi}\int_0^{i\infty} \frac{\mu\, d\mu}{r(2\pi\mu\sin\theta)^{1/2}}\,(k^2r^2-\mu^2)^{-\frac{1}{2}}\, e^{-\mu(\theta-2\psi)}$$

Now let $\mu = sp$ and change variable, (B5) becomes

$$\bar{u} = \frac{-1}{2\pi}\,\frac{s}{\sqrt{s}}\,\mathrm{Im}\int_0^{i\infty} \frac{\sqrt{p}\, dp\, e^{-s(p\theta+2\psi(p))}}{r^{\frac{1}{2}}(2\pi\sin\theta)^{\frac{1}{2}}\left(\frac{1}{\beta^2}-\frac{p^2}{r^2}\right)^{\frac{1}{2}}} \qquad (B6)$$

where

$$\psi(p) = \int\left(\frac{1}{\beta^2}-\frac{p^2}{r^2}\right)^{\frac{1}{2}} dr$$

and we are now assuming a step function source. Let $p' = p/r$ and (B6) becomes

$$\bar{u} = \frac{-s}{2\pi\sqrt{s}}\,\mathrm{Im}\int_0^{i\infty} \frac{\sqrt{p'}\, dp'}{(2\pi r\sin\theta)^{1/2}}\,\frac{e^{-sr}}{\left(\frac{1}{\beta^2}-p'^2\right)^{\frac{1}{2}}}$$

where

$$\tau = p'x + 2\int_{a/r}^{1}\left(\frac{1}{\beta^2} - \frac{p'^2}{r'^2}\right)^{\frac{1}{2}} dr'$$

and r' is normalized and $x = or$, x = surface range

Now applying the Laplace inversion we note that

$$\frac{s}{\sqrt{s}} \Rightarrow \frac{\partial}{\partial t}\left[\frac{1}{\sqrt{\pi t}}\right]$$

and

$$u(r,\theta) = \frac{-1}{2\pi^2}\frac{\partial}{\partial t}\left[\frac{1}{\sqrt{t}} * \Psi(t)\right]$$

where

$$\Psi(t) = \mathrm{Im}\left[\frac{\sqrt{p}}{\sqrt{2x}}\left(\frac{\partial p}{\partial \tau}\right)\left(\frac{1}{\beta^2} - p^2\right)^{-\frac{1}{2}}\right]$$

because $x \approx r\sin\theta$. The form of (B7) is identical to (A3) although ($\partial p / \partial \tau$) is different.

This solution can be generalized to n-layers when we neglect terms involving (as)$^{-1}$

$$u = \frac{2}{\pi}\frac{\partial}{\partial t}\left[\frac{1}{\sqrt{t}} * \psi(t)\right]$$

where

$$\psi(t) = \mathrm{Im}\left[R\left(\frac{p}{r_j}\right)\bar{J}\left(\frac{p}{r_j}\right)D(p)\sqrt{p}\left(\frac{\partial p}{\partial \tau}\right)\frac{1}{(2x)^{\frac{1}{2}}}\right]$$

and

$$\tau = px + 2\tau h_j \eta_j$$

where

$$\eta_j = \left(\frac{1}{c_j^2} - \frac{p^2}{a^2}\right)^{\frac{1}{2}}$$

a_j = average normalized radius of layer j and p is replaced by ($1/r$) in all other functions of the plane-layer case functions where r is the normalized local radius. That is at interface r_c the transmission coefficient is the

same as that in the plane case except p is replaced by p/r. The solution is only rigorous for reflected responses although it is probably good for refractions as well when the curvature is small.

C. Synthetic seismograms based on the NTS Bilby event

Synthetic seismograms are produced by a double convolution

$$SS(t) = \frac{\partial}{\partial t}\left[W(t) * T(t) \right]$$

where

$$T(t) = \frac{\partial}{\partial t}\left[S(t) * I(t) \right]$$

and $I(t)$ is the instrumentation response and $S(t)$ is the idealized source function. We chose to include the interaction of the earth's surface with the direct wave and label the total radiation $S(t)$. At ranges greater than 30 degrees the observations are quite similar in character which reflects the nature of $T(t)$. This is expected because the model structure is apparently simple at depths greater than 900 km and $W(t)$ is approximately a step function so that $SS(t) \approx T(t)$ The point will become clearer when we compute a simple model (S.E. Profile). We have done some calculations on $T(t)$ directly from $I(t)$ and $S(t)$ allowing a layer above the source. Using the $I(t)$ discussed by Carpenter (1967) and source function for the Bilby event by Toksöz (1967), we calculated T displayed in Fig. 1 where we assumed a thin layer of low velocity material above the shot. The theoretical response is the motion appropriate for energy emerging at about 30 degrees. The

decaying oscillation effect is caused by energy leaking out of the layer. The lower plot is $T'(t)$ which contains a convolution of the upper plot. $T'(t)$ does not change with angle very rapidly so that $T(t)$ is appropriate for a 10 degree range as well. Fig. 2 displays a profile of observations running S.E. from the NTS taken from the Bilby event. Their locations are given in Fig. 3. Note that the first 3 peaks of the OR observation look similar to Fig. 1. However, we do not know $S(t)$ very accurately so that we will use the first three secs of the observation at OR as the transfer function $T(t)$ in this preliminary study. We will discuss the N.E. profile first and return to the S.E. later.

The N.E. Profile has been studied by Julian and Anderson (1968). They find a model which is quite similar to Johnson's (1967). A simplified model which contains the most prominent features is given in Fig. 4. Synthetic seismograms for this model are displayed in Fig. 5 and should be compared with the observations in Fig. 6. It should be noted that not all of the observations are from Bilby and difference in transfer functions are expected. Nevertheless the prominent second arrival occuring at about 12 degrees is quite impressive. This arrival is the critical reflection off the 400 km transition. At greater ranges this arrival becomes the first event followed closely and interfering with the response from the 650 km transition. This composite waveform is also indicated in the observations. At the smaller ranges the model produces a rather large arrival which is the sum of reflections off the bottom of the low velocity zone. The observations at this range (not shown in Fig. 6) do not show this event. This means the model needs a smoother transition at this depth.

We used the model proposed by Dowling and Nuttli (1964) for the S.E. profile. Their model is given in Figure 7. We used the Birch model for the shear velocities and densities. The velocity depth function was approximated by a stack of layers 20 km thick. Only the P-mode generalized rays were allowed. The rays containing only one reflection dominate the motion although internal reflections were considered near critical angles. That is we include internal reflections from five layers above and below that depth where the geometrical ray bottoms. A profile of synthetic waveforms are compared with corresponding observations in Fig. 8. The $SS(t)$ display the fact that linear gradients return the incident waveform with very little distortion of shape, as is well known. The rate of decay as a function of range is also quite smooth although there is a change of slope in the velocity depth function at about 500 km. The transfer function is quite apparent in the observations. However, the amplitudes disagree, also the 2274 km observation has a definite precursor. This indicates that the 650 km transition is also present in this profile. The critical reflection occurs at about this range which would explain the large amplitude. None of the S.E. recordings show prominent second arrivals so that the 400 km transition must not be as sharp as in the N.E. profile. Thus it appears that the upper mantle is quite inhomogeneous.

We are now in the process of gathering observations from many shots in an attempt to give a detailed treatment of these transitions.

REFERENCES

Carpenter, E.W., Teleseismic signals calculated for underground, underwater, and atmospheric explosions, Geophysics, 32, 17-32, 1967.

Dowling, J. and D. Nuttli, Travel-time curves for a low-velocity channel in the upper mantle. Bull. Seism. Soc. Amer., 54, 1981-1996, 1964.

Gilbert, The scattering of impulsive p wave-motion from a rigid sphere, (unpublished).

Helmberger, D., The crust-mantle transition in the Bering Sea, Bull. Seism. Soc. Amer., 58, 179-214, 1968.

Johnson, L., Measurements of mantle velocities of p-waves with a large array, Ph.D. Thesis, CIT, 1966.

Julian, B.R. and D.L. Anderson, Travel times, apparent velocities and amplitudes of body waves. Bull. Seism. Soc. Amer., 58, 339-366, 1968.

Knopoff L., F. Gilbert, and W. Vilant, Wave propagation in a simple layer, J. Geophys. Res., 65, 265-278, 1960.

Figure 1 Upper plot is the response of a point source interacting with a surface layer assuming a step function source. The lower is the resulting $T(t)$

Figure 2 Profile of observations from Bilby

Figure 3 Location of Bilby stations (after Dowling and Nuttli)

Figure 4 Model of the upper mantle

Figure 5 Synthetic seismograms based on the model in Fig. 4

Figure 6 Record section for NTS-NE profile (after Julian and Anderson)

Figure 7 Velocity model for data SE from Bilby (after Dowling and Nuttli)

Figure 8 Comparison of synthetic and observations

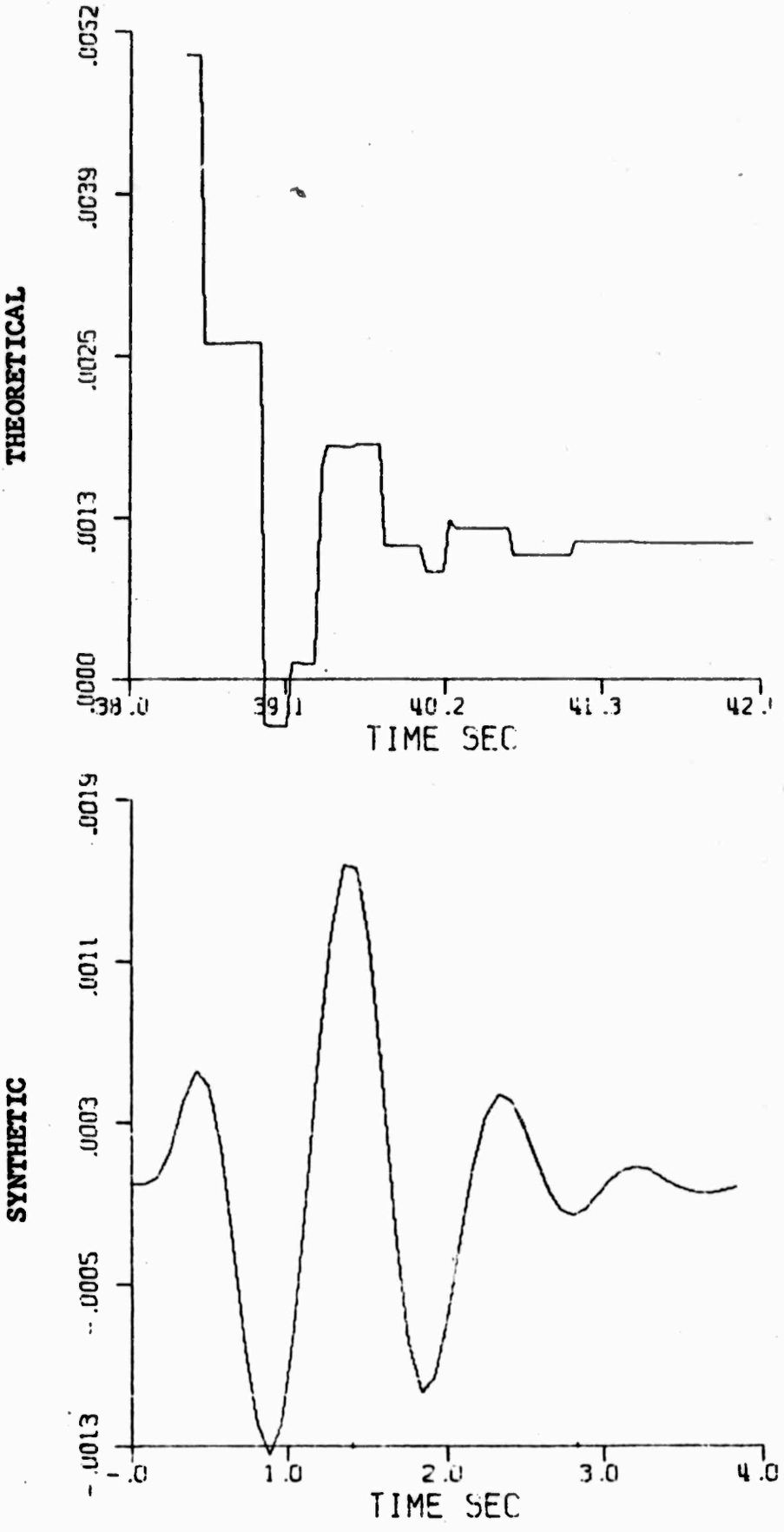
THEORETICAL
.0052
.0039
.0026
.0013
.0000
38.0
39.1
40.2
41.3
42.
TIME SEC
SYNTHETIC
.0019
.0011
.0003
-.0005
-.0013
-.0
1.0
2.0
3.0
4.0
TIME SEC

Fig. 1

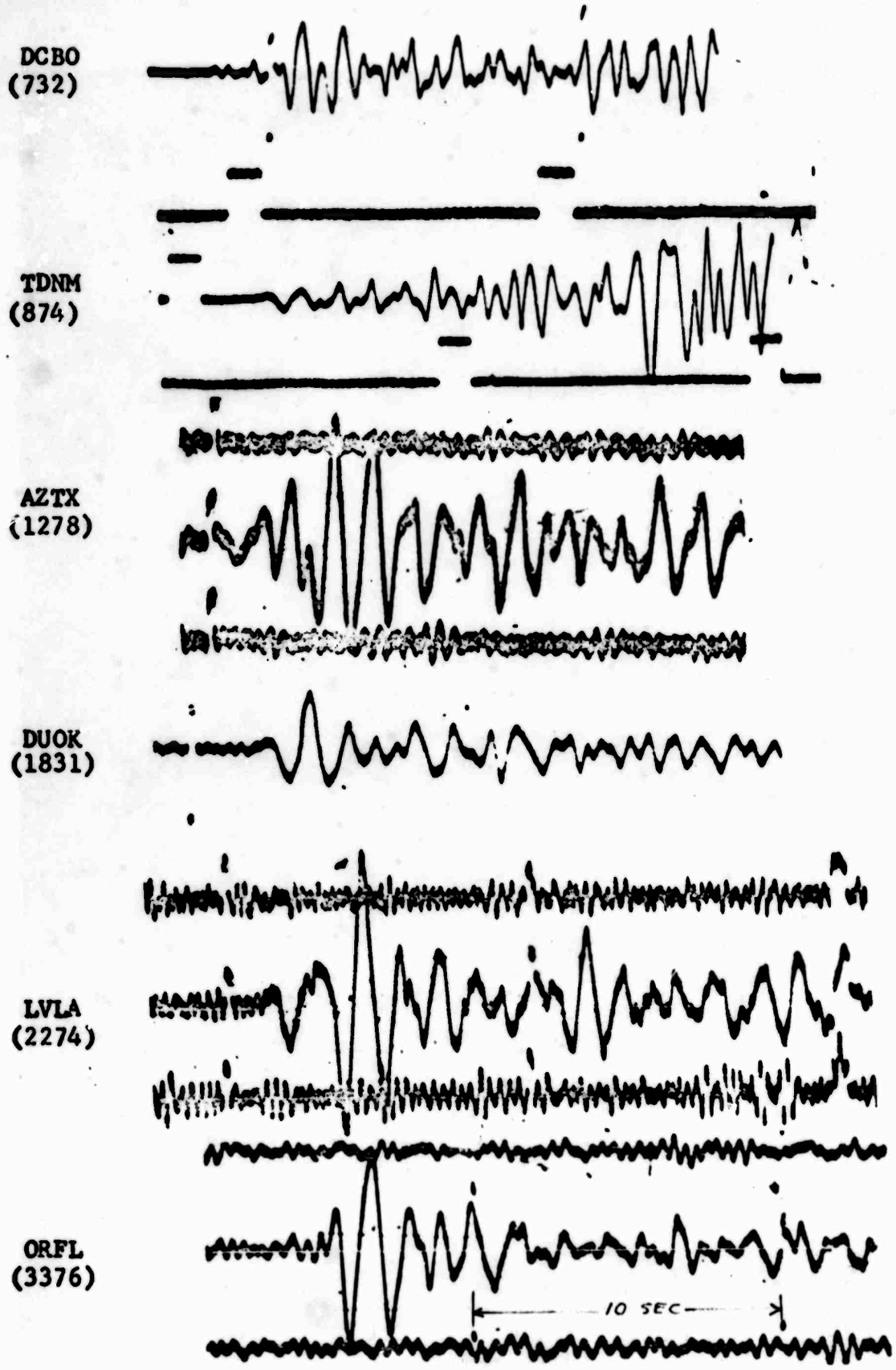
DCBO
(732)
TDNM
(874)
AZTX
(1278)
DUOK
(1831)
LVLA
(2274)
ORFL
(3376)
10 SEC

Fig. 2

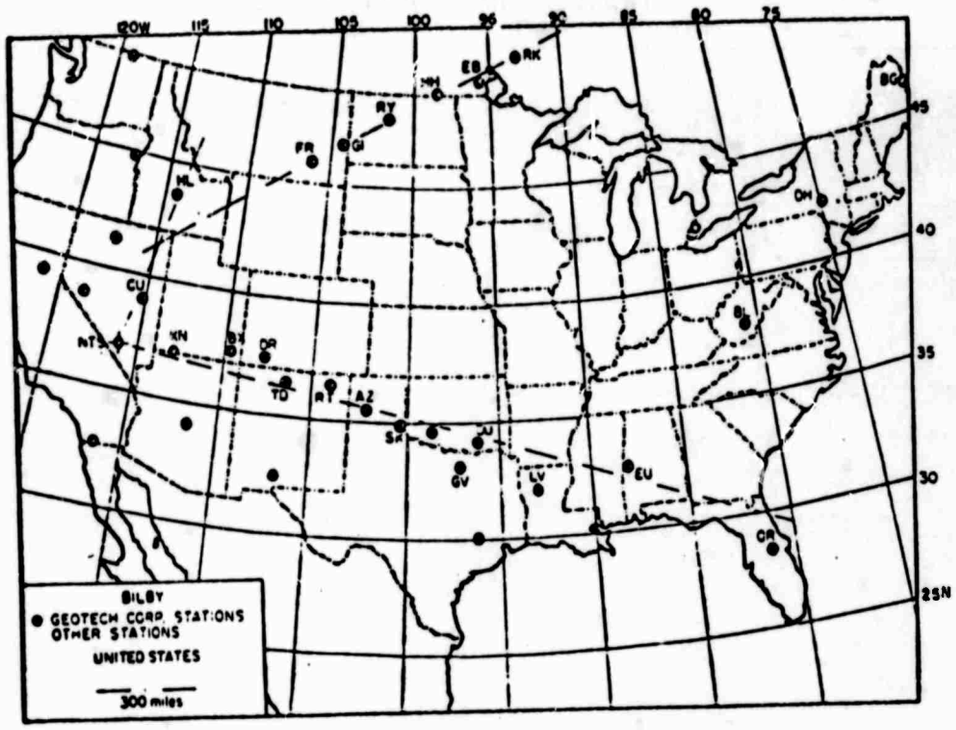
120W
115
110
105
100
95
90
85
80
75
45
40
35
30
25N
EB
RK
RY
GI
FR
HL
CU
KN
DR
TO
AZ
SH
GV
LV
EU
OH
BL
CR
BILBY
GEOTECH CORP. STATIONS
OTHER STATIONS
UNITED STATES
300 miles

Fig. 3

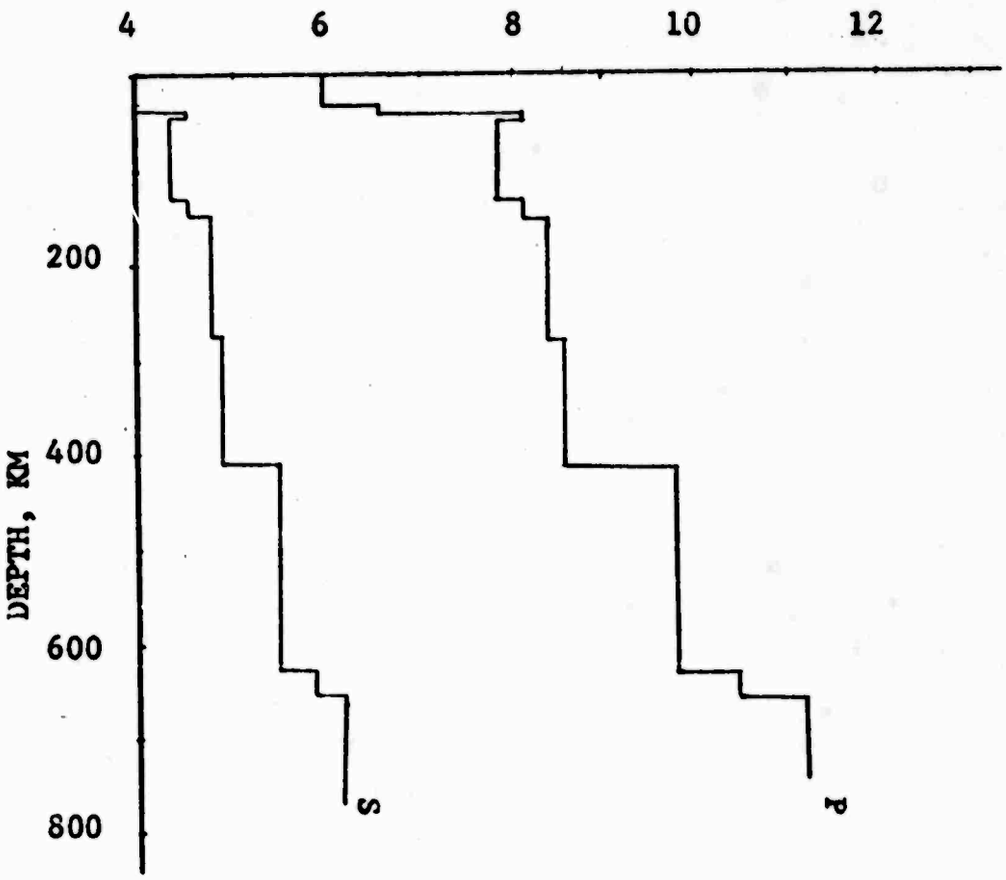
4
6
8
10
12
200
400
600
800
DEPTH, KM
S
P

Fig. 4

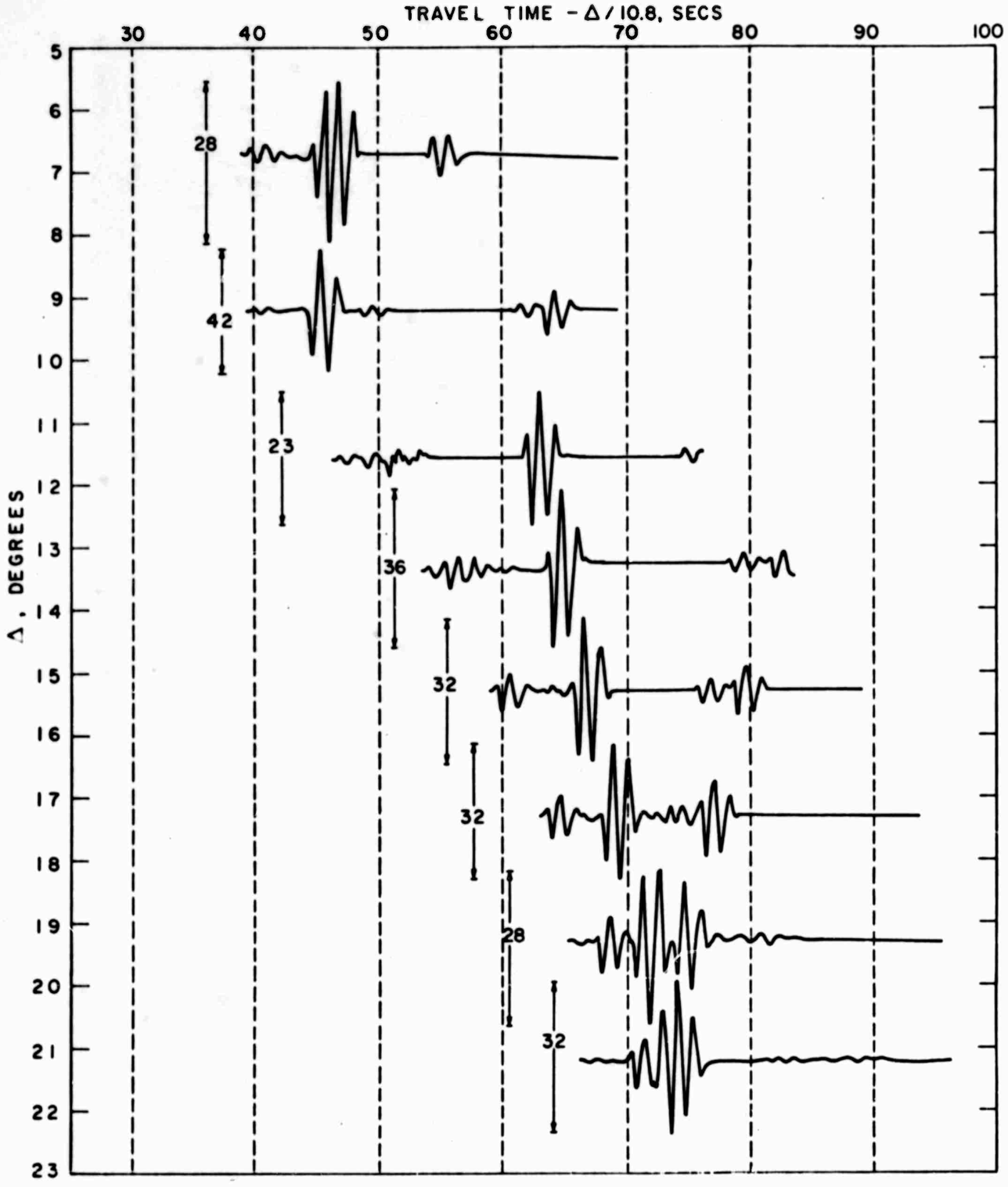
TRAVEL TIME - Δ / 10.8, SECS
30
40
50
60
70
80
90
100
Δ, DEGREES
5
6
7
8
9
10
11
12
13
14
15
16
17
18
19
20
21
22
23
28
42
23
36
32
32
28
32

Fig. 5

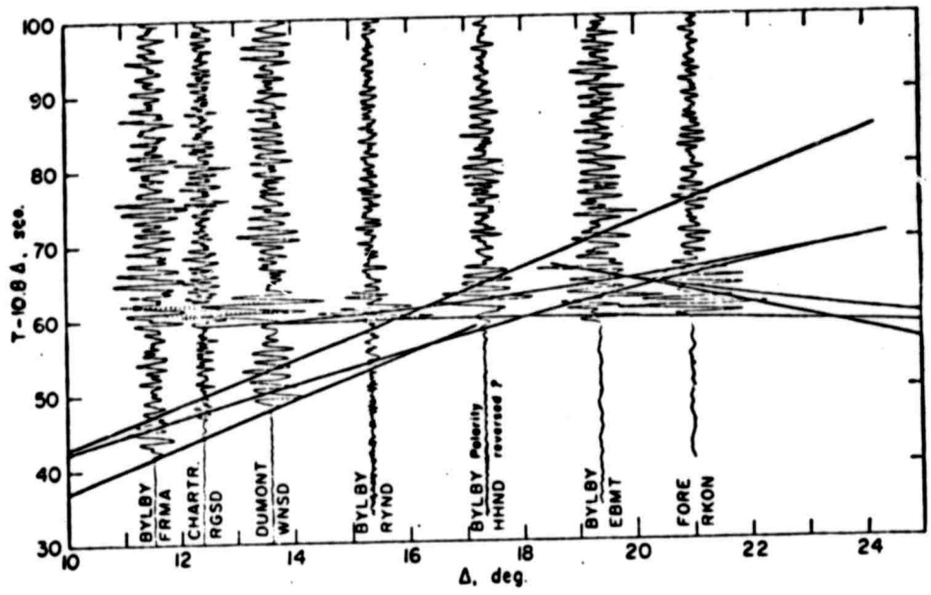

Fig. 6

TRAVEL-TIME CURVES FOR A LOW-VELOCITY CHANNEL

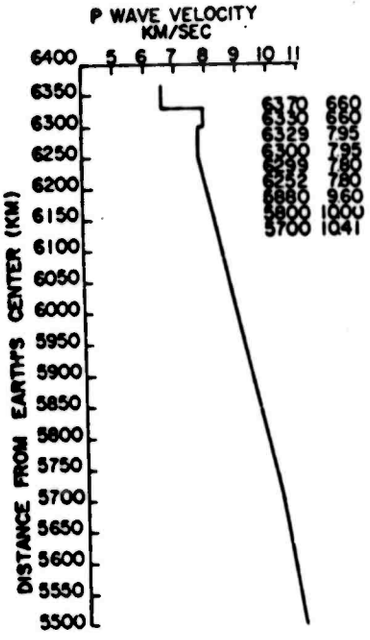

Fig. 7

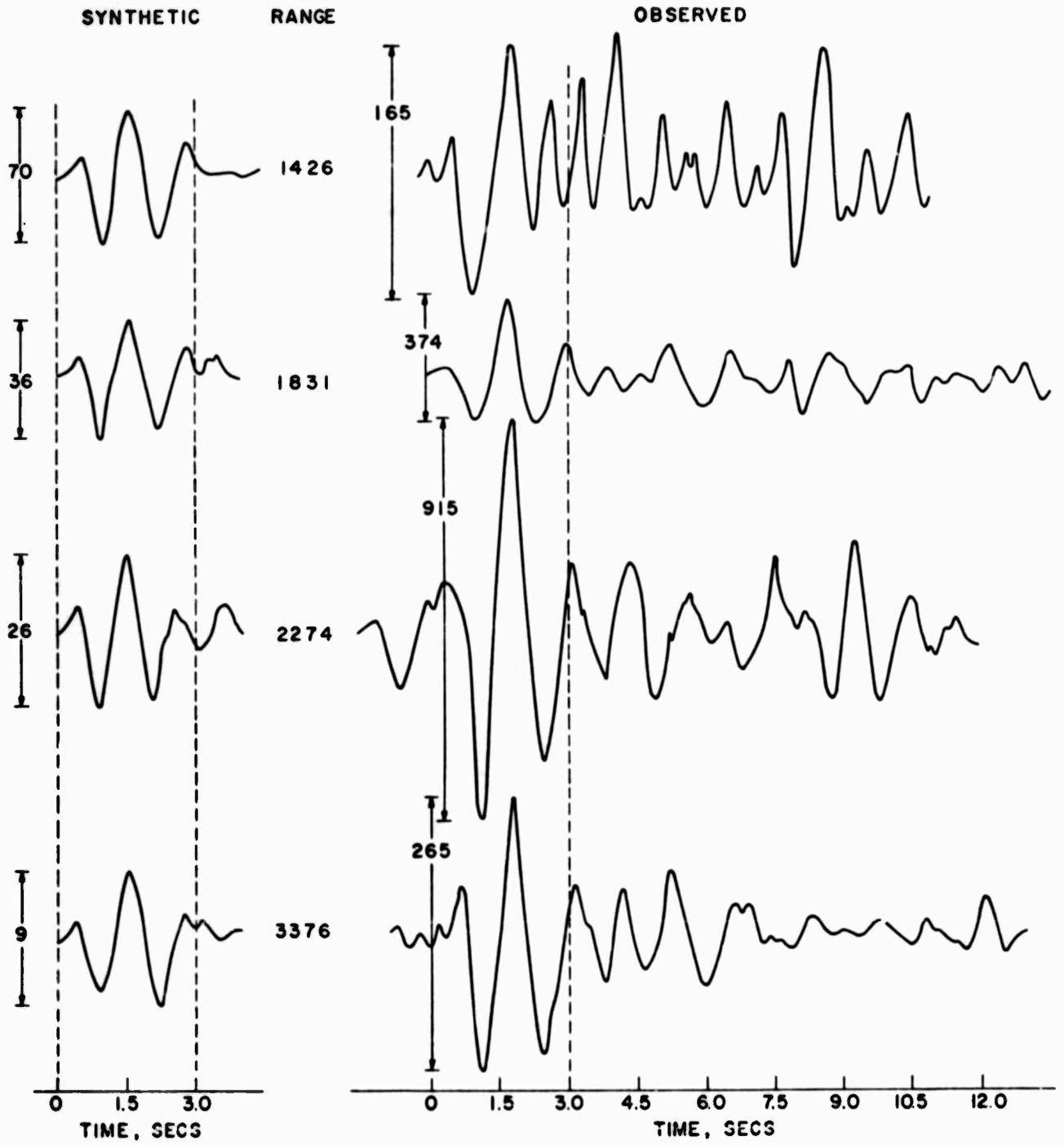
SYNTHETIC
RANGE
OBSERVED
70
1426
165
36
1831
374
915
26
2274
265
9
3376
0
1.5
3.0
TIME, SECS
0
1.5
3.0
4.5
6.0
7.5
9.0
10.5
12.0
TIME, SECS

Fig. 8

III.2 A Travel Time and Amplitude Interpretation of a Marine Refraction Profile

(D.V. Helmberger and G.B. Morris*)

III.2-1: Primary Waves

In recent years with the advent of modern computers it has become possible to gain meaningful information from seismic amplitudes. Some of the difficulties in this work have been obtaining adequate descriptions of source functions and maintaining a favorable signal-to-noise ratio at the receiver. It appears oceanic investigations have an advantage in the first of these whereas continental work has the advantage in the latter. However, last year at the proposed Mohole site off Hawaii, both features were well satisfied. Observations were recorded by FLIP, the Scripps Institution of Oceanography's Floating Instrument Platform, which provided an extremely stable platform with a low noise level. Seismic signals were produced by 85 kg charges fired at roughly constant depths along a 120 km line. The observed set of recordings provided an excellent opportunity to study the amplitude of seismic head waves.

The general method of study consisted of first obtaining a simple layered model which fit the travel times of the observed records. Theoretical synthetic records were computed for this model, after which waveforms and amplitude decay rates of the synthetic and observed records were compared. Where there was marked disagreement, adjustments were made to the original layered model by trial and error. This adjusting was continued until the synthetic records displayed the same pertinent features as the observed records. Such a technique is subjective and does not necessarily yield a unique solution. Nevertheless,

*University of California, San Diego
Marine Physical Laboratory of the Scripps Institution of Oceanography, La Jolla, California

by fitting both amplitude and travel time the solution is more restricted than a simple travel time interpretation.

OBSERVED RECORDS

The refraction records used in this study were taken during the summer of 1966 north of the Hawaiian Islands. The particular set of records, station SH31, located 350 km north-northwest of the island of Hawaii, is only one of the many profiles taken by a joint operation of Scripps Institution of Oceanography, University of Hawaii, Oregon State University, and the University of Wisconsin. Aboard FLIP the outputs of three hydrophones were recorded with the usual instrumental set-up used by Scripps and described by Raitt (1956) and Shor (1963). A sample recording is given in Figure 1. The first arrival G_1 is identified as a primary wave. The second arrival G_2 arrives with a velocity of 3.5 km/sec and is tentatively identified as a converted shear wave; that is a wave that travels through the ocean as a primary wave and through the solid crust as a shear wave. Figure 2 shows all the data points together with a layered model which is based on the time information. All of the shots regardless of charge size were used for this initial interpretation, however, only the 85 kg shots were used in the later comparisons. We should mention that the layered model was not based solely on the information from this one profile. This profile was one of a set which enabled us to compute split and reversed solutions. The layered model shown in Figure 2 is a solution which is compatible with this additional time information.

AMPLITUDE MEASUREMENTS OF OBSERVED RECORDS

To compare the amplitude-distance decay rates of the synthetic and observed records, we had to arrive at some measure of the amplitude of the received events. These

amplitudes were measured only on the records of the 85 kg charges. The records for smaller charges were not used in order to avoid empirical corrections for charge size and depth of detonation. The pulse amplitude was chosen as the average of the heights from the first valley to the second peak and from the second valley to the third peak for the three hydrophones. The first pressure peak was ignored as it was usually too small to measure accurately. These averaged values after being adjusted for amplifier gain setting are plotted for two seismic lines in Figures 3 and 4. Figure 3 is for profile SH31, whereas Figure 4 is for SH11, a profile some 450 km northwest of SH31. Figure 4 is included to support the premise that other lines in the area exhibit the same general amplitude-distance decay relation as SH31.

In making the amplitude measurements we observed that the principle cause of scatter seems to be interference between the various waves. Most of the events whose amplitude appears anomalously strong or weak on the plots also have a "disturbed" waveform suggesting that they are the result of more than one principle reflected or refracted event. This observation is also supported by noticing on the amplitude plots that the strong or weak second arrivals do not coincide with the strong or weak first arrivals, which would be the case if an entire record was anomalously strong or weak.

Regardless of the scatter of points, the amplitude-distance curves display several prominent features. Out to distances of about 30 km, which is the crust-mantle crossover, the amplitude decays slowly with distance. Beyond this cross-over point and out to about 50 km the amplitude shows little or no significant decay with distance. An additional feature not shown on the amplitude-distance

plots is exemplified in Figure 1. This record, taken at 18.8 km from the source, shows refracted and reflected events coming from the upper layers. The pertinent feature is how the energy is distributed with time. The energy in the first arrival G_1 occurs in the first three cycles after which there is a low signal level followed by a prominent second arrival G_2. It is this distribution of energy associated with the upper layers, together with the amplitude-distance relation which we will attempt to explain with the theoretically computed synthetic records.

SYNTHETIC WAVEFORMS AND COMPARISONS

The procedure for computing the synthetic records is similar to that developed by Helmberger (1968). In that paper the synthetic response was obtained by convolving the unit step function response of the earth model with the derivative of the transfer function with respect to time. The model response was calculated for a point source and receiver in the oceanic liquid layer overlying a crustal model of plane, homogeneous, isotropic solid layers and a solid half space. The method of generalized reflection and transmission coefficients was used to calculate the transient response in integral form. Such integrals can be solved by the Cagniard (1939) method. A version modified by deHoop (1960) and, later, extended to point sources by Gilbert (1963) was used. The transfer function or a modified source function which includes the effects of bubble pulses and various reflections from the surface was defined as:

$$T(t) = W(t) - W(t - t_1) - W(t - t_1 - t_2)$$

where W(t) is the convolution of the source function and

the instrumentation response. t_1 and t_2 are time lags determined by the depth of source and receiver respectively. The method of analysis used here is the same except for the addition of an absorption factor.

In order to avoid complications caused by variation of charge, all charges used in this study were 85 kg fired at depths of about 100 m. The resulting transfer function is shown by the dashed curve in Figure 5. Since the observations do not show the high frequency ripple apparent in Figure 5, we eliminated the ripple by applying a minimal amount of absorption. The effect of absorption can be treated by applying the operator $F(t, T/Q_{av})$ defined by Carpenter (1967). Here t is time, T is the total solid earth travel time of the compressional wave from source to receiver, and $1/Q_{av}$ is the average specific dissipation factor. The propagation operator used is given in Figure 6, with T = 15 sec and Q_{av} = 500. Convolving this operator with the transfer function produces the solid curve in Figure 5. This filtered transfer function was used throughout the study.

Using the propagation operator in this way is equivalent to simply low pass filtering our synthetic records. We are aware that while it is operationally convenient to define T/Q_{av} as a constant, it is an unrealistic treatment of absorption as it assumes the energy loss from absorption does not change with distance. The result is that the arrivals at short ranges are over-attenuated, while those at large ranges are under-attenuated. Nevertheless, by applying only a small amount of absorption the resulting amplitude change is not severe and does not change the basic behavior of the amplitude-distance decay curves.

Starting from the travel time model a perturbed model was found, by trial and error, which shows definite similarities in wave form to the observed records; however,

the refraction travel times now disagree slightly. This model, F, is given in Figure 7. The densities and shear velocities are assumed except for the apparent velocities of 3.55 km/sec and 3.85 km/sec which were obtained from the travel time data. Before discussing the synthetic waveforms for this model it is educational to look at the pressure response of the model as a function of range, R, assuming a unit step function pressure source (see Figures 8 and 9). The pressure responses are the summation of the P-mode generalized rays including multiple reflections within the various layers. Contributions of the large number of generalized rays that travel across one layer or more in the S-mode are neglected, although such contributions are appreciable at short ranges. This subject will be discussed in Part II. At R = 14.1 km the pressure response is dominated by three events which arrive at approximately the same time. They are responses from the bottom of layers 3, 4, and 5. These three events are quite strong since all three are near their respective critical angles, hence the large amplitude. As the range increases the response from the 6.8/8.1 interface, P_6, grows rapidly. It becomes the dominant event for R > 25 km. For larger ranges the refraction and reflection for this interface separate in time. As separation occurs the response from the bottom interface, P_7, grows supporting the refracted or head wave. The peak following P_6 is the first internal reflection in the oceanic layer.

The synthetic waveforms produced by convolving the responses in Figures 8 and 9 with the filtered transfer function in Figure 5 are given in Figures 10 and 11. The observations are included for comparison. At the nearest ranges the pressure response is essentially a step function so that when we perform the convolution and take the

derivative we reproduce the filtered transfer function. Note the similarity between Figure 5 and the synthetic waveforms at R = 14.1 and 18.8 km. At larger ranges the waveforms of the synthetics are elongated by the buildup of P_6, the Moho reflection. The simplicity of the pressure response at 30.9 and 35.0 km is displayed in their waveforms. As we increase the range the mantle head wave begins to separate from the Moho reflection. This is also apparent in the observations especially at R = 47 km. However, the corresponding synthetic record has not reached the same degree of separation. This implies that the critical range, that range where the Moho reflection is at critical angle, for the model occurs too late. In fact, examining the synthetic with the corresponding observed waveforms we see that the first half of the profile, Figure 10, would agree much better if the critical range was reduced by 5 km. This would effectively match the synthetic waveforms of R = 30.9 and 35.9 km with observed R = 27.1 and 30.9 km. The comparison between synthetic and observed waveforms is much better for the second half of the profile, Figure 11, which is controlled by the nature of the crust-mantle transition. We will devote most of this paper to this transition. Adjustments to the upper crust where converted shear waves are also important will be given in Part II.

Examining the observed waveforms of Figure 11 we see many variations in amplitude and shape. Many of these variations are probably caused by using a sinking explosive as a signal generator with the lack of exact positioning and variable yield. However, it does appear that the mantle headwave at separation is much too large compared to the Moho reflection to be a true refraction. Furthermore, it decays much slower than the Moho reflection. We have

tried to produce these effects by introducing the layer in the upper mantle. We think of this layer as representing a velocity gradient since replacing it by two thin layers, maintaining approximately the same velocity depth function, produced about the same synthetic waveforms. If the upper mantle has a low Q then the gradient would, obviously, need to be greater. However, if the gradient is increased any appreciable amount it would be indicated on the travel time plot which it is not.

Two other models were considered, one where the bottom interface or mantle gradient was omitted and one where the mantle had a negative velocity gradient; that is the bottom half space was given the velocity 7.92 km/sec. The pressure responses are shown in Figure 12 and the synthetic waveforms in Figure 13 for R = 84 km. We include the model containing the velocity increase for comparison. Figure 13 suggests that if the upper mantle in this region has a constant velocity it would be very difficult to identify a head wave at ranges greater than about 80 km assuming the same source and receiver. The case of a negative gradient would damp out the head wave even faster.

Finally we consider the sharpness of the Moho transition. Examining Figure 11 we find a relatively quiet zone between the head wave and Moho reflection. If there is a significant transition layer between the crust and the mantle its arrivals would manifest themselves in this zone. To illustrate this point we constructed a model containing a one-kilometer transition layer with velocity of 7.5 km/sec. The results at R = 84 are given in Figure 14. Since the comparison with observations is obviously poor we conclude that the transition is sharp, probably occurring over much less than a kilometer of thickness at this particular station.

COMPARISON OF THEORETICAL AND OBSERVED AMPLITUDES

The amplitude-distance decay curve for the synthetic records was measured using the same method as for the observed records. The comparison is given in Figure 15. While the comparison is not perfect, the decay curve for the synthetic first arrivals has the same general characteristics as that of the observed records. However, the observed amplitudes do decay more rapidly with distance than do the synthetics over the first 50 km. This is probably caused by not having the correct upper crustal model. After studying the ratio of the primary waves to converted shear wave, Part II, we found it necessary to reduce the P-velocities of the upper crust. This adjustment produced a faster amplitude decay with range. Nevertheless, the large observed amplitude at R = 18.8, as well as some of the rather erratic amplitude behavior at large ranges, is not explained. It does not appear that a plane, homogeneous, isotropic layered model can explain such jumps.

CONCLUSION

We have shown that the velocity must increase rapidly at the sea bottom to produce the large amplitudes of the first arrivals at small range. At larger ranges the existence of Moho reflections indicates the sharpness of the crust-mantle transition. In this region the transition zone is probably much less than a kilometer in thickness. The slow decay of mantle head waves with range is explained by a positive velocity gradient in the upper few kilometers of the mantle. To what depth this gradient is maintained cannot be answered by this study due to limited observations.

Acknowledgments. This work was supported by the National Science Foundation under grant NSF GM 7 and by the Office of Naval Research and in part by the Air Force under Contract AF 49(638) - 1763. We are indebted to Drs. R.W. Raitt and G.G. Shor, Jr. who critically read the paper and suggested improvements. We also wish to acknowledge the ship captains and crews and the scientific personnel from Scripps Institution of Oceanography, University of Hawaii, Oregon State University, and the University of Wisconsin who participated in the marine refraction program.

REFERENCES

Cagniard, L., Reflexion et Refraction des ondes Seismiques, Gauthier-Villars, Paris, 1939.

Carpenter, E.W., Teleseismic signals calculated for underground, underwater, and atmospheric explosions, Geophys., 32, 17-32, 1967.

deHoop, A.T., A modification of Cagniard method for solving seismic pulse problems, Appl. Sci. Res., B, 8, 349-356, 1960.

Gilbert, F., Transient response of a fluid-solid interface due to an impulsive pressure-point source, Office of the Director of Defense Bull., 32, 1963.

Helmberger, D.V., and G.B. Morris, A travel time and amplitude interpretation of a marine refraction profile, Part II. Converted shear waves, in preparation.

Helmberger, D.V., Head waves from the oceanic Mohorovicic discontinuity, Bull. Seism. Soc. Am., 58, 179-214, 1968.

Raitt, R.W., Geophysical measurements, Oceanographic Instrumentation, Rancho Santa Fe Conference, 21-23 June 1952, Nat. Acad. Sci., Nat. Res. Council Publ. 309, 1956.

Shor, G.G., Jr., Refraction and reflection techniques and procedure, in The Sea, 3, John Wiley and Sons, New York, 1963.

FIGURE CAPTIONS

Figure 1 Sample recording showing prominent arrivals. The upper three traces are high gain, low frequency (3-20Hz) outputs from three different hydrophones. The center trace is of intermediate frequency (20-200Hz). The lower three traces are low frequency outputs attenuated in magnitude by 20 db compared to the upper three.

Figure 2 Reduced travel time plot and layered model interpretation for refraction profile SH31.

Figure 3 Amplitude decay with distance for profile SH31. Second arrivals correspond to those arrivals in Figure 2 which lie on or near the 6.94 km/sec line and are at distances greater than 50 km. These are a combination of head waves from the oceanic layer and reflections from the Mohorovicic discontinuity.

Figure 4 Amplitude decay with distance for profile SH11.

Figure 5 Transfer function before and after low-pass filtering.

Figure 6 Propagation Operator.

Figure 7 Oceanic crustal model F.

Figure 8 Pressure response versus time after onset assuming a step function pressure source. P_i indicates the reflection time from the bottom layer i.

Figure 9 Continuation of Figure 8. P_6 indicates the Moho reflection time.

Figure 10 Synthetic waveforms based on the pressure responses of Figure 8.

Figure 11 Synthetic waveforms based on the pressure responses of Figure 9.

Figure 12 Pressure responses for a crustal model overlying a mantle with positive gradient, negative gradient and constant velocity.

Figure 13 Synthetic waveforms based on pressure responses of Figure 12.

Figure 14 Pressure response and synthetic waveform for a model containing a transition layer at range 84 km.

Figure 15 Comparison of relative amplitude decay with distance for observed records from profile SH31 and for theoretically calculated synthetic records for model F.

BLANK PAGE

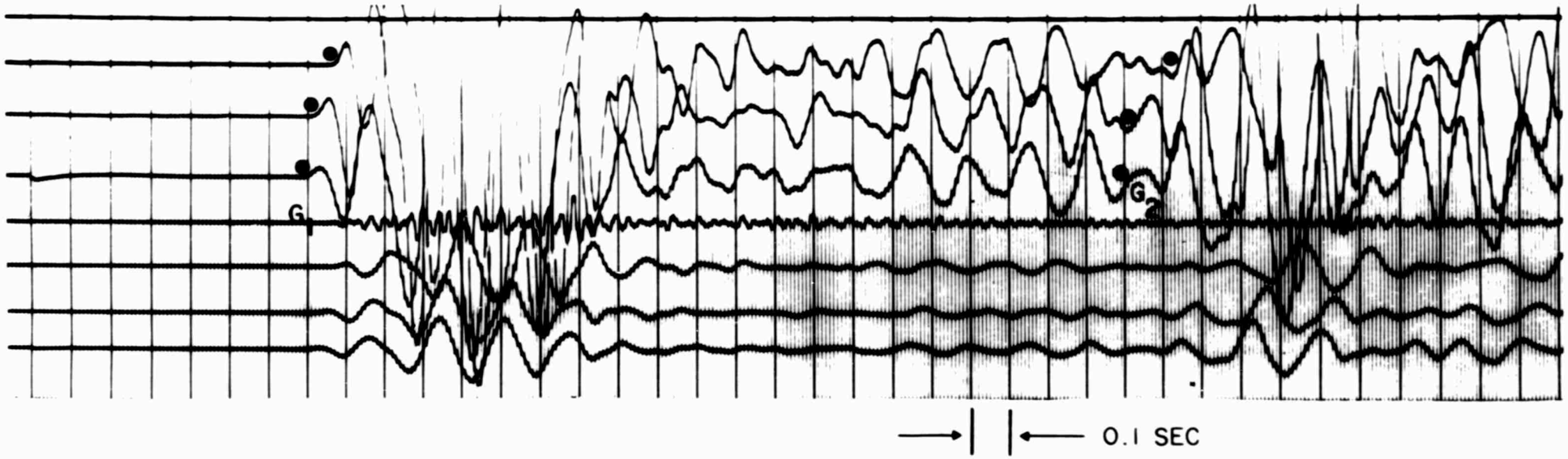

INCREASING TIME ⟶

Fig. 1

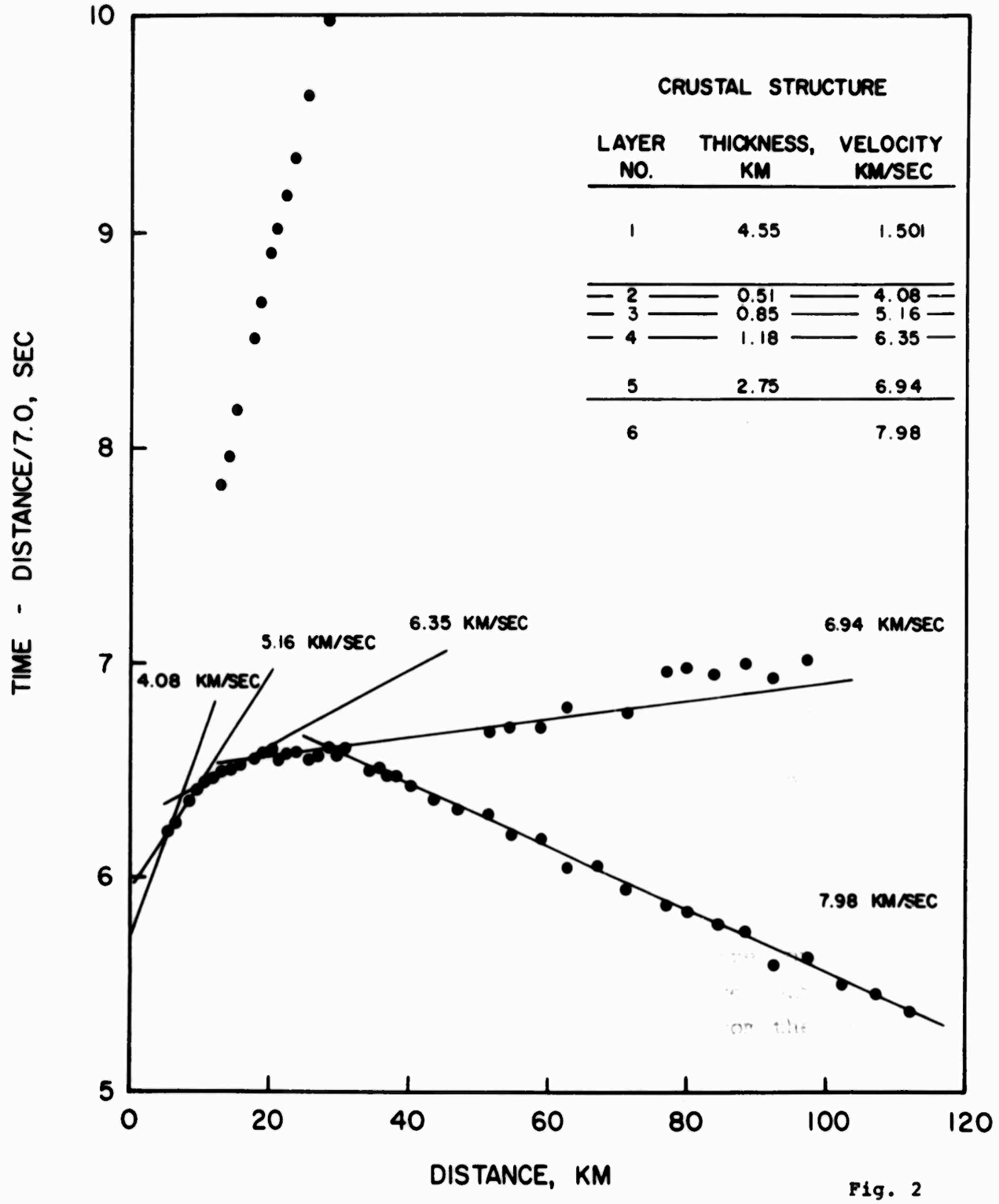
CRUSTAL STRUCTURE
LAYER NO.
THICKNESS, KM
VELOCITY KM/SEC
1
4.55
1.501
2
0.51
4.08
3
0.85
5.16
4
1.18
6.35
5
2.75
6.94
6
7.98
4.08 KM/SEC
5.16 KM/SEC
6.35 KM/SEC
6.94 KM/SEC
7.98 KM/SEC
TIME - DISTANCE/7.0, SEC
DISTANCE, KM
10
9
8
7
6
5
0
20
40
60
80
100
120

Fig. 2

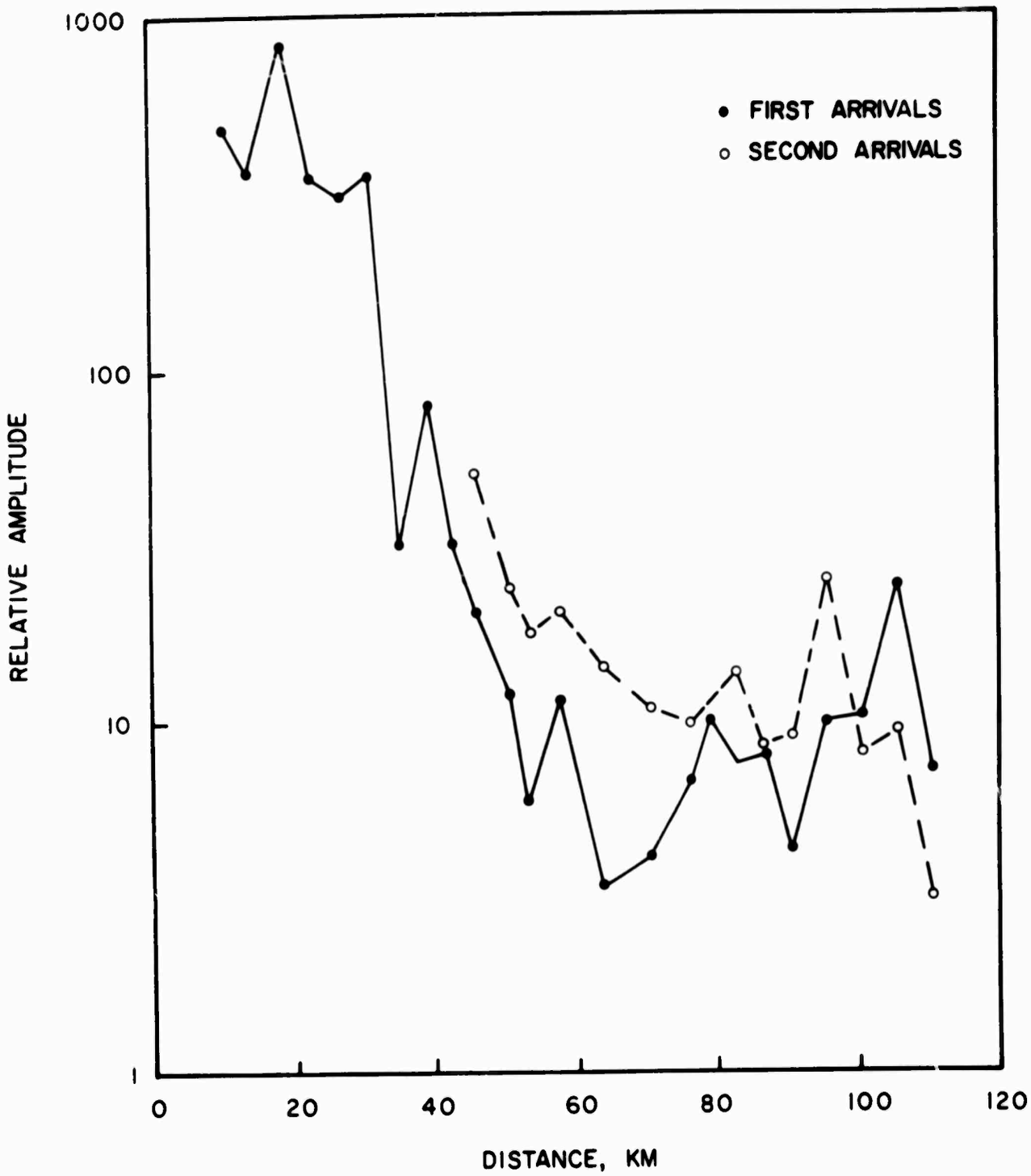
1000
100
10
1
RELATIVE AMPLITUDE
FIRST ARRIVALS
SECOND ARRIVALS
0
20
40
60
80
100
120
DISTANCE, KM

Fig. 3

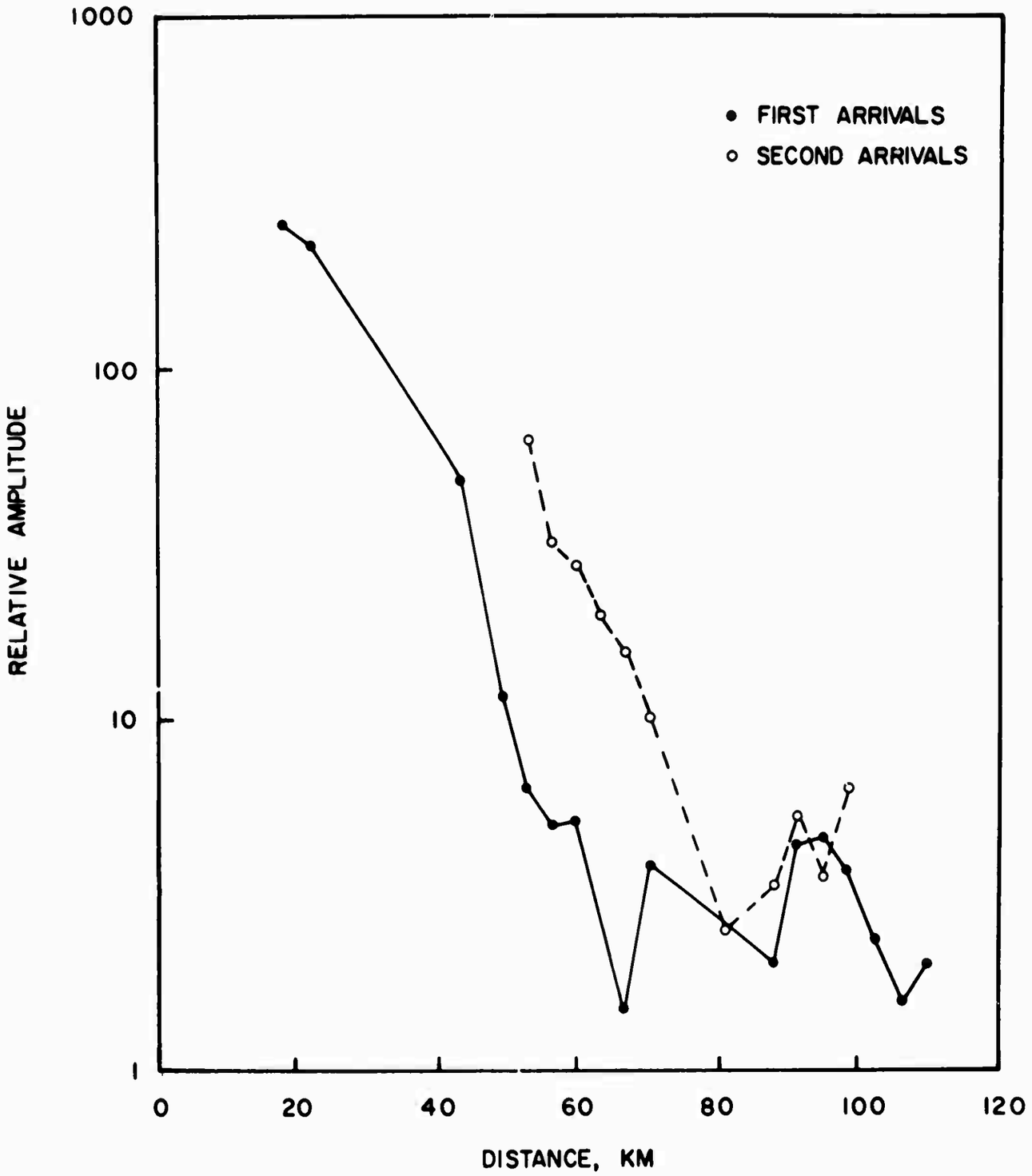
1000
100
10
1
RELATIVE AMPLITUDE
FIRST ARRIVALS
SECOND ARRIVALS
0
20
40
60
80
100
120
DISTANCE, KM

Fig. 4

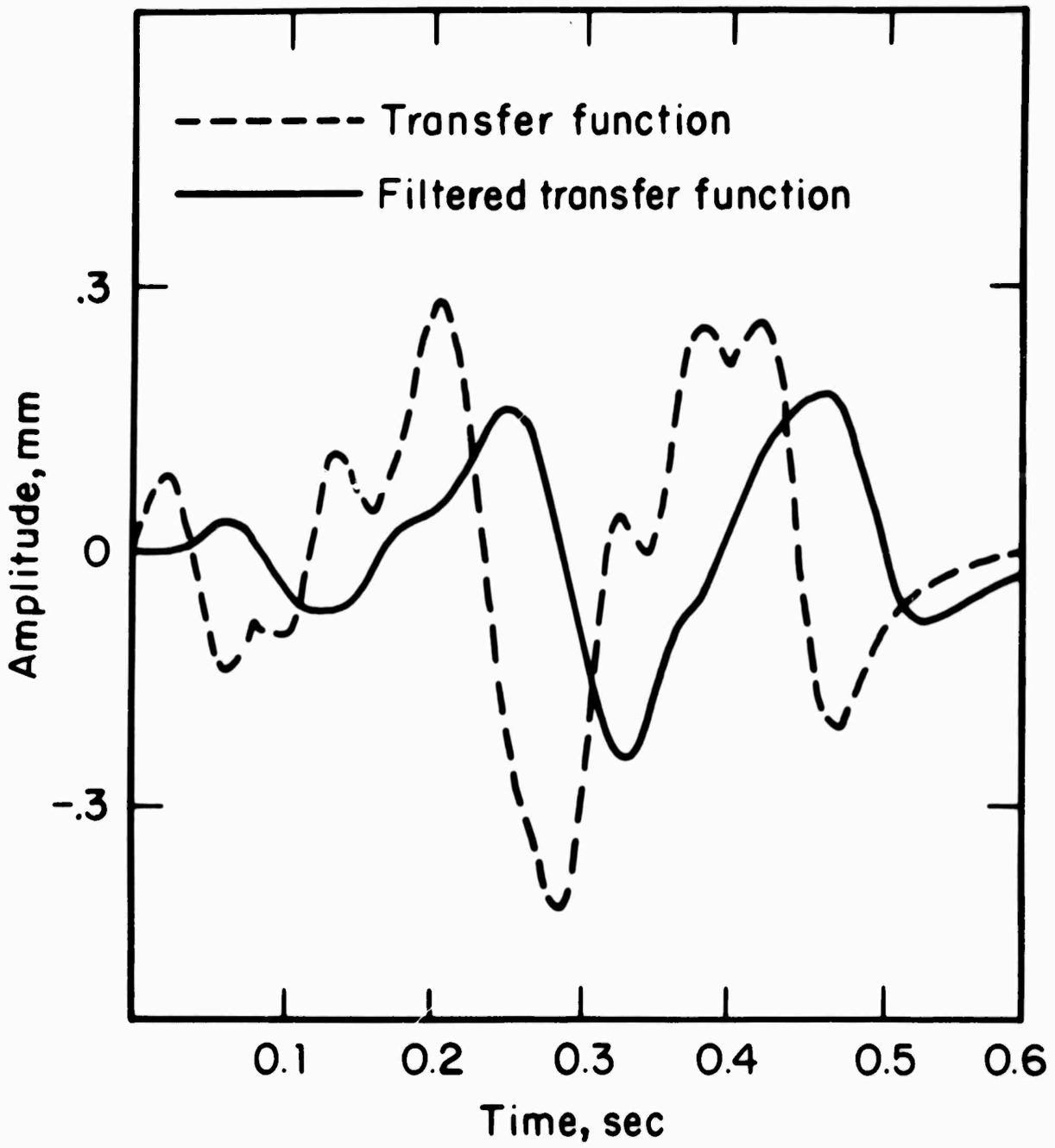
Transfer function
Filtered transfer function
.3
0
-.3
Amplitude, mm
0.1
0.2
0.3
0.4
0.5
0.6
Time, sec

Fig. 5

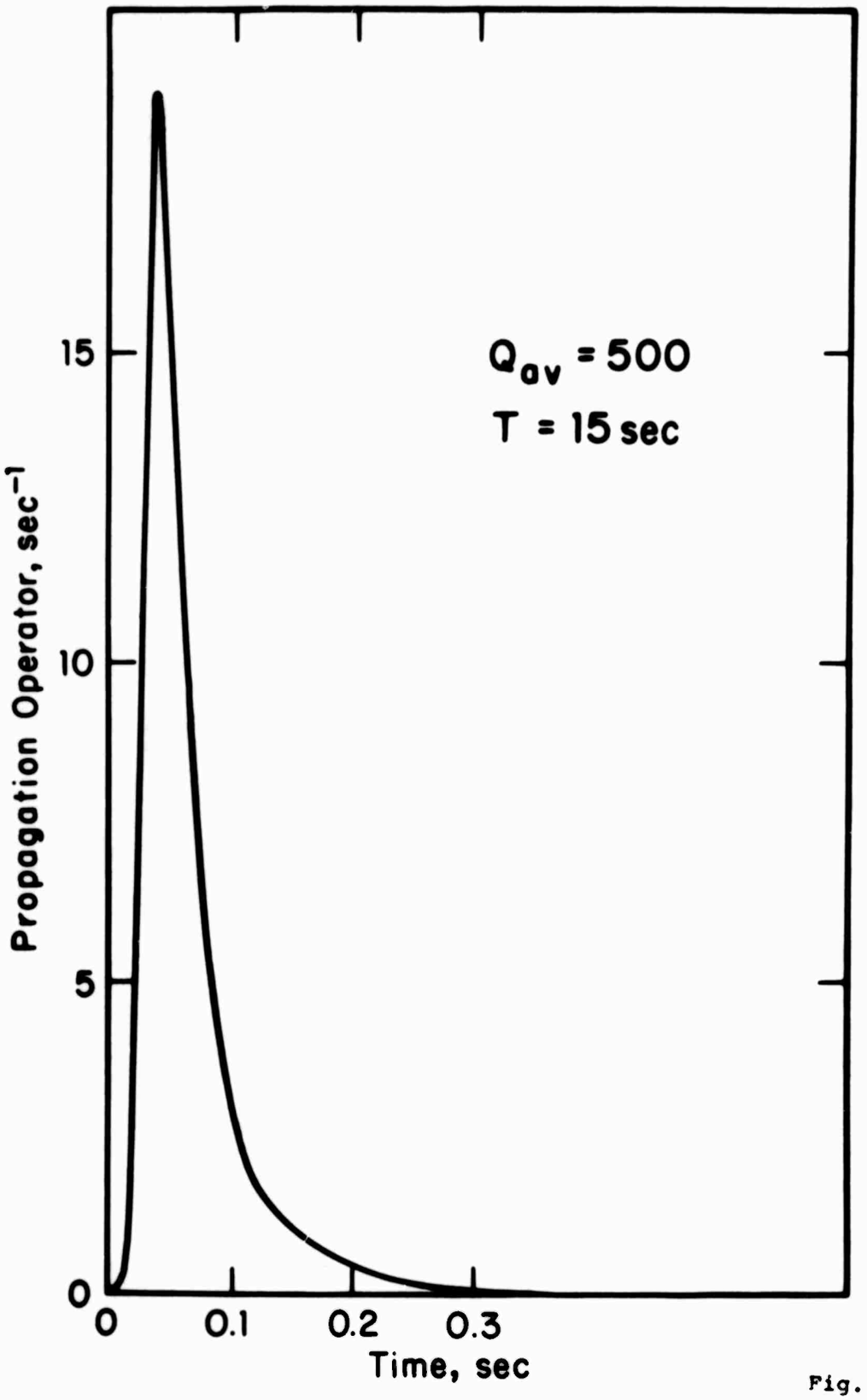
Q_{av} = 500
T = 15 sec
Propagation Operator, sec^{-1}
15
10
5
0
0
0.1
0.2
0.3
Time, sec

Fig. 6

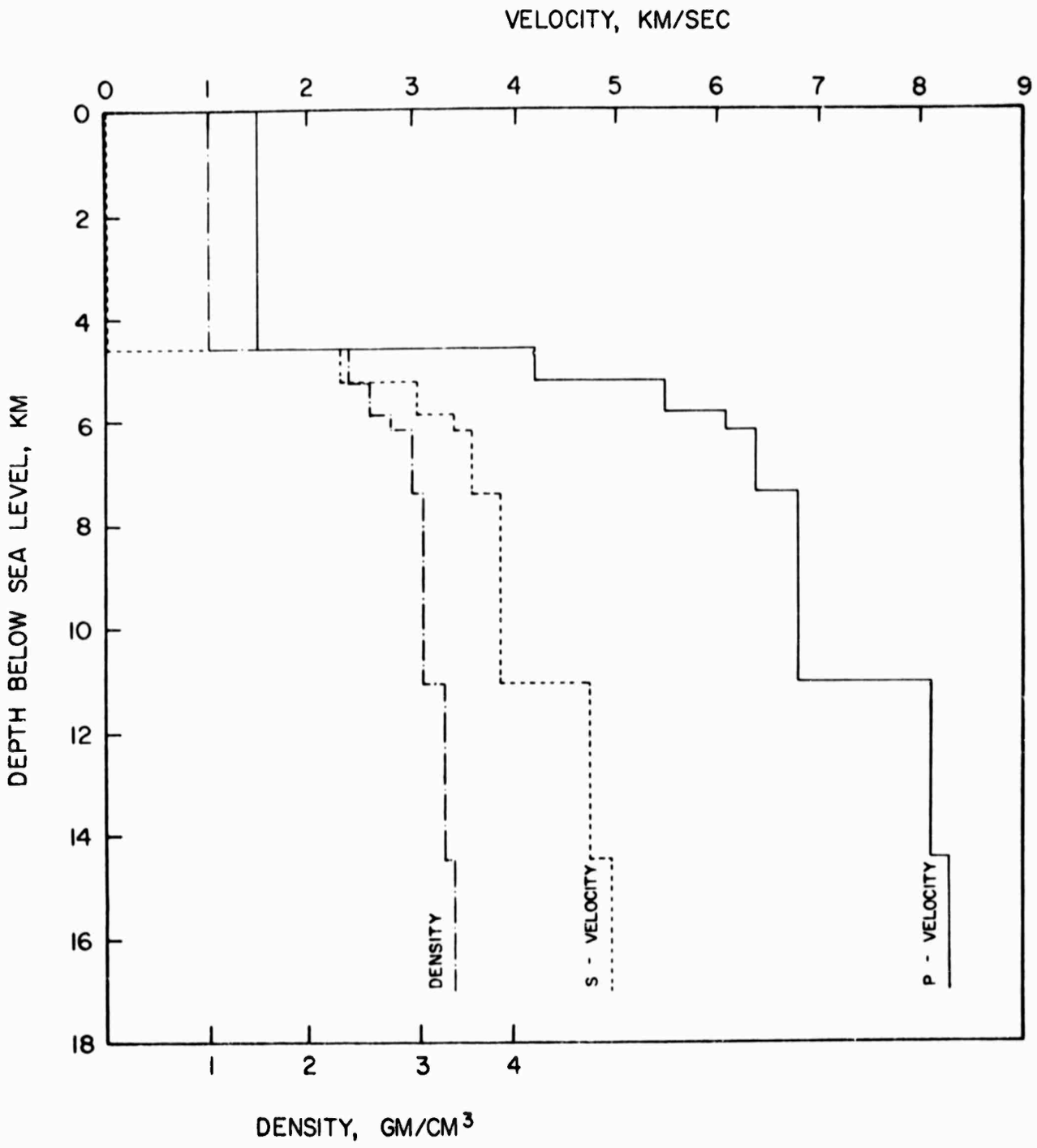
VELOCITY, KM/SEC
0
1
2
3
4
5
6
7
8
9
DEPTH BELOW SEA LEVEL, KM
0
2
4
6
8
10
12
14
16
18
DENSITY
S - VELOCITY
P - VELOCITY
1
2
3
4
DENSITY, GM/CM3

Fig. 7

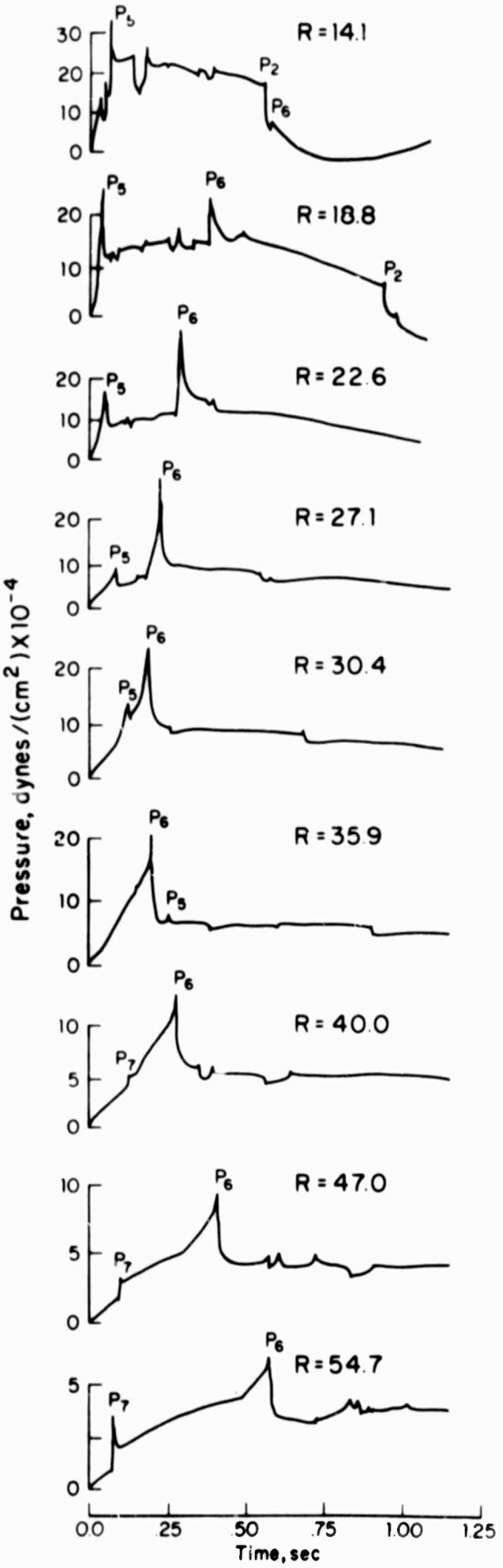
R = 14.1
R = 18.8
R = 22.6
R = 27.1
R = 30.4
R = 35.9
R = 40.0
R = 47.0
R = 54.7
P5
P2
P6
P7
Pressure, dynes/(cm²) X 10⁻⁴
Time, sec
0.0
.25
.50
.75
1.00
1.25

Fig. 8

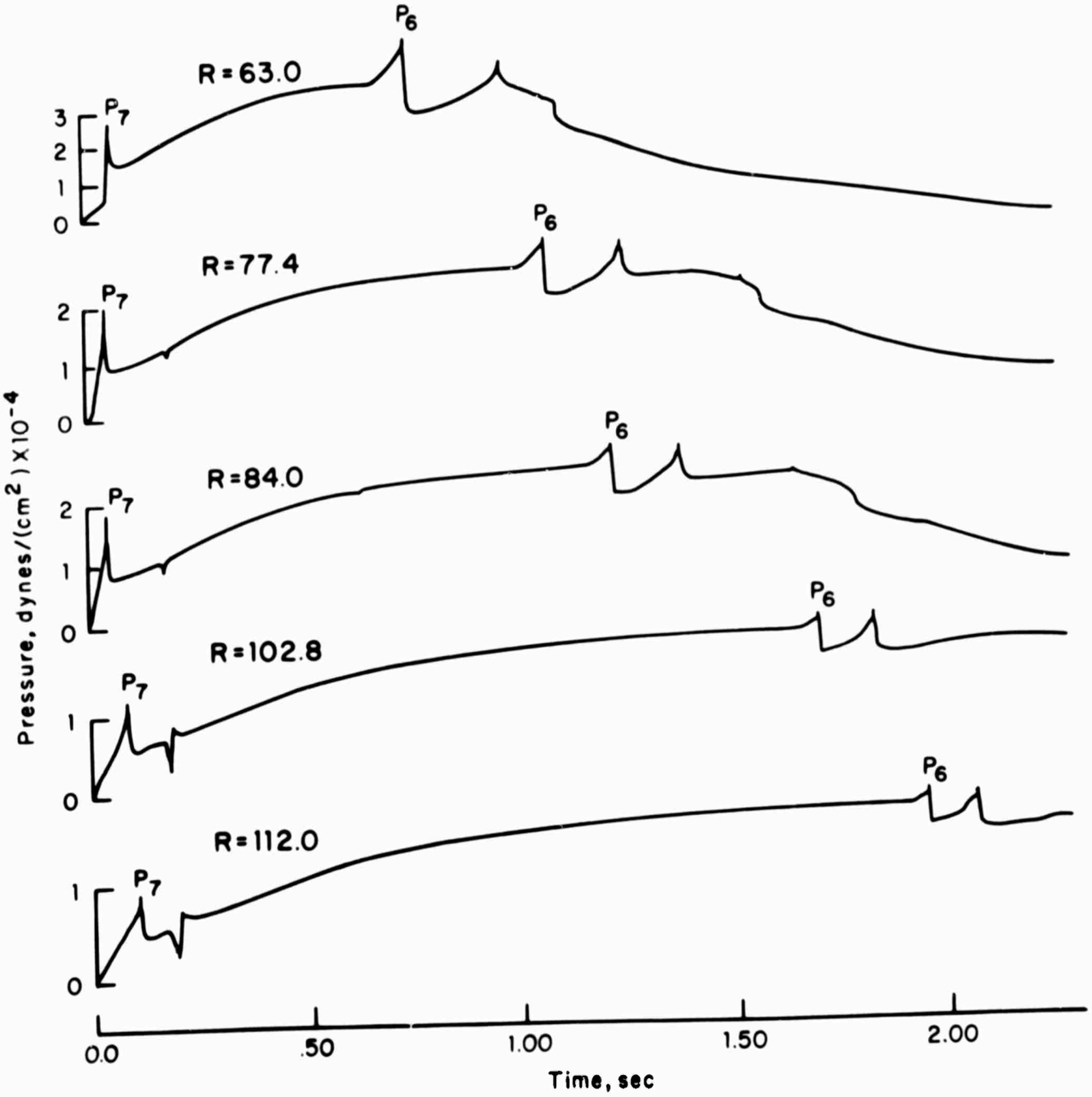
R=63.0
R=77.4
R=84.0
R=102.8
R=112.0
P6
P7
Pressure, dynes/(cm2) X10-4
Time, sec
0.0
.50
1.00
1.50
2.00

Fig. 9

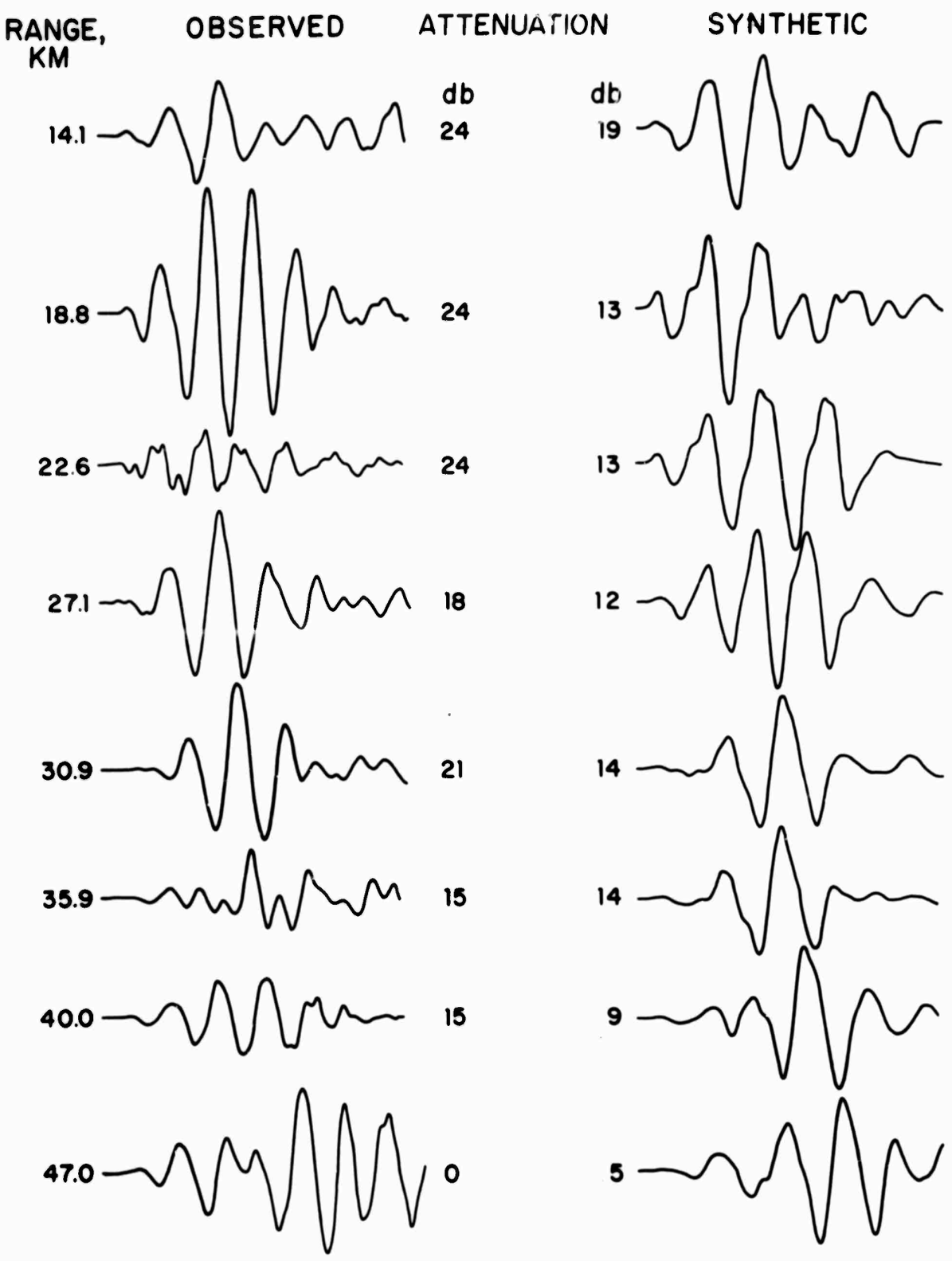
RANGE, KM
OBSERVED
ATTENUATION
SYNTHETIC
db
db
14.1
24
19
18.8
24
13
22.6
24
13
27.1
18
12
30.9
21
14
35.9
15
14
40.0
15
9
47.0
0
5

Fig. 10

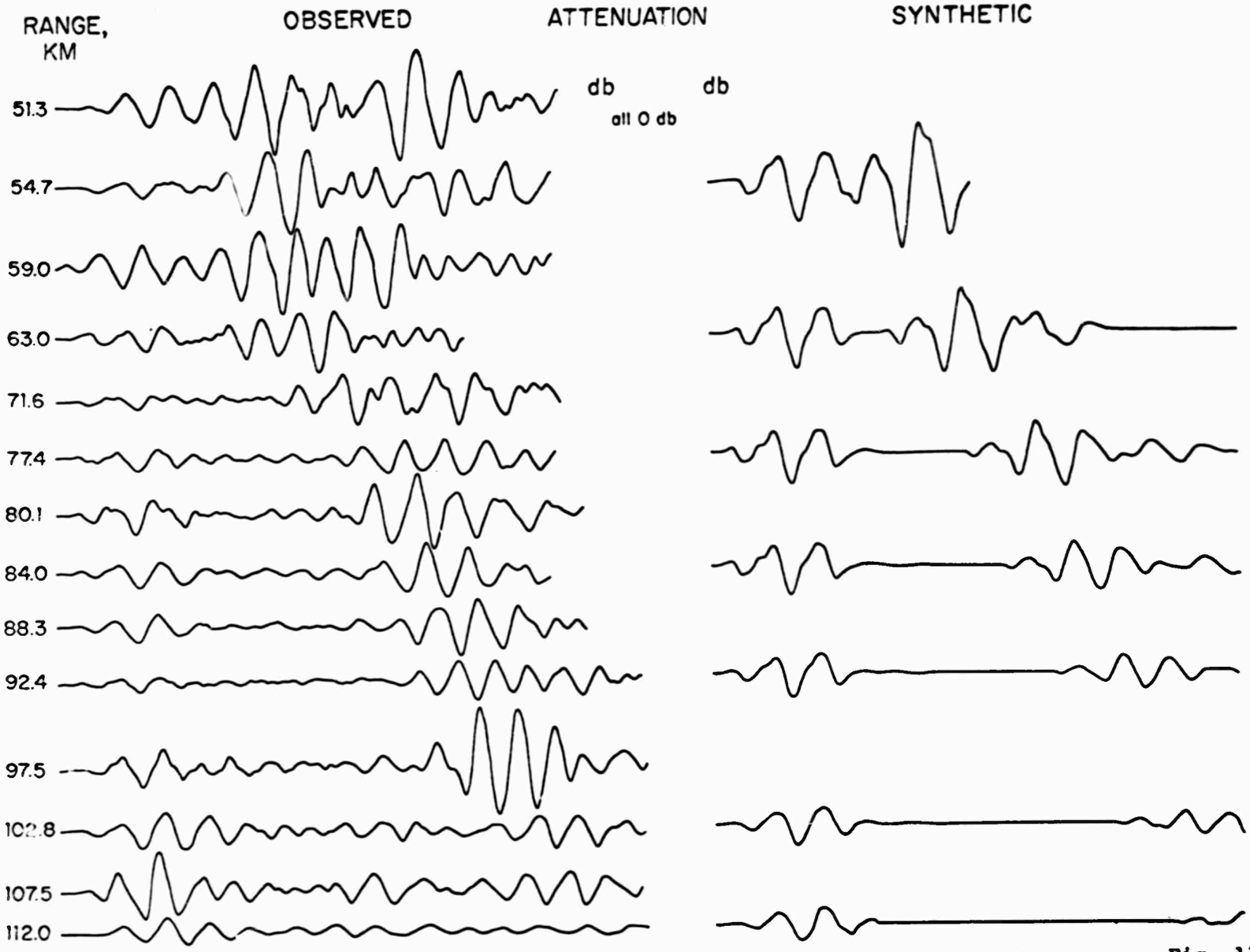
RANGE, KM
OBSERVED
ATTENUATION
SYNTHETIC
db
all 0 db
db
51.3
54.7
59.0
63.0
71.6
77.4
80.1
84.0
88.3
92.4
97.5
102.8
107.5
112.0

Fig. 11

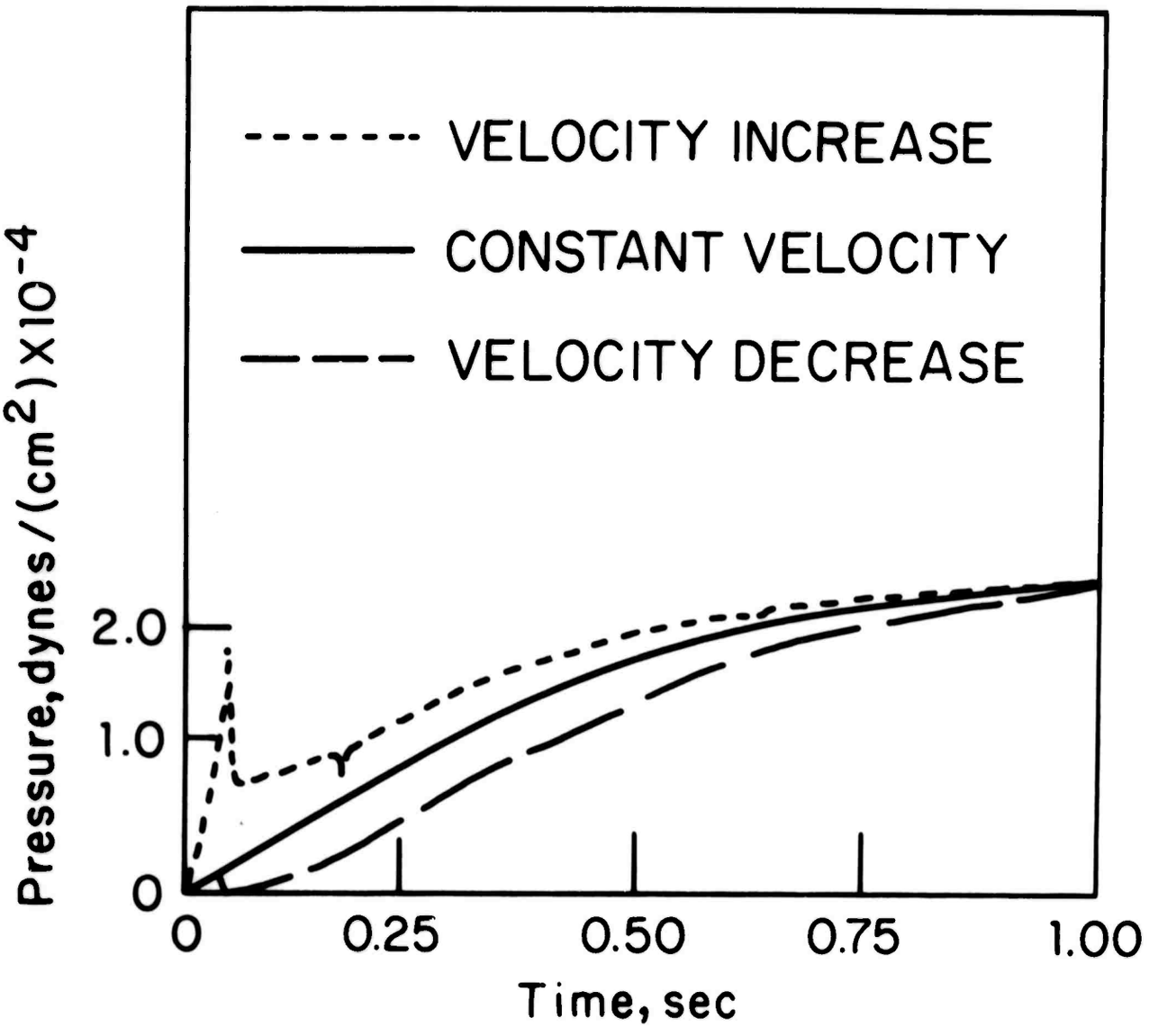
VELOCITY INCREASE
CONSTANT VELOCITY
VELOCITY DECREASE
Pressure, dynes/(cm^2) X10^{-4}
2.0
1.0
0
0
0.25
0.50
0.75
1.00
Time, sec

Fig. 12

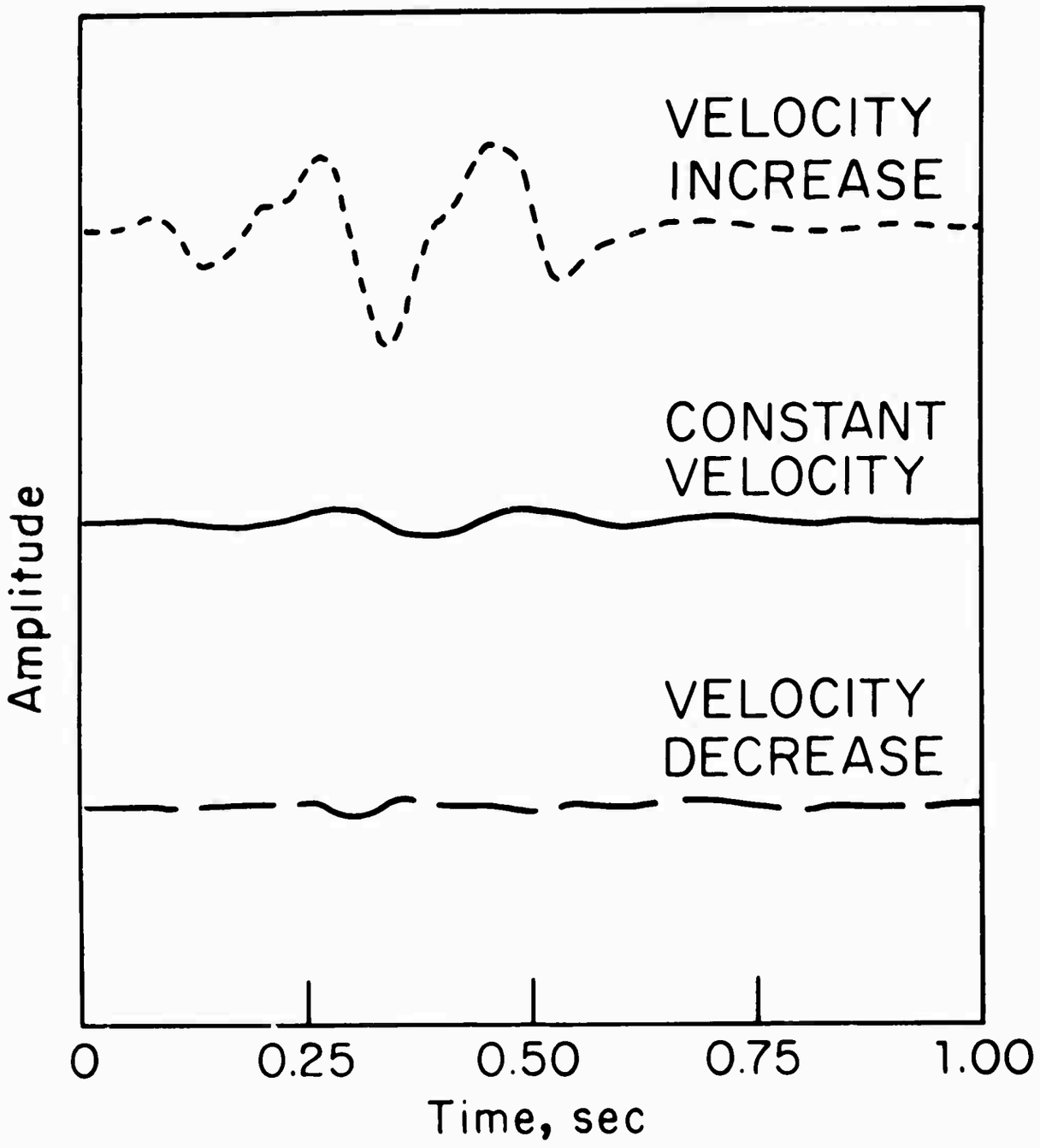
VELOCITY
INCREASE
CONSTANT
VELOCITY
VELOCITY
DECREASE
Amplitude
0
0.25
0.50
0.75
1.00
Time, sec

Fig. 13

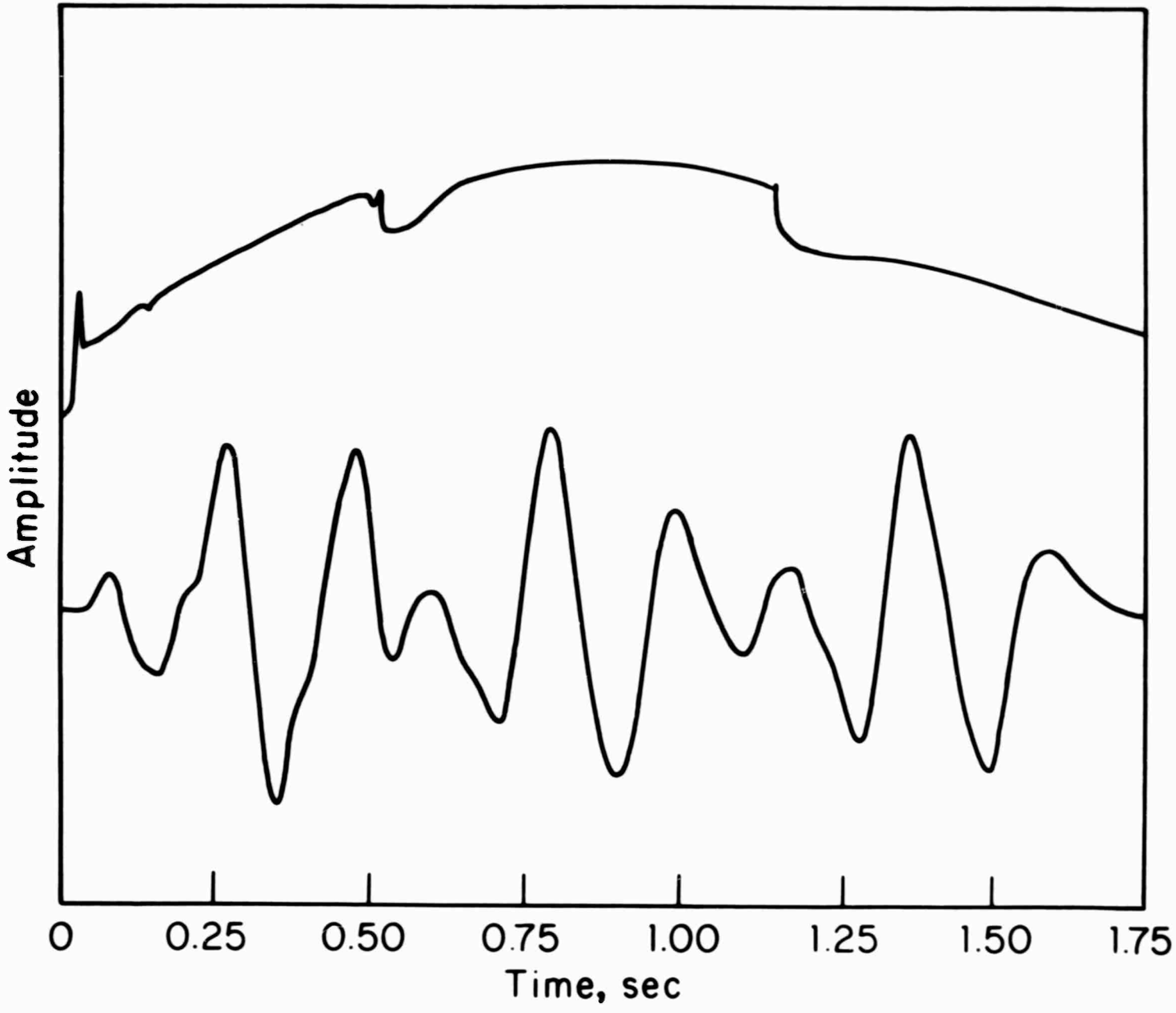

Fig. 14

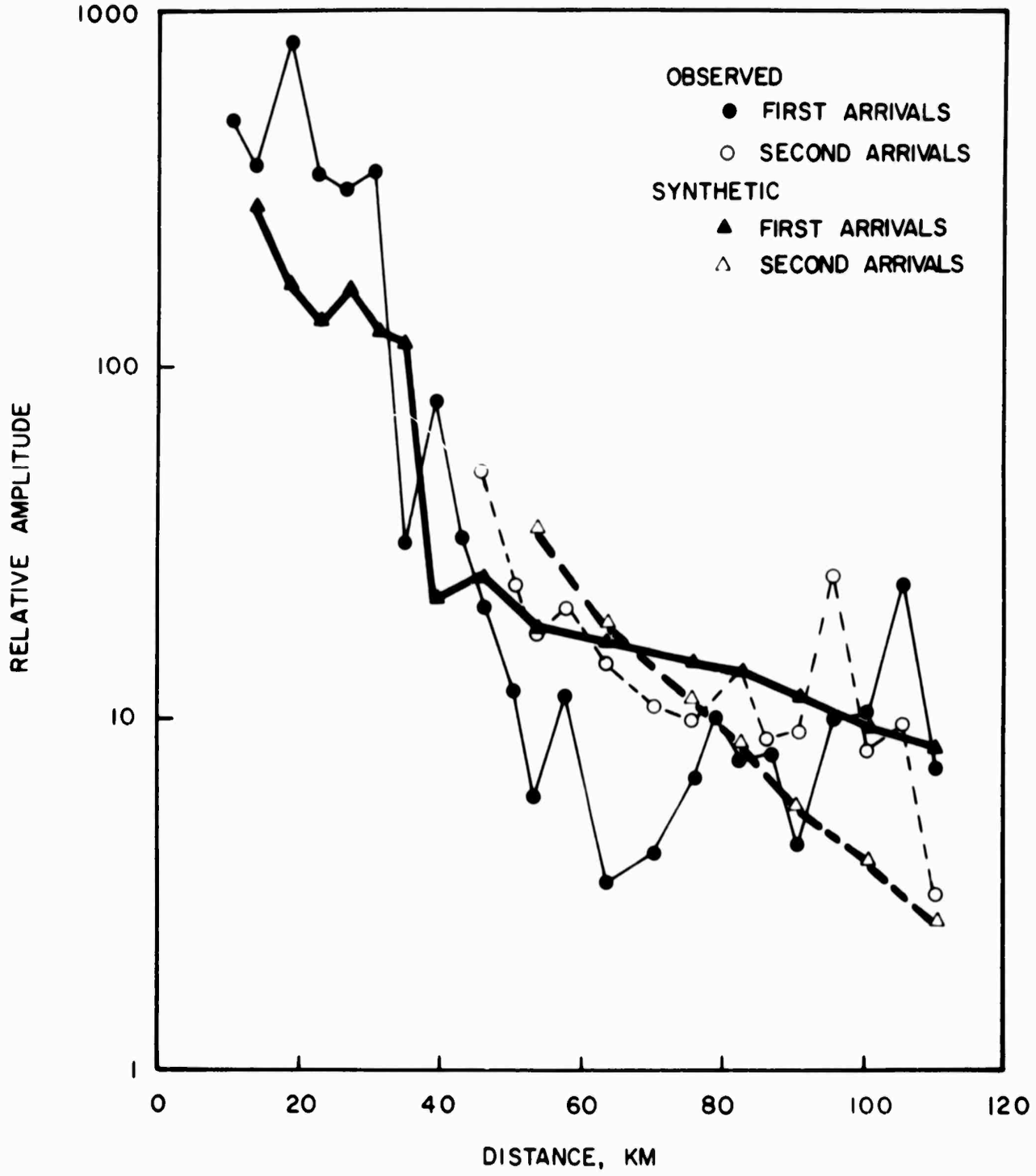
1000
100
10
1
RELATIVE AMPLITUDE
OBSERVED
FIRST ARRIVALS
SECOND ARRIVALS
SYNTHETIC
FIRST ARRIVALS
SECOND ARRIVALS
0
20
40
60
80
100
120
DISTANCE, KM

Fig. 15

BLANK PAGE

III.2-2: Converted Shear Waves

In a recent paper by the authors part 1, (Helmberger, Morris, 1968) synthetic primary waves for some oceanic crustal models were compared with a profile of observations. At short ranges, R < 50 km, a rather large second arrival is observed which has the apparent velocity of a shear wave, see Figures (2) and (3). We will label such arrivals converted shear waves, waves that travel through the ocean as primary waves and in the solid crust as shear waves. It is found that these generalized rays have a behavior similar to primary waves. That is the summation of rays leads to a large arrival which increases its velocity as a function of range.

The model studied in part 1 agreed well at large ranges (50 to 112 km) where the waveforms are dominated by the structure near the crust-mantle transition. The model indicated a sharp crust-mantle boundary with a small positive velocity gradient in the upper mantle. However, this model did not agree very well at short ranges where the critical Moho reflection of the model occurs at about 5 kms greater range than the observed. Before computing converted shear waves we will adjust the crustal structure to rectify this apparent disagreement.

Mode Conversion

One of the disadvantages of using generalized ray theory in synthetic seismogram generation is the troublesome problem of conversion of wave types at interfaces. This would not be such a difficulty if one was not forced to use many layers to approximate crustal structures. However, it appears that many generalized rays containing mixed mode paths can be neglected at certain ranges. In a recent paper (Helmberger, 1968) a procedure was presented for calculating the response for a sandwiched layer, including mixed mode paths. The numerical results for a one layer crustal model is given in Fig. 1 where the transfer function of part 1 was used as it will be throughout this study. The seismograms at R=19 and 32 km contain the first and second set of generalized rays. Only the first set is included at R=25 km. It is clear from Fig. 1 that the first set yields the principal contributions at the larger ranges. The results show that P to S mode conversion is the strongest at shorter ranges and drops off rapidly approaching the P-mode critical angle. Fig. 1 should be compared with Fig. 2 which displays part of the profile of observations studied in part 1. Fig. 3 is along the same profile but where two pound charges were used to generate the seismic signals. Note the difference in the principal period of the waveforms of Fig. 3 compared to those of Fig. 2. This is caused by the variation in bubble size which is predictable. The comparison of Fig. 1 with Fig. 2 and 3 suggest that PP and SS are idealized G_1 and G_2 respectively at the larger ranges. This identification will be supported by this study. Ond of the largest discrepancies is the ratio of PP to SS as compared to G_1 and G_2. This is caused by the large P-velocity contrast at

the ocean bottom interface. By reducing the upper crustal velocity the ratio of PP to SS will be enhanced, also the amplitude of Pr, now a diffracted wave caused by the gradient, will be greatly increased at the nearest ranges. The travel time between Pr and PP will also be reduced and, as we will see, these two events will interfere approaching the PP critical angle. Note the disturbances in G_1 and G_2 at about R=25 km. Examining the top three recordings in Fig. 3 it appears that the signals between G_1 and G_2 could well be mode conversions since they decay rapidly with range. It would be gratifying to show this formally by summing all possible generalized rays but this would be very time consuming. We will neglect these mode conversions in this study and compute G_1 based on P-mode and G_2 based on S-mode exclusively. That is we will allow changes only in mode crossing the ocean bottom interface.

Crustal Model

The structure near the crust-mantle transition was adequately determined in part 1 which we will incorporate into our new model. Suppose we reinterpret the travel time plot given in Fig. 4 by adding layers in the upper crust. The added criterion being that the new model has its critical Moho reflection at about 26 km and that the Moho reflection, at large ranges, has the proper lag behind the head wave. The model candidates can be easily checked against the above criterion by applying the first-motion approximations discussed by Helmberger (1968). A model passing these tests is given in Fig. 4, found by trial and error. The model contains the same gradient in the upper mantle as discussed in Part 1, that is .05 km/sec per km. Synthetic seismograms constructed exclusively from P-mode paths are shown in Fig. 5 which should be compared with Figures 2 and 3. At the shortest ranges the summation of reflections from the upper crustal interfaces produce the principal motion which may be interpreted as the direct wave turned back by the velocity gradient. Interference is produced when this event approaches the Moho reflection at larger ranges as dramatically indicated at R=22.7 in Figures 2 and 5. The same phenomeno occurs in G_2 at R=27.1. As we increase the range the synthetic seismograms approach those generated in part 1 since the lower structure is similar.

Converted Shear Waves

The S-velocity model was determined by applying the standard refraction interpretation technique but where the layer thicknesses are already assigned. The resulting model is not as well determined as the P-velocity model since the observations are limited to 40 km. The model used in this study is given in Fig. 4. A profile of pressure responses based on this model is displayed in Fig. 6, assuming a step function source. The responses are the summation of generalized rays including multiple reflected paths within the various layers. The long period precursor is the Rayleigh wave which, of course, is not excited by our source function. The crustal arrivals add up to produce the large negative peak S_g at R=14.1 km which can be interpreted as the direct wave turned around by the velocity gradient. As we go to larger ranges the Moho reflection builds up denoted by S_m. These two arrivals interact as they approach each other. Convolving the pressure response with the derivative of the transfer function with respect to time produces the synthetic seismograms plotted in Fig. 5. Comparing Fig. 5 with the corresponding observations displayed in Fig. 2 we find a reasonably good fit except that the observed shear waves appear to die out rather abruptly. We can not explain this feature presently. Furthermore, the P- ode generalized ray that is once reflected in the ocean layer arrives on top of the shear wave at about 42 km which complicates the situation. A number of other stations are now being studied to help clarify this discrepancy and, if possible, identify the mantle shear head wave.

Figure Captions

Figure 1 — One layer oceanic crustal model and synthetic responses. Velocities in km/sec, thicknesses in km.

Figure 2 — Observed recordings from a profile of 85 kg charges.

Figure 3 — Observed recordings from a profile of 2 pd charges. All recordings on the same amplitude scale.

Figure 4 — Reduced travel time plot and layered model interpretation.

Figure 5 — Synthetic seismograms from a profile of 85 kg charges assuming the model given in Fig. 4.

Figure 6 — Pressure response versus time after onset assuming a step function pressure source. Sq is the summation of upper layer responses and Sm is the Moho response.

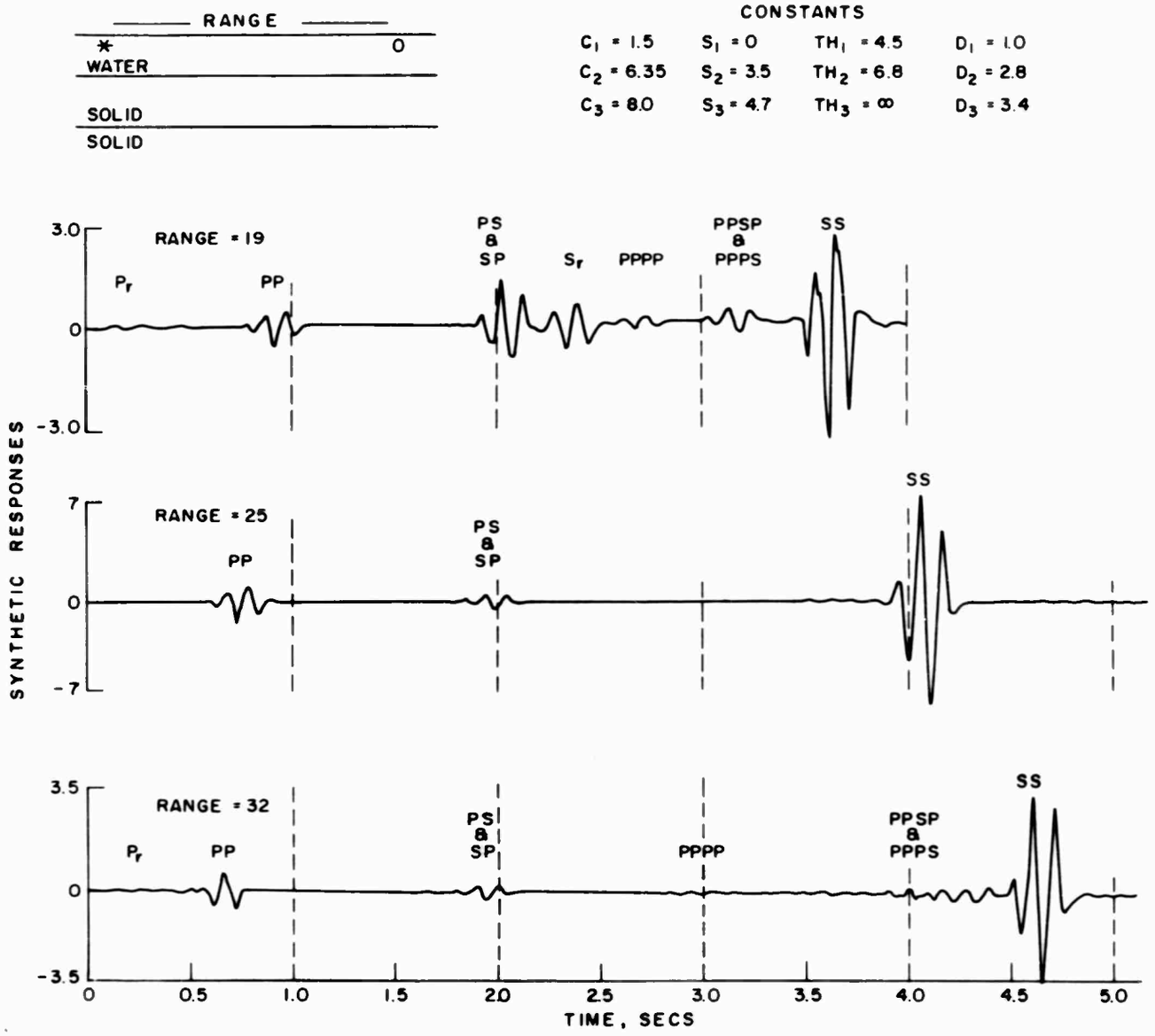
RANGE
*
0
WATER
SOLID
SOLID
CONSTANTS
C1 = 1.5 S1 = 0 TH1 = 4.5 D1 = 1.0
C2 = 6.35 S2 = 3.5 TH2 = 6.8 D2 = 2.8
C3 = 8.0 S3 = 4.7 TH3 = ∞ D3 = 3.4
SYNTHETIC RESPONSES
RANGE = 19
Pr
PP
PS & SP
Sr
PPPP
PPSP & PPPS
SS
3.0
0
-3.0
RANGE = 25
PP
PS & SP
SS
7
0
-7
RANGE = 32
Pr
PP
PS & SP
PPPP
PPSP & PPPS
SS
3.5
0
-3.5
0
0.5
1.0
1.5
2.0
2.5
3.0
3.5
4.0
4.5
5.0
TIME, SECS

Fig. 1

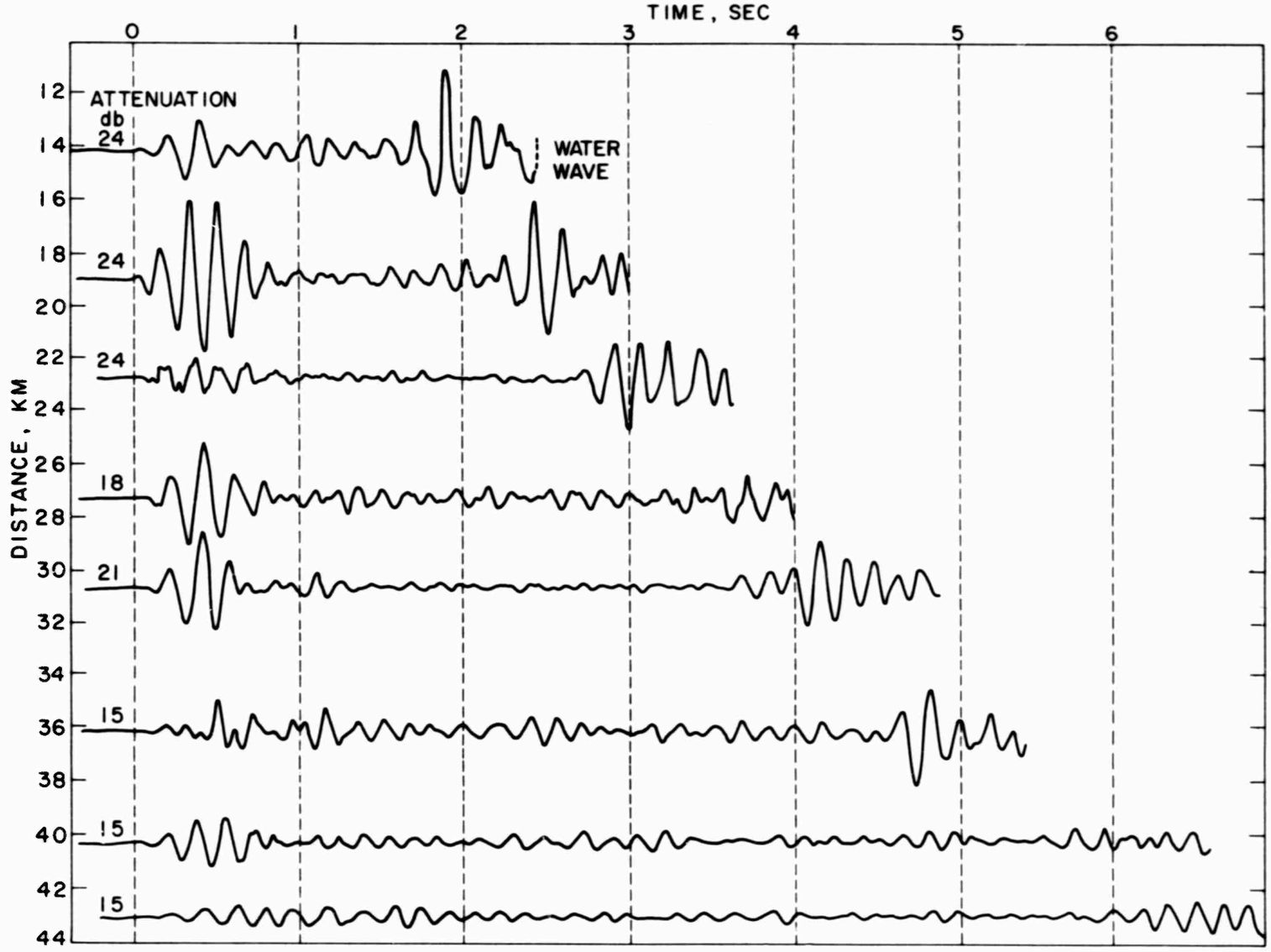
TIME, SEC
0
1
2
3
4
5
6
DISTANCE, KM
12
14
16
18
20
22
24
26
28
30
32
34
36
38
40
42
44
ATTENUATION
db
24
WATER
WAVE
24
24
18
21
15
15
15

Fig. 2

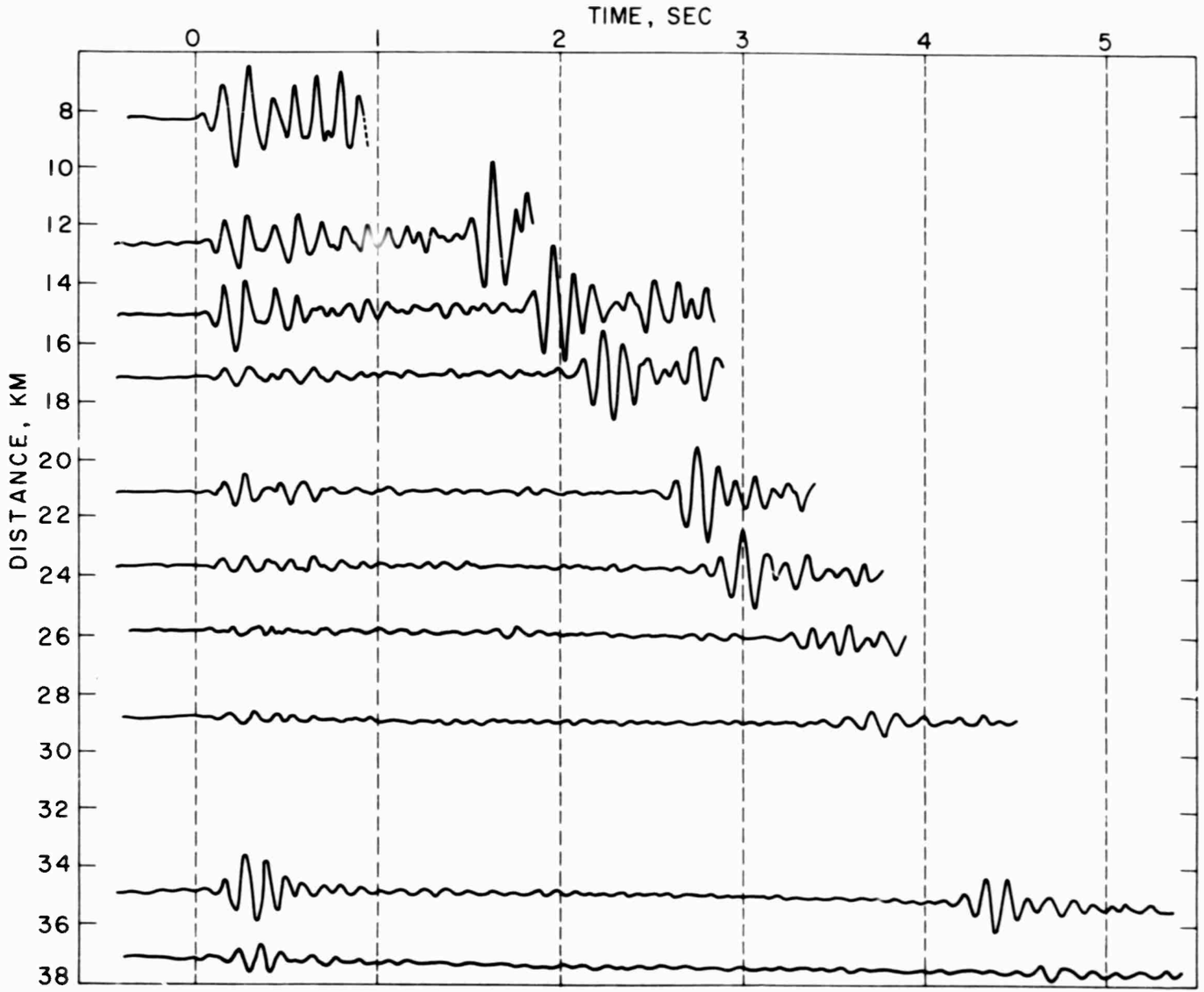
TIME, SEC
0
2
3
4
5
DISTANCE, KM
8
10
12
14
16
18
20
22
24
26
28
30
32
34
36
38

Fig. 3

LAYER NO.	THICKNESS KM	P-VEL. KM/SEC	S-VEL. KM/SEC	DENSITY
1	4.55	1.5	0.	1.0
2	.25	3.5	2.0	2.2
3	.3	4.35	2.4	2.4
4	.4	5.16	2.8	2.5
5	.5	5.8	3.2	2.7
6	.5	6.3	3.5	2.8
7	.8	6.55	3.65	2.9
8	2.5	6.75	3.8	3.0
		8.0	4.6	3.3

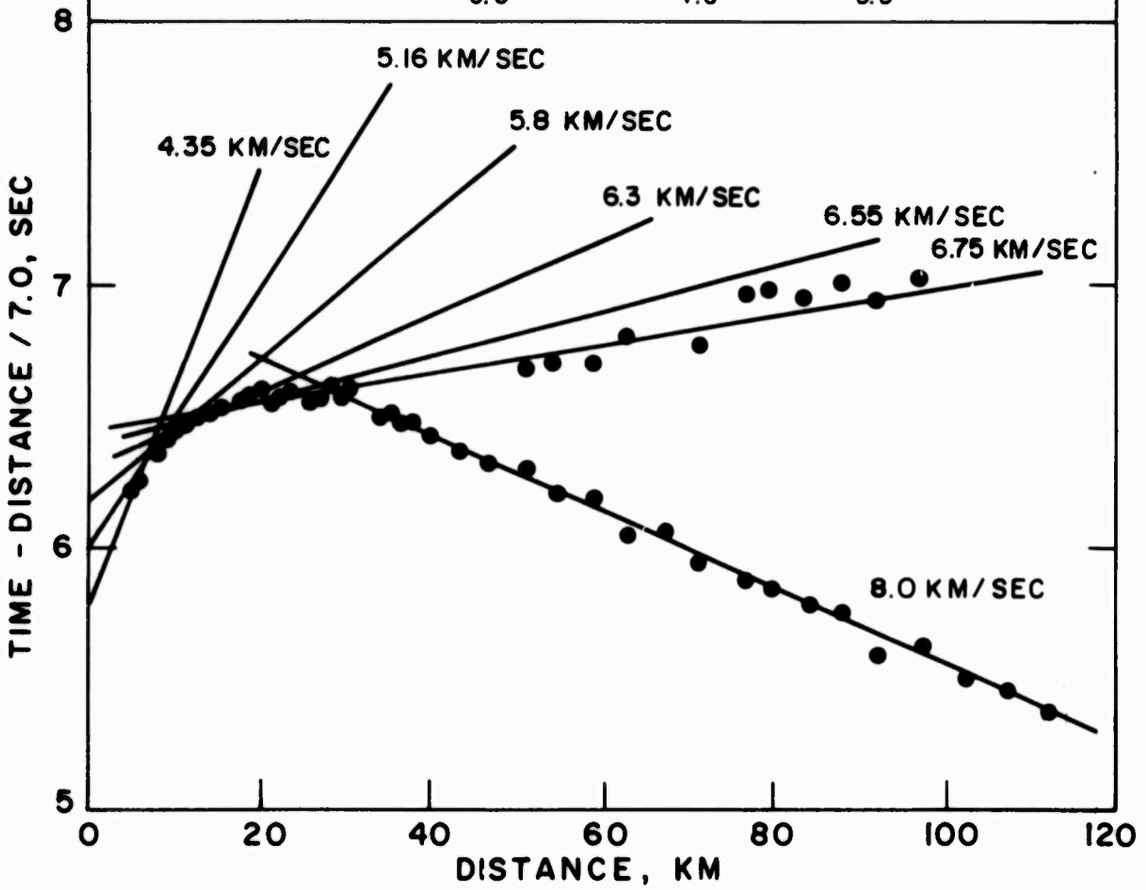

Fig. 4

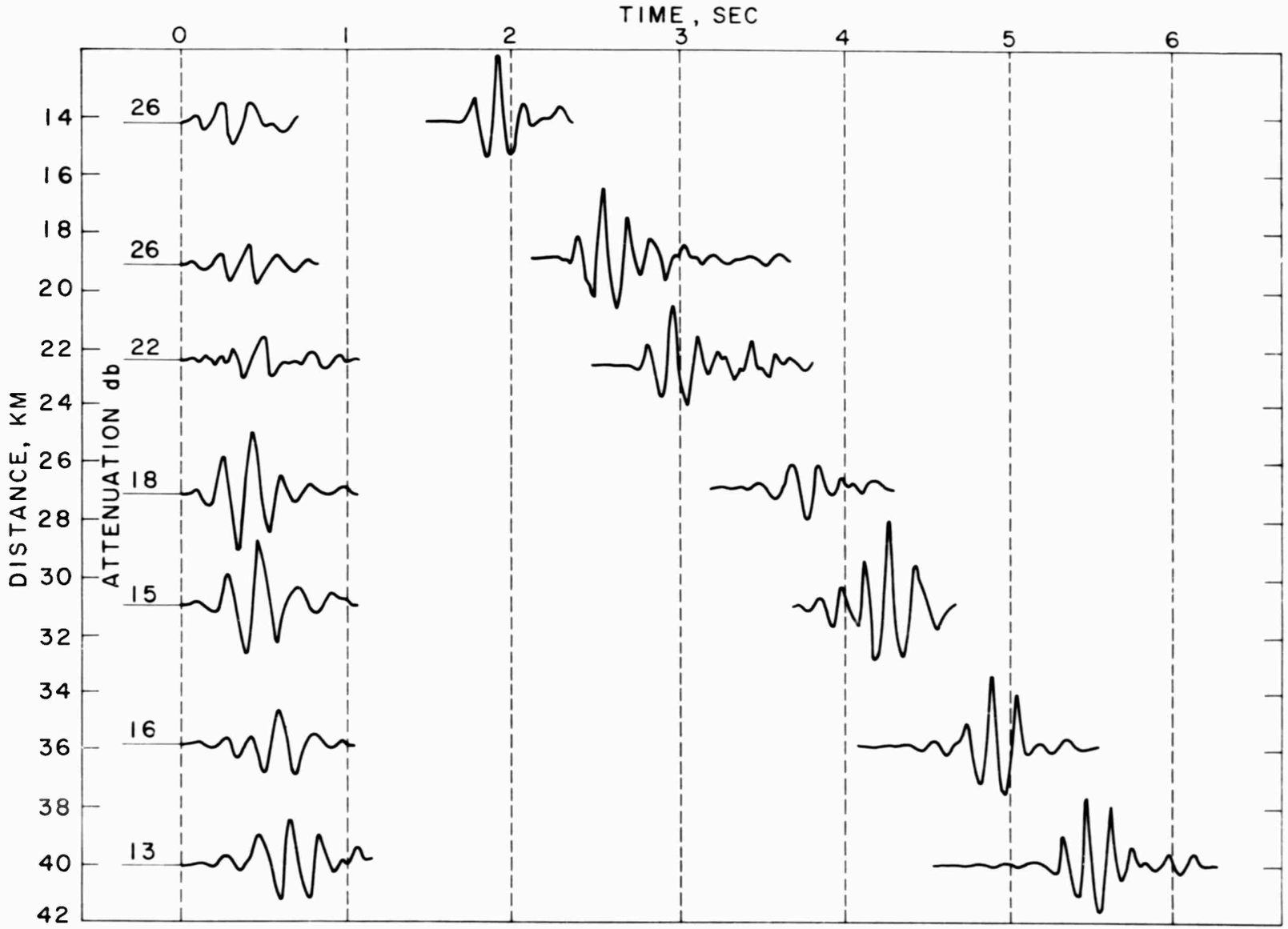
TIME, SEC
0
1
2
3
4
5
6
DISTANCE, KM
ATTENUATION db
14
16
18
20
22
24
26
28
30
32
34
36
38
40
42
26
26
22
18
15
16
13

Fig. 5

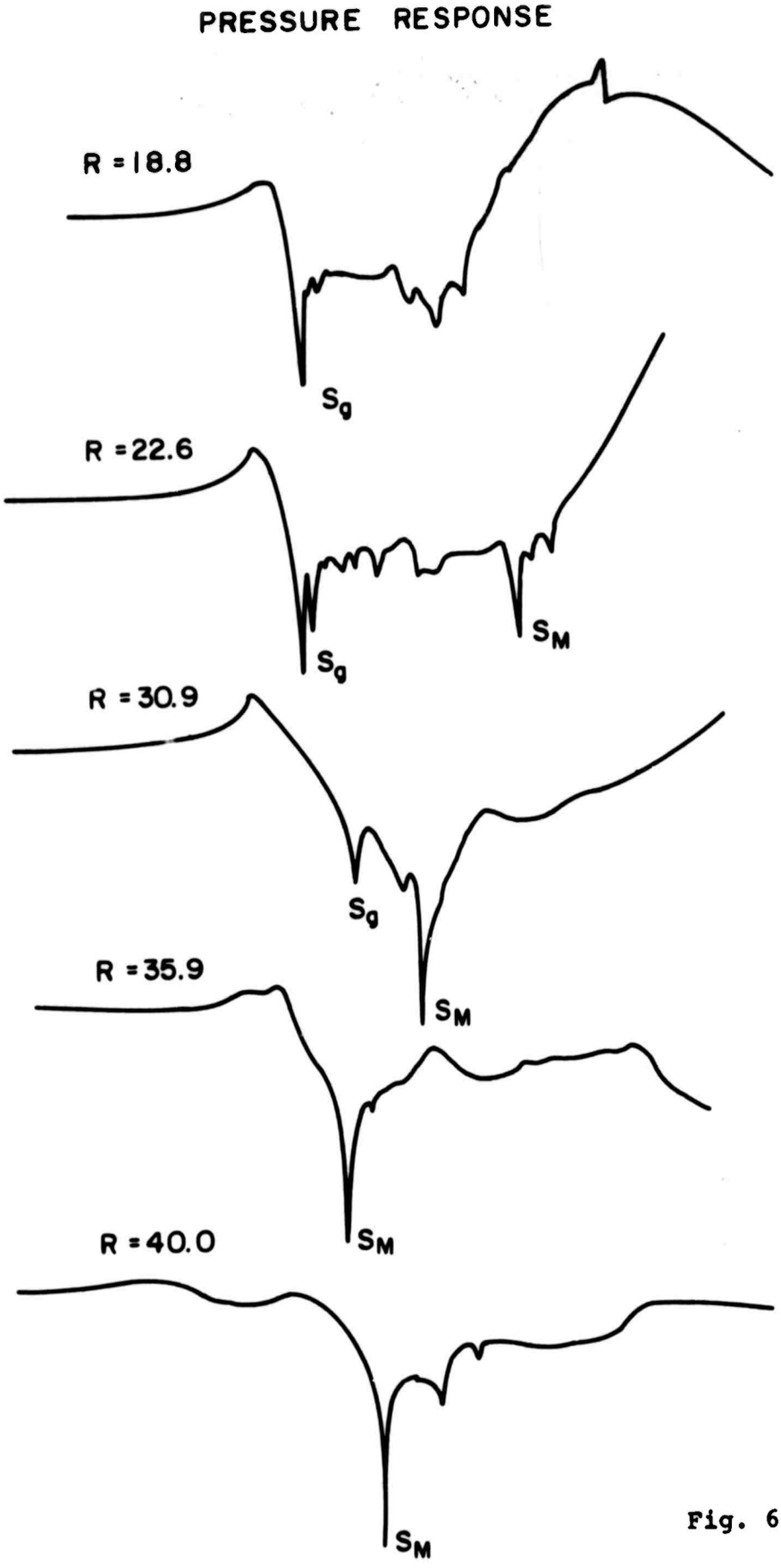
PRESSURE RESPONSE
R = 18.8
Sg
R = 22.6
Sg
SM
R = 30.9
Sg
SM
R = 35.9
SM
R = 40.0
SM

Fig. 6

Unclassified

Security Classification

DOCUMENT CONTROL DATA - R & D

(Security classification of title, body of abstract and indexing annotation must be entered when the overall report is classified)

1 ORIGINATING ACTIVITY (Corporate author)

Massachusetts Institute of Technology
Department of Geology and Geophysics
Cambridge, Massachusetts 02139

2a. REPORT SECURITY CLASSIFICATION

Unclassified

2b. GROUP

3 REPORT TITLE

Post-Doctoral Program in Seismology

4 DESCRIPTIVE NOTES (Type of report and inclusive dates)

Scientific:...Annual (1 July 1967 - 30 June 1968)

5 AUTHOR(S) (First name, middle initial, last name)

Frank Press (also, M. Nafi Toksöz; Keiiti Aki; Paul E. Green; Edward J. Kelly, Jr.)

6 REPORT DATE	7a. TOTAL NO OF PAGES	7b. NO. OF REFS
30 June 1968	118	50

8a. CONTRACT OR GRANT NO	9a. ORIGINATOR'S REPORT NUMBER(S)
AF 49(638)-1763	M.I.T. Department of Geology and Geophysics
b. PROJECT NO. 8652	No: S(Seismology) -2
c.	9b. OTHER REPORT NO(S) (Any other numbers that may be assigned this report)
d.	[redacted]

10 DISTRIBUTION STATEMENT

Distribution of this document is unlimited

11 SUPPLEMENTARY NOTES	12 SPONSORING MILITARY ACTIVITY
	Air Force Office of Scientific Research (SRPG) 1400 Wilson Blvd. Arlington, Virginia 22209

13 ABSTRACT

The research efforts of the research associates supported by this program are described. These studies are divided into two groups: I. Continental size arrays and their application, and II. Theoretical seismograms and earth structure.

A continental size array can be realized by considering individual seismic stations as array elements. A section of North America, where LRSM stations exist in sufficient density, is considered as a very large aperture array to supplement LASA. Travel times and $dT/d\Delta$ values for core phases (PKP, PKIKP) are measured with this array and the results are interpreted. A technique for direct measurement of $dT/d\Delta$ is also described.

The theoretical seismograms for P and S waves are computed for a model of point source in layered medium and matched with observed records. With this technique, the structures are determined for oceanic crust using marine refraction profiles, and for the upper mantle utilizing seismograms from NTS nuclear explosions.

DD FORM 1 NOV 65 1473

Unclassified

Security Classification

14 KEY WORDS	LINK A		LINK B		LINK C	
	ROLE	WT	ROLE	WT	ROLE	WT
Seismology						
Earth's core						
Arrays						
Synthetic seismograms						
Mantle structure						
Travel times						